Investigation of the Reversible Hysteresis Effect in Hexagonal Metal Single Crystals and the MAX Phases

A thesis

Submitted to the Faculty

of

Drexel University

by

Justin P. Griggs

in partial fulfillment of the

requirements for the degree

of

Doctor of Philosophy

December 2015

Dedications

This thesis is dedicated to my parents, Paul and Phyllis Griggs, and to my family who have supported me along the way.

Acknowledgements

I would like to thank those who have contributed to making the completion of my project a success. These individuals include my thesis advisors, Dr. Michel Barsoum and Dr. Mitra Taheri, whom I am grateful for their time and oversight of my project. I am grateful also for Professor Roger Doherty for his useful insight and great discussions, and grateful to Dr. Antonios Zavaliangos for being on my committee and for his mentoring and support. Special thanks for my colleague Babak Anasori, who contributed in invaluable ways through useful discussions and insight on my project. Much gratitude is owed for the time and hard work of Grady Bentzel in collecting the EDSB data, Andrew Lang and Greg Vetterick for the TEM data, Wayne Harlow for ex-situ FIB lift out work when needed on occasion, and Chris Barr for his useful insight into SEM analysis and data processing. Special thanks to many more who contributed in any way whether it was through informal discussions, material acquisition or hands on training.

Many thanks to the CRF staff Dmitri Barbash, Ed Basgall and Craig Johnson for training and use of CRF instruments and equipment. I am grateful for funding through the GAANN fellowship and also grateful for the office staff in the material science department, Sarit Kunz, Keiko Nakazawa, Yenneeka West, Dorilona Rose, and Leslie Anastasio for their years of support. I am grateful for family and friends who supported me along the way.

Table of Contents

List of Tables

List of Figures

Abstract

Investigation of the Reversible Hysteresis Effect in Hexagonal Metal Single Crystals and the MAX Phases

Justin Griggs
Michel Barsoum, PhD
Mitra Taheri, PhD

Hexagonal close packed (hcp) materials are abundant in nature, and are of great technological importance since they are used in many applications. When cyclically loaded some hcp solids outline fully and spontaneously reversible stress-strain hysteresis loops. To date, the micromechanical origin of these loops is unknown. To shed light on the subject, a spherical nanoindenter was repeatedly indented – up to 50 times in the same location - into Mg, Zn and Ti_3SiC_2 single crystals of various orientations, followed by select, post-indentation transmission electron microscope (TEM) cross sectional analysis. Based on the totality of the results, the energy dissipated per unit volume per cycle in the hexagonal metals can be related to the bowing out – and back – of geometrically necessary dislocations – in most cases in the form of low angle kink boundaries (LAKBs) - through statistically stored ones. Kinks were observed after indentations normal to the basal planes in Mg and Zn and also when indented normal to the $(10\bar{1}1)$ and $(10\bar{1}2)$ planes in Zn. When indented parallel to the basal planes in Zn, if hysteresis loops formed at all, they were insignificant in area. When $(10\bar{1}0)$ planes in Mg were indented, tensile twins formed. The most probable explanation for the energy dissipated in this direction is the growth and contraction of these twins. In the case of Ti_3SiC_2, hysteresis loops were observed even in absence of kink boundaries. No direct evidence for twins or non-basal slip was found nor has been reported in literature. Evidence presented in this study supports the existence of a new type of defect in bulk layered solids known as ripplocations – which combine features of dislocations and surface ripples – that are able to explain the phenomena observed in this study

on Ti_3SiC_2 in ways conventional dislocations cannot explain. It is the migration of these ripplocations that are believed to cause energy dissipation in Ti_3SiC_2. The energy dissipation due to ripplocations was found to be higher than the energy dissipation due to dislocations, which may offer a possible signature to distinguish between the two. However, the simplest method to distinguish between ripplocations and dislocations is to load the basal planes edge-on under a spherical indenter as carried out here. The formation of cracks, normal to the basal planes, are the unequivocal signature of ripplocations.

CHAPTER 1: INTRODUCTION

Hexagonal close packed (hcp) materials are abundant in nature, and are of great technological importance since they are used in many applications in industries such as the automotive, aerospace, electrical and hardware industries. Their importance is ever more demanding as it pertains to energy technologies. According to the Inventory of the U.S. Greenhouse Gas Emissions and Sinks [1], the electrical and transportation sectors accounts for the most greenhouse gas emissions annually, with electricity accounting for nearly one third of all emissions. Within the transportation industry, one of the largest reductions in greenhouse gas emissions will result from a reduction in total vehicle weight.

As the lightest structural metal, with a density two thirds of aluminum (Al), magnesium (Mg) and its alloys are promising candidates in reducing the total vehicle weight in automobiles and aircraft, thereby providing a viable option for improving fuel efficiency. Mg alloys are light-weight, provide great stiffness, and have a high specific strength among their many advantages [2]. An increasing number of automotive manufacturers are investigating the possibility of incorporating more Mg into automotive parts by replacing Al alloys and steel with Mg alloys. A major goal in moving forward with Mg incorporation into automobiles is to reduce the total vehicle weight by 15 percent [3].

Another important hexagonal material commonly used is zinc (Zn). It is used to galvanize steel to protect it from corrosion, and also used in coatings and alloys. Zn is recyclable, has a low melting point which means it also has a low cast temperature and therefore less susceptible to thermal shock, making it very economical as a casting material. Zinc alloys can offer strength of up to 60, 000 psi [4], and die cast alloys are believed to extend the life of die casting tools.

Household items, automotive parts and tools of all kinds may contain Zn, which illustrates its versatility.

In addition to metals, fairly new ceramic-metal hybrid materials known as MAX phases may show promising applications to these various industries equally well. A precise definition will be formulated in the subsequent chapters. The MAX phases have attracted attention as a material to potentially use in fission and fusion reactors [5, 6], especially for nuclear cladding applications. The MAX phases possess a hexagonal crystal structure as do Mg and Zn, and they have been the subject of investigations for their unique properties that are common to both metals and ceramics alike. Focusing on hcp materials in general, when some hcp solids are cyclically loaded, they outline fully and spontaneously reversible stress-strain hysteresis loops. To date, the micromechanical origin of these loops is unknown. It is necessary to understand the mechanisms involved in the deformation process to fully understand the origins of this effect. There is variation in the mechanical behavior associated with deformation of hcp metals [7] such that some hcp metals deform more easily by twinning than others, or some slip systems are active in some hcp metals that are not active in other hcp metals. Since the hcp crystal structure is a fairly complicated crystal structure to analyze and understand, robust crystal plasticity models for hcp materials are certainly a work in progress. Experimental and theoretical research would help lead to better crystal plasticity models for nonbasal deformation modes, from which constitutive laws for plastic deformation could be developed [7].

The purpose of this thesis is to contribute to the scientific understanding on the origins of reversible hysteresis loops in stress-strain curves that are observed in some hcp materials. Beginning with Chapter 2, this thesis will discuss background information on the deformation and mechanical properties of hexagonal materials specific to this study. Chapter 3 provides an experimental overview of the techniques, data acquisition and analysis that were used in this study. Chapters 4-6 presents specific experimental details, results and discussion from nanoindentation experiments that were performed on magnesium single crystal, zinc and the MAX phase Ti_3SiC_2. Chapter 7 provides a comparative analysis between the materials used in this study, and Chapter 8 provides a summary and conclusion of results, as well as an outlook for future work.

CHAPTER 2: BACKGROUND

2.1 Deformation in hcp materials

In comparison to materials with a body centered cubic (bcc) or face centered cubic (fcc) crystal structure, deformation of materials with a hexagonal closed packed (hcp) crystal structure is not as fully understood due to the diverse mechanical behavior of hcp materials, and the limited understanding of their nonbasal deformation modes [7]. The most common deformation modes observed within hcp materials, especially within metals, are deformation by slip and deformation twinning. Some hcp materials have also been known to deform by kink band formation [8-13], which includes a class of materials known as the MAX phases. The MAX phases are ternary layered carbides and nitrides having the general chemical formula $M_{n+1}AX_n$, where M is a transition metal, A is an A-group element, X is carbon or nitrogen and n = 1, 2 or 3. The MAX phases have an hcp crystal structure with generally c/a ratios, rendering nonbasal slip and/or twinning impossible, which in some ways renders understanding their deformation modes. Nonetheless, it is essential to understand the deformation modes to better contribute to understanding the different phenomena observed within hcp materials, and especially the MAX phases.

2.1.1 Slip in hcp materials

Deformation by slip is a process which involves the re-orientation of atoms in a crystalline lattice under a sufficient applied stress or sufficiently high temperature. This can be visualized as one row of atoms sliding over an adjacent row of atoms (see Fig. 2-1a) under a sufficient shear stress. A slip plane is the plane on which dislocations move by glide, and the slip direction is the direction in the slip plane that corresponds to the shortest lattice translation vector. Both the slip plane and slip direction constitute a slip system. In order for deformation by slip to occur, a minimum of five independent slip systems are required [14] to satisfy the von Mises criterion, and slip occurs when the applied stress exceeds the critical resolved shear stress (CRSS) on the slip system with the highest Schmid factor. In hcp materials, slip occurs in the $\langle 11\bar{2}0\rangle$ direction with the basal slip system being operative [15] in all hcp materials. The possible slip systems in an hcp crystal are basal slip $(0001)\langle 11\bar{2}0\rangle$, prismatic slip $\{10\bar{1}0\}\langle 11\bar{2}0\rangle$, 1st order pyramidal $\{10\bar{1}1\}\langle 11\bar{2}0\rangle$ and 2nd order pyramidal $\{11\bar{2}2\}\langle \bar{1}\bar{1}23\rangle$ slip. These different slip systems are illustrated in Fig. 2-1b.

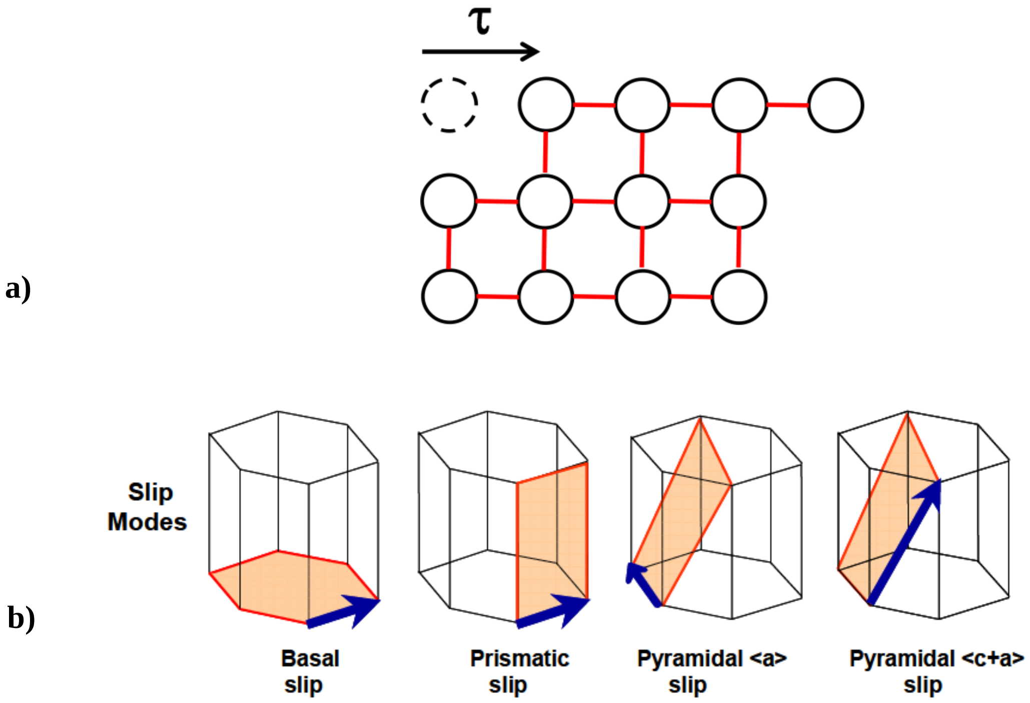

Figure 2-1. a) The process of deformation by slip is illustrated in which the top row of atoms slides relative to the second row of atoms under the shear stress τ. b) The slip planes and slip directions are shown for basal, prismatic, 1st order pyramidal and 2nd order pyramidal slip.

Dislocations gliding on the same slip plane may interact while in close proximity relative to one another. When dislocations with opposite signs interact on the same slip plane, they attract, combine and annihilate resulting in a perfect crystal (see Fig. 2-2a). On the contrary, dislocations having the same sign interact repulsively at close distances. When dislocations of the same sign are held up at an obstacle, such as at a grain boundary, dislocation pile ups may result as shown in Fig. 2-2b. Dislocation pile-ups create a back stress on the dislocation source.

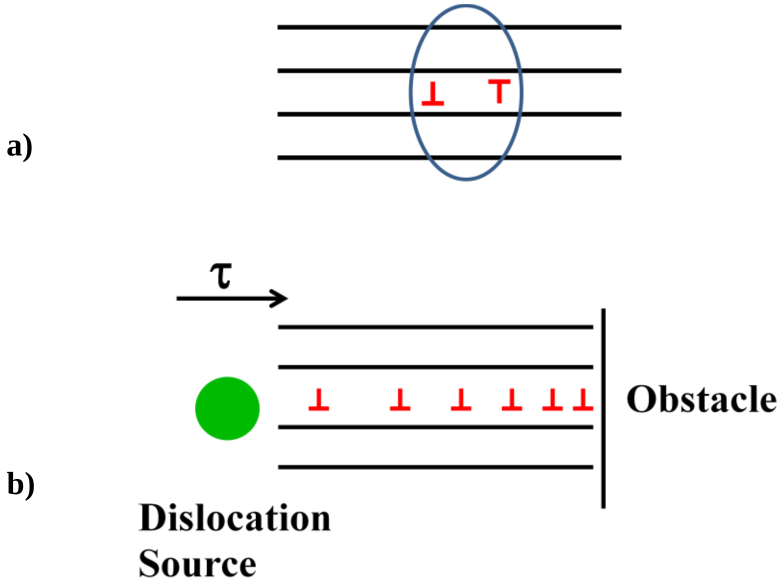

Figure 2-2. a) Dislocations of opposite sign gliding on the same slip plane, represented by solid lines. At close distances, the dislocations combine and annihilate, rendering a perfect crystal. b) Dislocations of the same sign gliding on the same slip plane pile up at an obstacle (i.e., grain/twin boundary, or pre-existing defect), inhibiting dislocation mobility. A back stress on the dislocation source is created as a result of the pile up.

Whenever deformation occurs by slip in hcp materials, the most commonly observed dislocations are those with <*a*> or <*c* + *a*> Burger's vectors. Cross slip may occur when screw dislocations slip onto another slip plane that contains its Burger's vector, enabling dislocations to glide on a different slip plane. This phenomenon is observed in some FCC metals, but occurs in hcp materials via constriction of the screw dislocation, and thus enabling the perfect dislocations to cross slip at the constriction.

2.1.2 Deformation twinning in hcp

Deformation twinning is another commonly observed deformation mode within hcp materials. A schematic of a twin is shown in Fig. 2-3, in which a twin boundary separates two regions in the crystal of different orientations. Twins in hcp materials reorient the crystal lattice and form when there are an insufficient number of slip systems to accommodate c-axis strain. They can make the crystal more favorable to deform by slip, and can occur as a result of annealing or deformation. The most common twinning modes observed in hcp metals are shown in Table 2.1, where K_1 and K_2 are the twin habit planes for the primary and conjugate twinning modes, and η_1 and η_2 are vectors representing the shear and conjugate shear directions respectively [14, 16]. The $\{10\bar{1}2\}$ twin is active in all hcp metals [14, 16], as seen in Fig. 2-4. In this figure, the twinning shear is plotted against the axial ratio, $\gamma = \frac{c}{a}$.

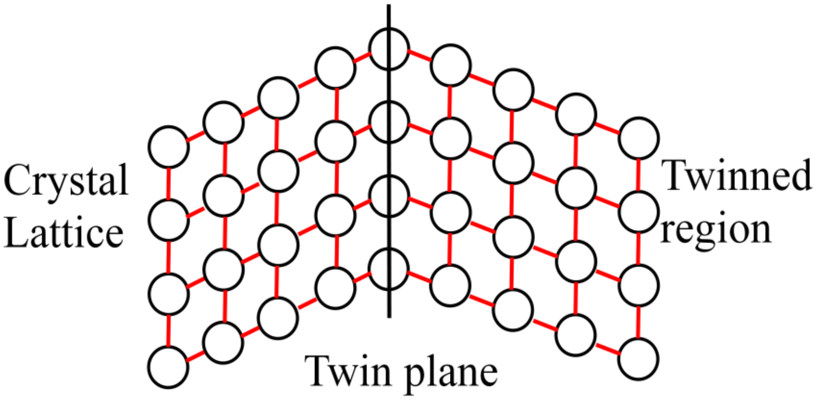

Figure 2-3. A schematic of a twinned region in a crystal is shown as a mirror image to the crystal lattice. The twinned region and crystal lattice is separated by a twin boundary.

The twinning shear, which depends on the c/a axial ratio, largely influences twinning [14]. The positive slopes in the Fig 2-4 correspond to contraction along the c-axis and negative slopes correspond to extension along the c-axis. Whenever $\gamma > \sqrt{3}$, the $\{10\bar{1}2\}$ twin is a contraction twin, and when $\gamma < \sqrt{3}$, the $\{10\bar{1}2\}$ twin is a tensile twin. Tensile twins cause extension along the c-axis and reorient the crystal lattice by ~86° about the $<11\bar{2}0>$ directions, while compression twins cause contraction along the c-axis and reorient the lattice by ~56° about the $<11\bar{2}0>$ directions. Second order twinning may occur, as in the case of Mg in which $\{10\bar{1}1\}$ twins may be followed by $\{10\bar{1}2\}$ twins in Mg [14], resulting in increased total plastic strain.

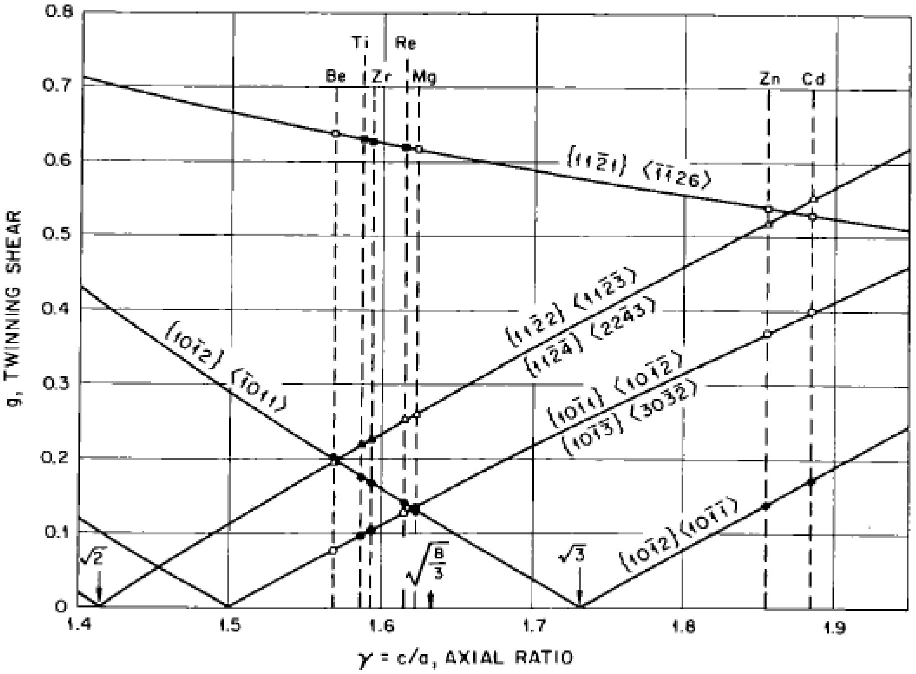

Figure 2-4. The relationship between the twinning shear and the c/a axial ratio for different hexagonal metals is shown in this figure. The filled circles are active deformation modes, while the open circles are inactive twinning modes [14].

Table 2-1. The family of primary (K_1) and conjugate (K_2) twin planes are shown along with their corresponding shear directions.

K_1	K_2	$\boldsymbol{\eta_1}$	$\boldsymbol{\eta_2}$
$\boldsymbol{\{10\bar{1}2\}}$	$\{10\bar{1}\bar{2}\}$	$\pm <10\bar{1}\bar{1}>$	$\pm <10\bar{1}1>$
$\boldsymbol{\{10\bar{1}1\}}$	$\{10\bar{1}\bar{3}\}$	$<10\bar{1}\bar{2}>$	$<30\bar{3}2>$
$\boldsymbol{\{11\bar{2}2\}}$	$\{11\bar{2}\bar{4}\}$	$\frac{1}{3}<11\bar{2}\bar{3}>$	$\frac{1}{3}<22\bar{4}3>$
$\boldsymbol{\{11\bar{2}1\}}$	(0002)	$\frac{1}{3}<\bar{1}\bar{1}26>$	$\frac{1}{3}<1120>$

Basal and prismatic dislocations interact with $\{10\bar{1}2\}$ and $\{11\bar{2}1\}$ twins repulsively in Mg, Co, Re, Zr, Ti, Hf and Be leading to local stress concentrations due to dislocation pile-ups at the interface [14, 17]. As a result, conjugate twins or other twins may form, or a crack may form depending on the cleavage strength of the material. In the case of Zn and Cd, the basal dislocation interaction with the $\{10\bar{1}2\}$ twin is attractive [14, 17] and leads to the subsequent growth of the twin.

2.1.3 Kink bands in hcp materials

The theory of kinking in metals was first introduced by Orowan (1942) [9], who proposed a deformation mechanism in metal single crystals different from slip and twinning. Orowan observed kinking behavior in Cd single crystals when loaded parallel to the basal planes under compression (see Fig. 2-5c). Kink band formation is a deformation mechanism observed in some hcp materials such as in graphite [18] and ZnO [19], and also in layer structures such as mica [12]. Figure 2-5 shows examples of kink bands in Ti_3SiC_2 at different length scales.

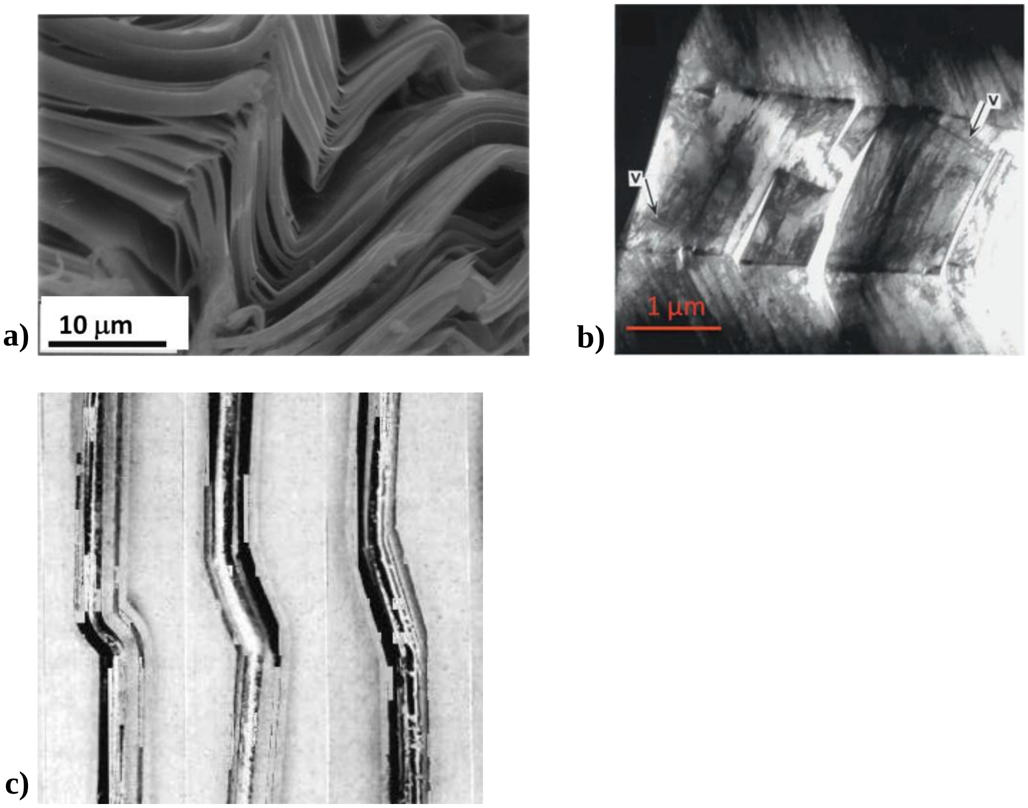

Figure 2-5. Kink bands in Ti_3SiC_2 at different length scales. a) Image shows an SEM image of kink bands while, b) shows a brightfield image of kink bands with mobile dislocation walls labeled, V, in image [11]. c) Kinks in Zn single crystal after compressed parallel to basal planes [20].

The precise mechanism that leads to kind band formation is not understood. Frank and Stroh [21] considered a thin elliptical kink band comprised of two dislocation walls of opposite sign spaced a small distance that grow to form kink boundaries. In the work of Frank and Stroh, pairs of dislocations of opposite sign nucleate and grow at the tip of a thin elliptical kink, which has length 2α and width 2β with $\alpha >> \beta$ (see Fig. 2-6). Dislocations of opposite sign are attracted to one another, but are held apart under an external applied stress.

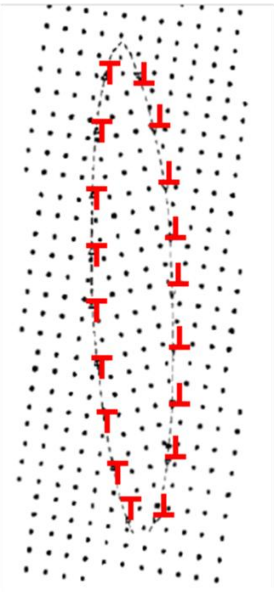

Figure 2-6. Dislocation pairs of opposite sign nucleate and grow at the tip of an elliptical kink. The dislocation walls are held apart only under an external applied stress and annihilate when the stress is removed [21].

Using the Griffith approach, Frank and Stroh determined the critical stress at which the kink band will grow to be

$$\tau_c \approx \frac{\sigma_c}{M} = \sqrt{\frac{4G^2 b\gamma_c}{2\alpha\pi^2}\ln\left(\frac{b}{w\gamma_c}\right)}\ , \qquad (2\text{-}1)$$

where, τ_c is the shear stress, G is the shear modulus, b is the Burger's vector, γ_c is the critical kinking angle, w is a length on the order of b and related to the core energy of a dislocation, M is a Taylor factor relating the shear stress to the axial stress. Finally, the critical kinking angle was determined by Frank and Stroh to be

$$\gamma_c = \frac{b}{D} \sim \frac{3\sqrt{3(1-\nu)}}{2G}\tau_{loc}\ , \qquad (2\text{-}2)$$

where τ_{loc} is the local stress needed to nucleate a dislocation pair. When $\gamma \geq \gamma_c$, then the kink band will grow. If a kink band extends to a free surface, then the dislocation walls will be pushed apart and become parallel planes, forming the kink boundaries. A micro-scale model based on the work Frank and Stroh was later developed to describe the process of kink band formation as well as to help explain a unique phenomenon observed in materials capable of deforming by kink band formation. Before this micro-scale model can be introduced, a discussion on elasticity and mechanical behavior is necessary.

In layered structures such as mica and the MAX phases, kink bands are often observed with delamination between layers (see Fig. 2-5a and b), and sometimes with cracks adjacent to or near kink bands.

2.1.4 Ripplocations

A new deformation micromechanism has been proposed by Kushima et al. [22] for 2D van der Waals solids, that they termed ripplocations. In their study using high resolution transmission electron microscopy (HRTEM) on MoS_2, ripplocations (see Fig. 2-7a) were regarded in the context of 2D van der Waals homostructures and defined as being a local line of ripple created by an excessive line of atoms that are locally inserted into one layer relative to the other, thereby creating a local line of ripple in the van der Waal homostructure. Ripplocations were described by Kushima et al. [22] as being topologically equivalent, but energetically distinct from dislocations in bulk crystals. Some characteristics of ripplocations includes being localized with core width on the order of a few nanometers, ripplocations of same-sign attract (see Fig. 2-7b) and merge, and the core energy is equal to the total energy. The total energy of a ripplocation is the sum of the elastic bending energy, U_B, and the interfacial energy, U_s. It was also inferred in this study on MoS_2 that bonds are not broken when ripplocations form.

Ripplocations are theorized as being capable of nucleating, migrating or annihilating [22] in response to mechanical loading, thermal or chemical changes.

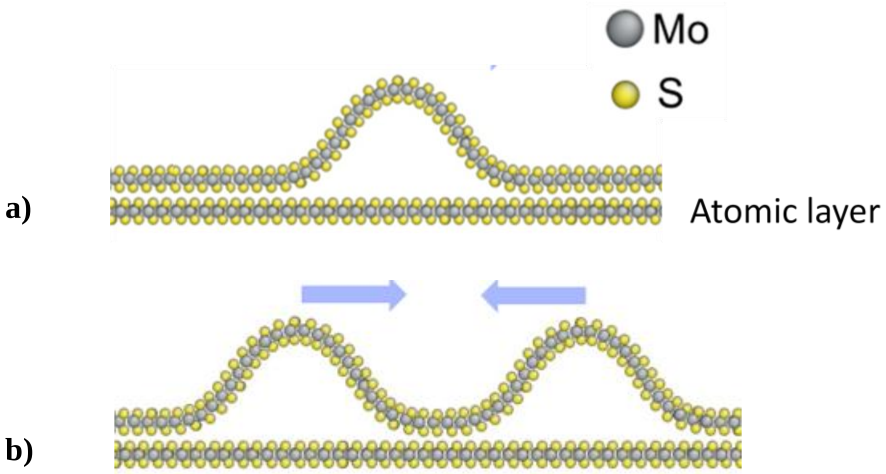

Figure 2-7. a) Schematic of a ripplocation in MoS_2. b) Ripplocations of the same sign shown attracting just before merging [22].

While the study of ripplocations on MoS_2 has been theorized for 2D layered van der Waals solids, they are certainly relevant in this study on the MAX phases, granted the MAX phases are layered solids. To date, no direct evidence of <c + a> dislocations have been reported in literature on the MAX phases, and yet in numerous studies involving indentation on the (0001) plane of various MAX phases, c-axis deformation has been observed even in absence of visible damage [23]. As shown herein, ripplocations within the MAX phases better explain observations. If ripplocations do indeed exist in a bulk crystal, it is likely they would be slightly different compared with a 2D layered van der Waal solid.

2.2 Mechanical behavior

As structural materials are deformed under an applied load, the amount of deformation at a given load is valuable information for design and construction purposes. The typical data used to quantify the amount of deformation at a given load is the stress vs. strain curve (see Fig. 2-8). Although there are different types of stresses, the engineering stress, σ, is defined by

$$\sigma = \frac{P}{A_0}, \qquad (2\text{-}3)$$

where P is the applied load and A_o is the cross sectional area under no applied stress. Similarly, if a material, such as a rod or bar of length l_o, is deformed either in tension or compression, then the engineering strain is defined as

$$\varepsilon = \frac{(l - l_0)}{l_o} = \frac{\Delta l}{l_0} \qquad (2\text{-}4)$$

where l is the length after deformation. By convention, when materials are deformed in tension, then $\varepsilon > 0$, and when materials are deformed in compression, $\varepsilon < 0$.

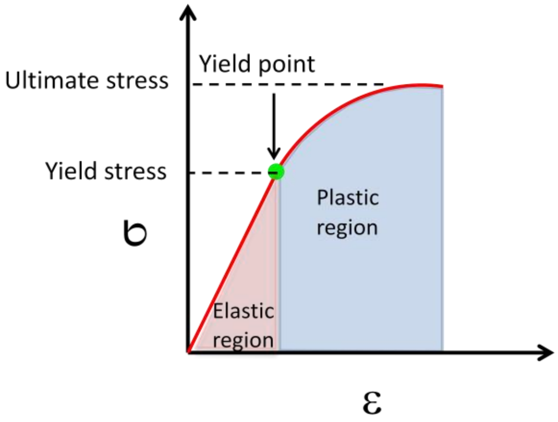

Figure 2-8. A typical stress vs. strain curve for materials such as metals or alloys is shown. The yield stress is indicated by the green circle, at which point, deformation transitions from elastic to plastic. These two regions are shaded below the curve on the strain axis, respectively.

There are two types of deformation, which are elastic and plastic deformation. Elastic deformation is temporary and is recovered fully when an applied load is removed, while plastic deformation is permanent and non-reversible when an applied load is removed. Typically, structural materials, such as metals or alloys, deform elastically until yielding occurs, at which point the onset of plastic deformation occurs. In the stress-strain curve (see Fig. 2-8), this is manifest by a region that is first linear and then transitions to non-linear at the yield point. The slope of the line in the elastic region of the stress-strain curve (see Fig. 2-8) is the modulus of elasticity, E, also known as Young's modulus. The relationship between stress and strain in the linear elastic region of the stress-strain curve is given by:

$$\sigma = E\varepsilon. \tag{2-5}$$

This holds only in simple tension or compression, but does not apply, for example, in particle compaction. The stress and strain in Eq. 2-5 correspond to normal stresses and strains.

As structural materials are deformed beyond the yield point, the stress increases to a maximum (ultimate) stress, and the material continues to deform plastically. The strength of the material actually increases with increasing plastic deformation until a maximum stress is achieved. This phenomenon of increasing the strength of a material through deformation is known as strain hardening (or cold work). The stress vs. strain behavior in this process is shown schematically in Fig. 2-9 under loading, unloading and re-loading. After strain hardening has resulted, the stress required to plastically deform material has increased to beyond the previous maximum stress (see Fig. 2-9).

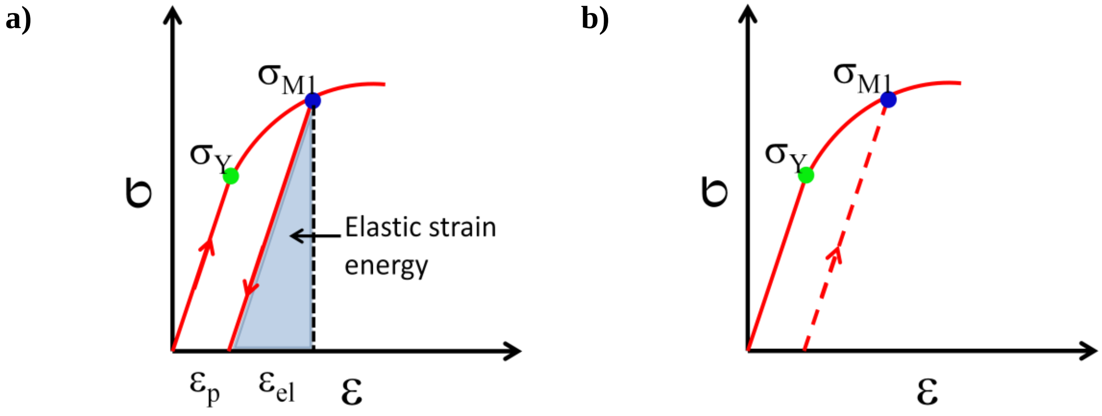

Figure 2-9. Schematic showing the stress vs. strain behavior in the process of loading, unloading and re-loading. a) Elastic deformation occurs until the yield stress, σ_y, is achieved, at which point plastic deformation occurs. The material continues to deform plastically until the stress σ_{M1} is achieved. When the load is removed, some elastic strain, ε_{el}, is recovered, and the total change in strain between initial loading and unloading is the total plastic strain, ε_p. The area below the elastic strain portion of the curve is the elastic strain energy. b) Upon reloading, the material will deform elastically until the stress σ_{M1}, is achieved, and then plastically when the applied stresses > σ_{M1}, following the trajectory of the plastic region in the stress vs. strain curve in part (a).

The amount of plastic strain within a material is related to the dislocation density by the following equation:

$$\gamma = b\bar{x}\rho \tag{2-6}$$

where γ is the shear strain, $\bar{x}$ is the average total displacement of mobile dislocations and ρ is the total dislocation density. This relationship will be useful in the later chapters in which dislocation densities are correlated with the amount of plastic deformation under a spherical indenter.

Much of the discussion on stress and strain, and elasticity and plasticity has focused on the simplest case. In general (i.e., in 3D), stress and strain are related in the following way:

$$\sigma = C\varepsilon \qquad \text{or} \qquad \varepsilon = S\sigma \tag{2-7}$$

where both C and S are the stiffness and compliance, respectively, and represent 4th order tensors. Equation 2-7 can be represented with repeated notation as follows:

$$\varepsilon_{ij} = S_{ijkl}\sigma_{kl} \tag{2-8}$$

in which every strain component depends linearly on the corresponding stress component. Note that $\sigma_{kl}= \sigma_{lk}$ and $\gamma_{kl} = \gamma_{lk}$ by symmetry, which allows for a reduction in independent compliances to 21 components. In the hexagonal crystal structure, there are seven independent compliances. Equation 2-8 could have been expressed in terms of the stiffness as well, C_{ij}, which represent the elastic constants. There are 5 independent elastic constants in the hexagonal crystal structure, namely C_{11}, C_{12}, C_{33}, C_{13}, and C_{44}.

The values for the compliance tensor for a hexagonal material can be used to calculate the elastic modulus along a specific direction. In anisotropic solids, such as in hcp materials, the elastic modulus varies by orientation. The elastic modulus along a direction, d, in a hexagonal crystal is given by the following equation:

$$\frac{1}{E} = (1- \varphi^2)s_{11} + \varphi^4 s_{33} + \varphi^2(1- \varphi^2)(2s_{13} + s_{44}) \tag{2-9}$$

where φ is the cosine of the angle between the direction, d, and the c-axis. This equation is useful especially when performing nanoindentation on hcp materials since indentation may be applied entirely within specific grains of varying orientations.

2.3 Reversible Non-linear Strain Model

At this juncture, one model will be discussed that attempted to explain a unique phenomenon – that is, the reversible plastic deformation within some hcp materials. References to other models and a brief description will be introduced in subsequent chapters as needed. In the previous sections, a model describing kinking was presented as well as discussion on elasticity and mechanical behavior. A micro-scale model was developed that incorporates both of these topics of discussion.

2.3.1 The KNE Model

As mentioned previously, when materials are compressed within the elastic regime of the stress-strain curve, the curve returns to the point of origin upon unloading. However, some solids such as sapphire [24], Mg [25, 26], graphite [18], the MAX phases [13, 27, 28], have been reported to exhibit fully reversible nonlinear strain after cyclic loading. Typically, the material is deformed with some net plastic strain during the first cycle rendering an open loop or cycle when the load is removed. During subsequent cycles, the loops become less open until finally achieving full reversibility. As a load is applied, the material deforms elastically until the yield point is reached, at which point the stress-strain curve transitions from linear to nonlinear until a maximum stress is achieved. When the load is removed, the curve returns to the point of origin forming a closed hysteresis loop, shown schematically in Fig. 2-10. The area of the loop, W_d, is the energy dissipation per unit cycle per unit volume. Details of calculating the area of a loop will be discussed in Ch. 3.

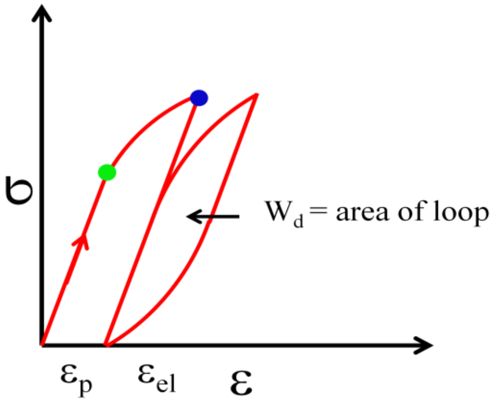

Figure 2-10. The stress-strain behavior is shown for a typical KNE solid, in which reversible non-linear strain results during cyclic loading. The number of cycles required to achieve full reversibility varies by material, but this exaggerated scenario shows the typical behavior once the cyclic threshold has been achieved.

The aforementioned and other hcp materials that exhibit reversible plastic strain have in common the fact that each has been reported to deform by kink band formation and have been designated to a special class of materials known as kinking nonlinear elastic (KNE) solids. The term KNE refers to a solid whose deformation mechanism is by kink band formation, has nonlinear reversible strain, and elastic since no *net* plastic deformation occurs. Plastic anisotropy is a necessary condition for a solid to be KNE, and a good measure of plastic anisotropy in hcp materials is the c/a ratio. Solids that have $c/a > \approx 1.5$ or are layered solids [12, 13, 29] tend to be not only plastically anisotropic, but also tend to be KNE.

Following the work of Frank and Stroh [21], Barsoum et al. [5] developed a microscale model for KNE solids that serves as an energy dissipative model to describe the process of kink band formation as well as the origins of W_d. Frank and Stroh [21] theorized the existence of subcritical kinks as a precursor to kinking, while Barsoum et al. [5] provided a model for such a mechanism. Using the same approach as Frank and Stroh [21], an elliptical kink band of length 2α and width 2β with $\alpha >> \beta$ was considered and used in the KNE model. The Incipient Kink Band (IKB) was invoked to explain the micromechanism responsible for kinking nonlinear elasticity. IKBs consist of multiple coaxial parallel dislocation loops separated by a distance D. A schematic of an IKB is shown in Fig. 2-11a. An IKB can be thought of as a kink band, which has not dissociated into two mobile dislocation walls (see Fig. 2-11b). As a load is applied, the two dislocation walls of the IKB are pushed apart in opposite directions, and upon removal of the load, the dislocations of opposite sign attract and annihilate. If a sufficiently large load is applied, then the IKB will dissociate into two mobile dislocation walls (see Fig. 2-11c), forming a kink band comprised of two kink boundaries (see Fig. 2-11d).

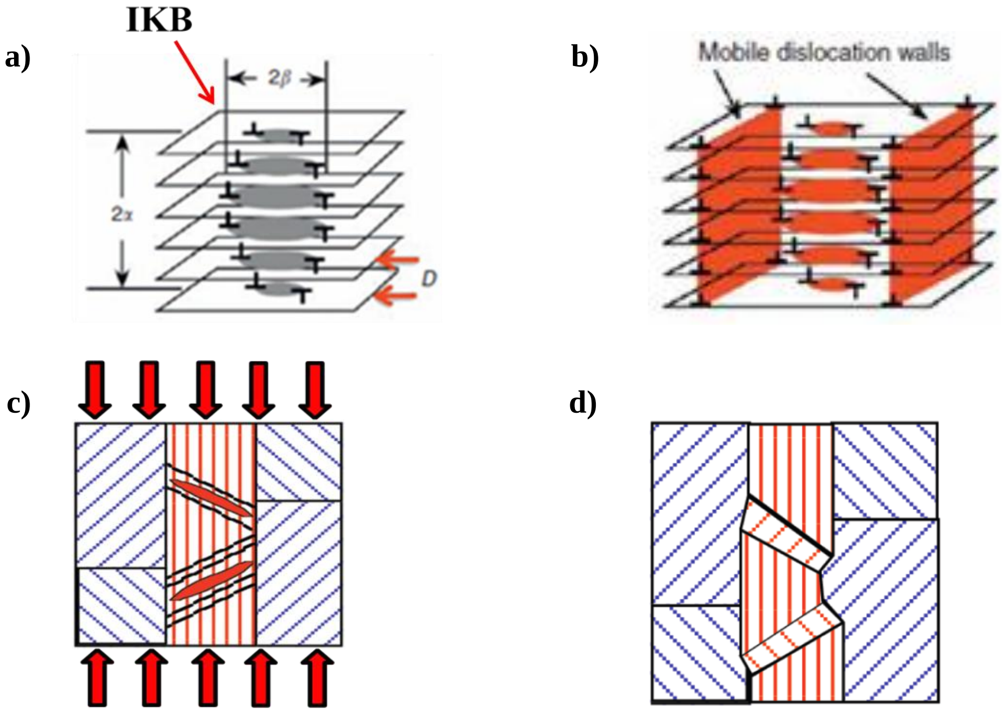

Figure 2-11. a) Schematic of an IKB of length 2a and with 2b, which consists of dislocation loops confined to multiple parallel planes. b) Mobile dislocation walls (MDWs) are shown. c) Under sufficient applied load, the MDWs dissociate and coalesce to form d) permanent kink boundaries.

During loading, the total strain is the sum of the linear elastic and nonlinear reversible strain, which in a KNE solid, the nonlinear strain is the sum of the strain due to the presence of IKBs ($\varepsilon_{\mathbf{IKB}}$) and strain due to reversible dislocation pileups ($\varepsilon_{\mathbf{DP}}$) [13]. The total strain in the KNE model is given by:

$$\varepsilon_{Tot} = \frac{\sigma}{E} + \varepsilon_{NL} = \frac{\sigma}{E} + \varepsilon_{IKB} + \varepsilon_{DP} \qquad (2\text{-}10)$$

In what follows, it is assumed that ε_{DP} can be neglected.

In Eq. 2-10, σ is the axial stress and E is Young’s modulus. The strain due to the presence of IKBs is given by the following expression:

$$\varepsilon_{IKB} = \frac{\Delta V N_v \gamma_c}{k_1} \qquad (2\text{-}11)$$

where N_v is the number of IKBs per unit volume, ΔV is the change in kinked volume, γ_c is defined as in Eq. 2-2, and k_1 is a factor relating the volume strain due to the IKB to the axial strain. Using the following relations,

$$\Delta V = \frac{4}{3}\pi\alpha(\beta_x\beta_y - \beta_{cx}\beta_{cy}) \tag{2-12a}$$

$$2\beta_x \approx \frac{2\alpha(1-\nu)}{G\gamma_c}\frac{\sigma}{M} \ and \ 2\beta_y \approx \frac{2\alpha}{G\gamma_c}\frac{\sigma}{M} \tag{2-12b}$$

the strain due to IKBs is determined by

$$\varepsilon_{IKB} = \frac{N_v\gamma_c 4\pi\alpha(\beta_x\beta_y - \beta_{cx}\beta_{cy})}{3k_1} = \frac{N_v 4\pi\alpha^3}{3k_1 G^2\gamma_c M}(\sigma^2 - \sigma_t^2) = m_1(\sigma^2 - \sigma_t^2), (8)$$

where σ_t is the threshold stress. The energy dissipated per unit cycle per unit volume, W_d, is the area of the loop on the stress-strain curve in Fig. 2-10 and is given by

$$W_d = \frac{4\boldsymbol{\Omega}\pi N_v\alpha}{D}(\beta_x\beta_y - \beta_{cx}\beta_{cy}) = \frac{4\pi(1-\nu)N_v\alpha^3}{G^2\gamma_c M^2}\frac{\Omega}{b}(\sigma^2 - \sigma_t^2) = m_2(\sigma^2 - \sigma_t^2) \tag{2-13}$$

where Ω is the energy dissipated as the dislocation line moves per unit area. It follows then that Ω/b is the critical resolved shear stress for an IKB[13, 28]. Thus,

$$W_d = 3k_1\frac{\Omega}{b}\varepsilon_{IKB} = \frac{m_2}{m_1}\varepsilon_{IKB} \tag{2-14}$$

The above derivation is known as the KNE model, which is a dislocation based and energy dissipative model developed to explain kinking and nonlinear elastic behavior. In the model, W_d is proportional to the applied stress squared, σ^2 and also to the nonlinear reversible strain, as observed experimentally [12, 13, 24-28, 30].

CHAPTER 3: EXPERIMENTAL DETAILS

3.1 Instruments and materials studied

An environmental scanning electron microscope, SEM (Philips FEI XL30) equipped with electron backscatter diffraction (EBSD) was used to generate an orientation map of different grains, or to confirm the orientation of single crystals used in the various experiments. Nanoindentation, NI, experiments were performed using a nanoindenter (MTS Nanoindenter XP system, MTS Corporation, Oak Ridge, TN) into select grains or on single crystals using spherical tips with hemispherical radii of either 21 μm or 100 μm. A dual beam focused ion beam SEM (FEI Dual Beam 235) was used to measure the radius of the plastic residual marks after indentation and to prepare cross section lift outs of indents for microstructural analysis in the transmission electron microscope, TEM (JEOL 2100 LaB_6). An atomic force microscope (Park NX10 AFM) was used to study the surface topography around select indents on the MAX phase.

A list of all materials used in this study is shown in Table 3-1. Although nanoindentation experiments were also performed on other materials (Ti_2AlC, Cr_2GeC, Zr, and Re) and on other orientations for the materials listed, this study focused primarily on the ones listed in Table 3-1. The orientations that were focused on primarily for Mg and Ti_3SiC_2 were the (0001) and the $(10\bar{1}0)$ orientations, while the primary orientations in Zn were the (0001), $(10\bar{1}2)$, $(10\bar{1}1)$ and $(10\bar{1}0)$. The average grain or single crystal sizes ranged from 200 μm to > 500 μm. Specific experimental details for each material will be covered in subsequent chapters, which include sample prep, indenter tip sizes, maximum applied load and number of cycles used.

Table 3-1. Materials used in this study along with the orientations tested and typical grain/crystal sizes. The red outline indicates the orientations of primary focus on this study on a given material.

Material	Orientation	Grain Size (μm)
Magnesium	(0001)	500 – 700 single crystal
	$(10\bar{1}0)$	
	$(10\bar{1}2)$	
Zinc	(0001)	200 – 700
	$(10\bar{1}0)$	
	$(10\bar{1}2)$	
	$(10\bar{1}1)$	
	$(2\bar{1}\bar{1}0)$	
Ti_3SiC_2	(0001)	200 – 300
	$(10\bar{1}0)$	
	$(2\bar{1}\bar{1}0)$	

3.2 Experimental procedure and data analysis

3.2.1 Indentation stress vs. a/R curves

After each sample was prepared for NI experiments, continuous stiffness mode (CSM), nanoindentation experiments was performed on select grains in Zn or Ti_3SiC_2, identified from the orientation map, or on Mg single crystals. When run in CSM mode, the NI records the stiffness simultaneously to the load and displacement. The specific details for each test on each material will be addressed in subsequent chapters. As a general approach, each test consisted of loading a given location to a peak load, unloading to a minimum load of 5 mN for either 25 or 50 times, followed by 5 incremental loading and unloading cycles with the peak loads ranging between 20 – 100% of the peak load. A sufficient number of cycles are required to achieve an equilibrium microstructure defined as one that does not further evolve with cycling. The minimum number of cycles to achieve an equilibrium microstructure, varied depending on the material, but typically fell in the range of 5 – 10 cycles for materials used in this study. Hence, 25 or 50 cycles were used in this study to ensure the closure of nested cycles following cyclic loading. The targeted strain rate for each test was 0.1 s^{-1}.

Figure 3-1 shows a schematic of a spherical nanoindenter tip indenting into a surface.

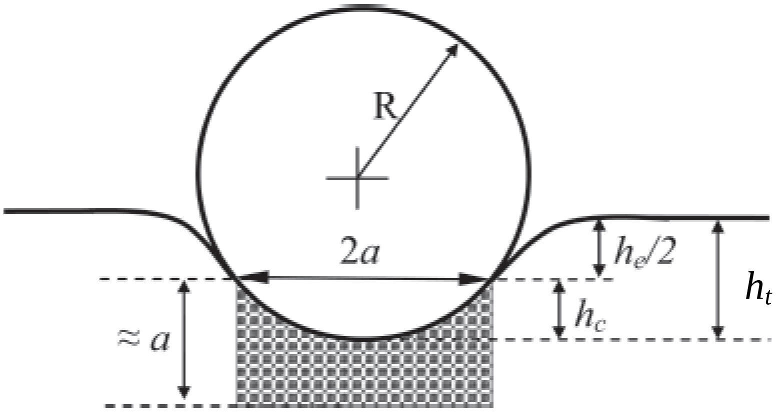

Figure 3-1. Schematic of a spherical nanoindeter indented into a material surface. The indenter radius, R, contact radius, a, elastic displacement, h_e, total displacement, h_{tot}, and contact depth, h_c, are labeled [31].

The load vs. displacement data was converted to indentation stress vs. indentation strain curves. Following the derivation given in [31], the derivation begins with the Hertz equation:

$$P = \frac{4}{3} E_{eff} R^{1/2} h_e^{3/2} \tag{3-1}$$

where P is the indentation load, E_{eff} is the effective elastic modulus of the indenter tip and specimen system, R is the indenter radius and h_e is the elastic displacement into the surface. The effective modulus is given by

$$\frac{1}{E_{eff}} = \frac{(1-\nu_s^2)}{E_s} + \frac{(1-\nu_i^2)}{E_i} \tag{3-2}$$

where E_s and ν_s are the specimen elastic modulus and Poisson's ratio and E_i and ν_i are the elastic modulus and Poisson's ratio of the diamond indenter.

Using a result by Sneddon [32] for rigid spherical indenters in the elastic regime, the following holds:

$$h_e = h_t = \frac{a^2}{R} \tag{3-3}$$

h_t is the total displacement into the surface and a is the contact radius. It suffices to calculate the contact depth, h_c, for both the elastic regime and the elasto-plastic regime so that the contact radius, a, can be determined. Beginning with the elastic regime, h_e will be derived first and then h_c will be determined for the elastic-plastic regime.

Using a method by Oliver and Pharr and Field and Swain [33, 34] involving the slopes of the loading and unloading portion of the load vs. displacement curve, the value for h_c can be determined. By differentiating Eq. 3-1 with respect to *h*, which yields

$$\frac{dP}{dh} = 2E_{eff}R^{1/2}h_e^{1/2} \ , \tag{3-4}$$

and substituting the result back into Eq. 3-1, the follow expression for the load is obtained

$$P = \frac{2}{3}\frac{dP}{dh}h_e \ . \tag{3-5}$$

Note that dP/dh is simply the stiffness of the system and load frame, S_{sys}, and the stiffness, S, is given by:

$$\frac{1}{S} = \frac{1}{S_{sys}} - \frac{1}{S_f} \tag{3-6}$$

where S_f is the load frame stiffness reported by the manufacturer to be 5.5 MN/m. Equation 3-5 can be rearranged as follows to give an expression for h_e in terms of load (P) and stiffness (S):

$$h_e = \frac{3}{2}P\frac{dh}{dP} = \frac{3}{2}\frac{P}{S} \, . \tag{3-7}$$

This expression relates the elastic displacement into the sample to the load and stiffness and holds for the elastic regime. A similar expression can be derived for the elastic-plastic regime. The contact depth, h_c, used in the elastic-plastic regime follows the work of Oliver and Pharr and Field and Swain [33, 34], and is assumed to be

$$h_c \approx h_t - \frac{h_e}{2} \; . \tag{3-8}$$

Equation 3-7 can be combined with Eq. 3.-8 and h_c can be expressed in terms of P, S and h_t as

$$h_c = h_t - \frac{3}{4}\frac{P}{S} \; . \tag{3-9}$$

The contact radius, a is determined from h_c assuming the following relationship

$$a = \sqrt{2Rh_c - h_c^2} \approx \sqrt{2Rh_c} \; , \tag{3-10}$$

where the right hand side of Eq. 3-10 holds provided $h_c << a$ and assuming a perfectly spherical indenter tip.

In the elastic regime, $h_c = h_e/2 = h_t/2$, while in the plastic regime $h_c \approx h_t$ since for the most part, $h_t >> h_e/2$. By determining the contact depth, h_c, the contact radius, a, can be determined using Eq. 3-10. Using Eq. 3-1 and expressing h_c in terms of a and R yields the follow expression:

$$\frac{P}{\pi a^2} = \frac{4}{3\pi} E_{eff} \left(\frac{a}{R}\right) \tag{3-11}$$

where the term on the left is the indentation stress, which is plotted against $(\frac{a}{R})$ in this work. While the precise definition of indentation strain is debatable, in this work we relate the ratio $\left(\frac{a}{R}\right)$ to the non-linear strain (see Ch. 4). The conclusions reached in this study using indentation stress vs. $\left(\frac{a}{R}\right)$ remain valid for indentation stress vs. indentation strain relationships since there is a relation between $\left(\frac{a}{R}\right)$ and the indentation strain. In this work, the use of a/R is preferable to converting the latter to indentation strain.

3.2.2 Drift correction and W_d calculations

Because of the relatively large number of cycles used in each location, drift was, in many cases, unavoidable. This was evidenced as an increase (or sometimes decrease) in total displacement, h_t, during the duration of a specific test. Figure 3-2a shows a load vs. displacement curve where instrumental drift occurred. This drift increases the total displacement, which in turn increases the contact radius and results in an apparent decrease in the indentation stress (Fig. 3-2b). Two separate methods were used to correct drift, depending on the final indent geometry. The first method will be discussed here, and second method will be discussed as needed in the later chapters.

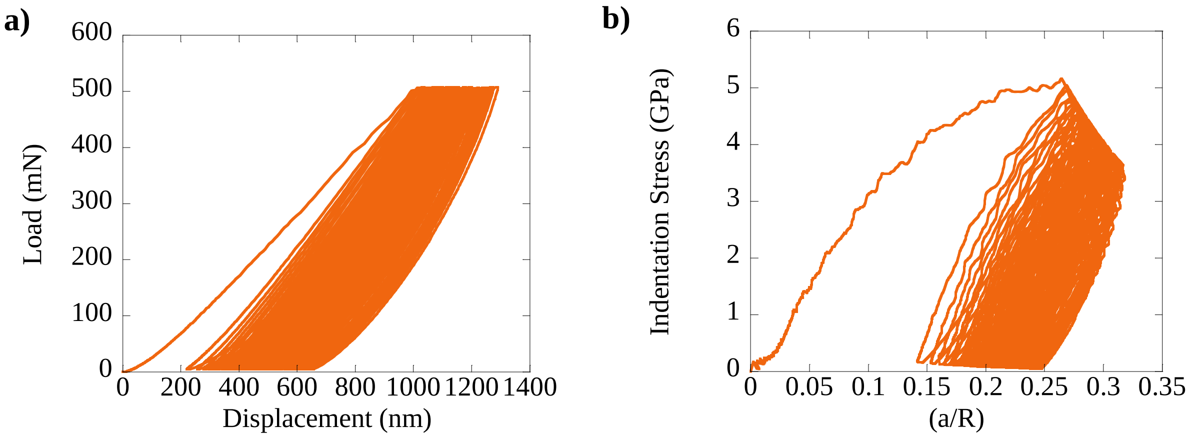

Figure 3-2. a) Load vs. displacement curves where instrumental drift occurred. b) Resulting indentation stress is plotted against a/R for the corresponding load vs. displacement curve in (a), illustrating the effect of instrumental drift on the indentation stress.

When the indents resulted in spherical craters, to correct for instrumental drift, the contact radius of the spherical crater after indentation was first measured in the FIB-SEM, a_{SEM}. The FIB-SEM measurements produced -2 % or + 1% errors depending on whether measurements were taken at 0° or 52° tilt. After measurements were taken, corrections were made to compensate for errors, averaged and a standard deviation was calculated. The average of the measured values will henceforth be denoted by $a_{SEM.}$ This value was compared with calculated values for the contact radius after each cycle from the nanoindentation data (i.e., using Eq. 3-10). The cycle at which $a_{SEM} \approx a$, – after unloading – was the cycle to which the raw data (load vs. displacement) was manually shifted, before recalculating the NI stress. For example, if $a_{SEM} \approx a$ after n cycles, then the load vs. displacement data for cycles (n+1) – 50 were shifted to cycle n. Figure 3-3a illustrates this process. Indentation stress vs. a/R plots were plotted, but now with the drift removed (Fig. 3-3b).

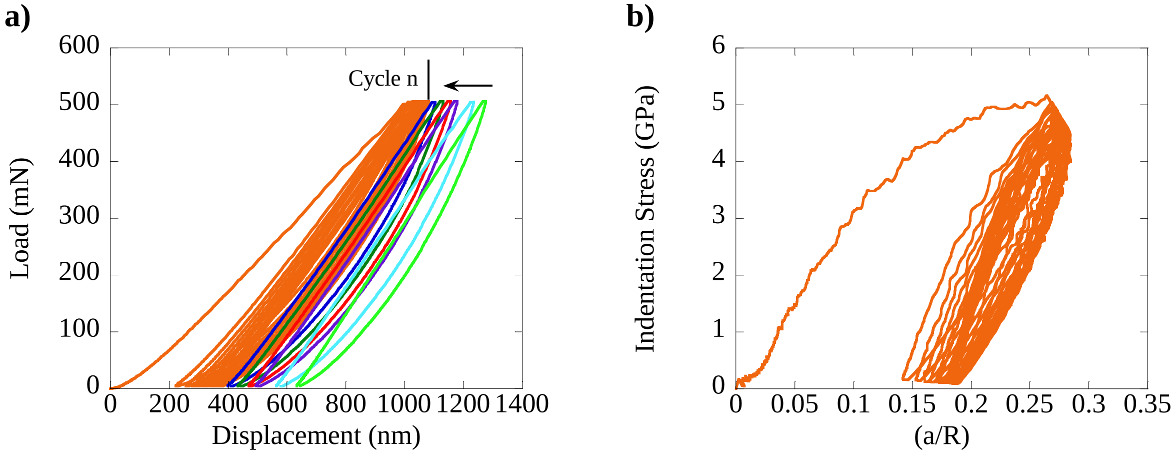

Figure 3-3. a) Load vs. displacement cycles are shifted to cycle n, at which point, the contact radius measurements in the SEM matched those calculated from the nanoindentation data. This process was done to remove instrumental drift. b) The indentation stress vs. a/R curve is shown here with the drift removed.

In some cases, when the drift was minimal, no corrections were required. In most cases, the runs that did drift resulted in indentation stress vs. a/R curves after correction that were almost identical to the ones where there was no drift, lending credence to the methodology used herein. Note that equating a to a_{SEM} ensures that the maximum stresses that are then used in later analysis are accurate.

It is important to note that instrumental drift can be corrected using the method described herein as long as the drift rate was relatively low at the beginning of a test. If the drift rate is high upon initial loading – as was the case for some indents studied on Mg on the 0001 plane loaded to 80 mN – it was not possible to correct for drift after a large number of cycles using the method described herein. This was especially true when a_{SEM} was *smaller* than the *a* after the first cycle, indicating high drift initially. Hence, NI data from those locations was not emphasized or used for analysis. The TEM data collected from these experiments, however, remains valid and was used in microstructural analysis.

After the drift corrections were made (if needed), the nested cycles in the indentation stress vs. a/R curves were plotted and analyzed. Typically, the sequence resulted in closed loops (see Fig. 3-4), the areas of which represent W_d. The loop area was approximated by taking the difference in area beneath the loading and unloading curves using a sequence of rectangle approximating both areas beneath the curves. This process is shown (oversimplified) schematically in Fig. 3-4 with open black rectangles representing the area beneath the loading curve, and the filled in red rectangles representing the area beneath the unloading curve.

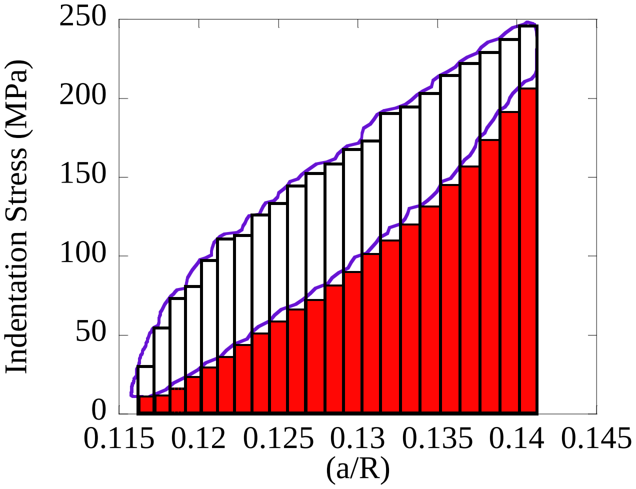

Figure 3-4. The area of an indentation stress vs. a/R loop, W_d, was calculated by approximating the area below the loading (black rectangles) and unloading (red filled rectangles) curves using sequences of rectangle partitions, and taking the difference as the area of the loop. The width of each rectangle corresponded to the change in contact radius as a function of time in increments of 0.2 s. W_d represents the energy dissipated per cycle per unit volume.

3.3 FIB, TEM and AFM

Cross-sections of select indents were lifted out using a standard lift out procedure, which included depositing a protective Pt layer ~ 1 μm thick, milling using beam currents ranging from 30–5,000 pA, and welding the sample to a copper omniprobe grid (see Fig. 3-5a). Depending on the size on the indent, lift outs, which included the entire indent and part of the surrounding matrix, ranged between ~ 10 μm to > 30 μm in width. Once a sample was welded to a grid, the sample was thinned to electron transparency (~ 100 nm thick) for TEM analysis. The energy typically used for FIB work was 10–12 kV, with a spot size 3. In Mg, orientation data was collected using 200 kV in nanobeam mode with a 15 nm spot size and a 5 nm step size. Images were taken at 200 kV using bright field, weak beam bright field, and weak beam dark field depending on the image. Weak beam bright field was used to image dislocations which appeared in contrast under the appropriate diffracting conditions.

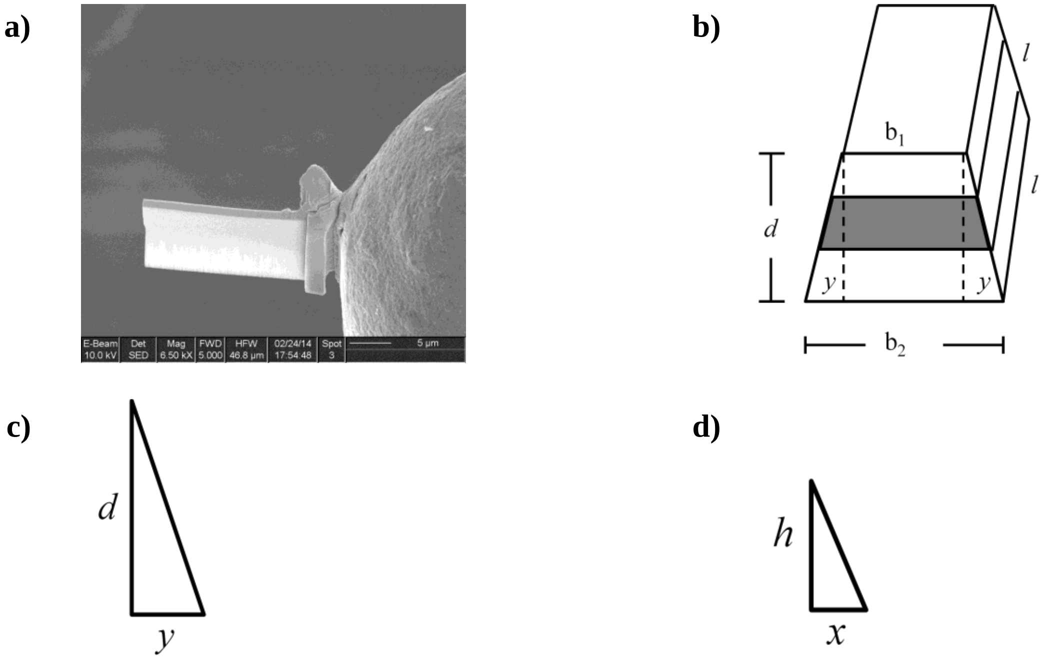

Figure 3-5. a) Typical lift out of indent cross section welded onto copper omniprobe grid. b) Schematic of indent cross sectional, which was assumed to have a trapezoidal shape. c) Right triangle with height *d* and width *y* used to approximate the taper of the foil at arbitrary depth, *x*. d) Triangle with dimensions *h* and *x* is similar to triangle in (c). Thus, the value for *x*, which is the taper at an arbitrary depth, *h*, is determined using similar triangles.

Dislocation analysis and density calculations were done on, mostly, Mg specimens, to better understand the microstructure beneath the indents. To calculate the dislocation density within the TEM samples, the thickness of the sample had to be determined. The thickness was approximated based on the foil geometry and a few assumptions. The first assumption that was made was to consider the foil to have a trapezoidal cross-sectional shape, as shown in Fig. 3-5b. The taper on either side of the top of the indent was assumed to be the same. From here, the widths across the top and bottom of an indent were measured in the FIB to give the dimensions (b_1 and b_2) of the top and bottom bases of the trapezoid. Measurements made using the FIB were corrected to compensate for the -2 % error in measurements using built-in software. The depth of the lift out was approximated using the FIB as well.

Since the taper was assumed to be the same on either side of the wedge-shaped lift out, the width of the taper, y, was determined using the dimensions of the trapezoid:

$$y = \frac{(b_2 - b_1)}{2}\,. \tag{3-12}$$

A right triangle (see Fig. 3-5c) with height equal to the depth of the indent, d, the width of the taper, y, and the length of slope of the taper, s, was used to determine the width of the taper, x, at an arbitrary height, h, using similar triangles (see Fig 3-5d). Once x was determined for an arbitrary h, the length of the base at the height h was determined. This process was repeated for two heights (h_1 *and* h_2) to yield the top and bottom bases of a trapezoid, b_1' and b_2', which represented the cross section of the localized region that was analyzed in the TEM. The area of this trapezoid was computed and multiplied by the length of the region examined to yield the volume. Finally, this volume was used in dislocation density calculations by dividing the total dislocation line length within a TEM micrograph by the calculated volume yielding an approximate dislocation density.

AFM data were collected at select locations on Ti_3SiC_2 in contact mode. An area approximately 25x25 μm around an indent was scanned, and height profile measurements were analyzed to investigate the surface around inside the indented region and around an indentation. Typically the changes in height on the MAX phases were below the resolution limit of the SEM, therefore AFM was used to study these surface effects (see Ch. 6 on MAX phases).

CHAPTER 4: MAGNESIUM

4.1 Background

Bulk Mg has been shown [35] to deform preferentially by basal slip or twinning when different slip or twinning systems are activated. Studies [36-43] on Mg single crystal to better understand the deformation modes have revealed that deformation mechanisms in Mg are a complex association of slip systems with <*a*>, <*c*> and <*c+a*> Burgers vectors.

Shin et al. [36] investigated nanoindentation on Mg single crystal in different crystal orientations and show that different slip systems are activated depending on the crystal orientation, and concluded that tensile twin formation sometimes accommodates the strain induced by nanoindentation. The anisotropy of Mg plays a key role in the activation of slip or twinning systems. Kitahara et al. [44] investigated the anisotropic deformation of Mg single crystals under spherical indentation by studying the deformation structures and concluded that the interaction between basal slip and twins determined the morphology of indentations, and that elliptical indentation morphologies resulted from the anisotropic activation of basal slip and twin systems. Similar to the work herein, Catoor et al. [45] indented Mg single crystals of different orientations using a 3.3 µm hemispherical tip. For the (0001) orientation, it was concluded – based on TEM observations of dislocations below the indent and an estimate of the geometrically necessary dislocation density – that more than 90% of the plastic deformation must be accommodated by basal slip. Some <c+a> slip was observed, but could only account for a minor fraction of the total deformation.

The active twinning modes in Mg are the $\{10\bar{1}2\}<\bar{1}101>$ and the $\{10\bar{1}1\}<10\bar{1}\bar{2}>$ extension and contraction twins respectively [15, 16, 46]. Whenever the $\{10\bar{1}1\}$ contraction twin has been observed in Mg, it has been the result of double twinning. Barnett [47] performed conventional tension and compression tests on Mg alloy AZ31 bulk samples. It was suggested that $\{10\bar{1}1\}$ and $\{10\bar{1}2\}$ double twinning, which accounts for c-axis contraction, may cause a decrease in uniform elongation in Mg and its alloys, and that double twinning may cause shear failure at low strains in Mg and its alloys as a result of strain softening and local twin sized voids.

While twinning has been observed in bulk samples, there is question as to whether or not Mg deforms by twinning or perhaps by kinking at smaller length scales. Zhou et. al [25] investigated the deformation behavior of polycrystalline Mg, and concluded that Mg could deform up to at least 4% strain by activation of basal slip alone by mobile dislocation walls and kink band formation. From this study, Mg was classified as a KNE solid.

Twinning is believed to be another possible mechanism responsible for the hysteresis loops in stress-strain curves for Mg under cyclic loading. Mann et al. [48] loaded sand cast Mg to 4% strain in compression and unloaded to study the hysteresis loops that developed, and concluded that the loops developed progressively after a plastic strain of 0.0001 and the hysteresis effect was the result of the partial reversibility of $\{10\bar{1}2\}$ twins. Partridge and Roberts [49] investigated the movement of twin boundaries in Mg single crystal under micro-indentation and concluded that the stress required to move a twin boundary is much less than the stress required to nucleate new twin boundaries. Dislocations were believed to be more easily nucleated at the twin boundary-matrix interface than the surrounding matrix, which accounts for the bowing out of twins [49].

In 2009, Capolungo et at. [50] investigated twin-thickening mechanisms in hcp metals and applied their model to Mg. It was concluded that $\{10\bar{1}2\}$ twin thickening in Mg was independent of slip, which is consistent with the notion that dislocation interactions with this twin type in Mg is repulsive [14]. The exact role that deformation twinning in Mg plays in the reversible stress-strain loops remains open to investigation.

4.2 Sample preparation of Mg single crystals

A Mg (99.8% metal basis, Alfa Aesar) rod was cut in pieces and placed in top of a MAX phase preform (Ti_2AlC) inside of an alumina crucible and heated in a graphite-heated vacuum furnace to 750° C for 1 h. Figure 4-1 shows a schematic of this set up. The inside of the alumina crucibles were lined with graphite foil to avoid reaction between the Mg and alumina. Alumina disks were used to cover the crucibles. The low pressure inside the chamber allowed for evaporation and condensation of the Mg, which led to the nucleation and growth of a multitude of Mg single crystals – as byproducts of infiltration experiments – of the order of 0.5 mm with a variety of orientations. Energy dispersive spectroscopy (EDX) confirmed that the single crystals used in this work were pure Mg.

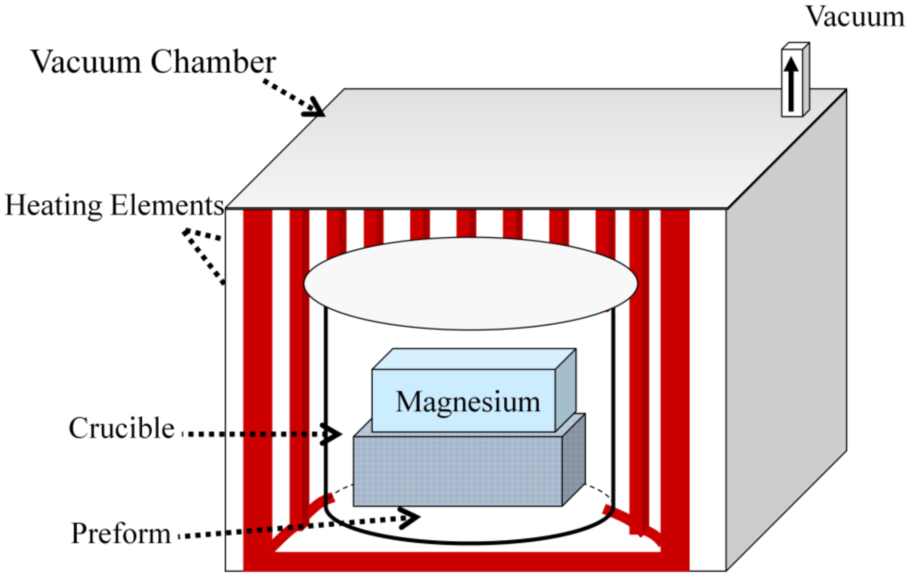

Figure 4-1. Experimental set up of infiltration experiments, in which pure magnesium was placed on top of a Ti_2AlC perform inside an alumina crucible and heated in a vacuum chamber with graphite heating elements. The chamber was heated to 750° C for 1h, and Mg single crystals formed upon cooling as a byproduct of infiltration experiments.

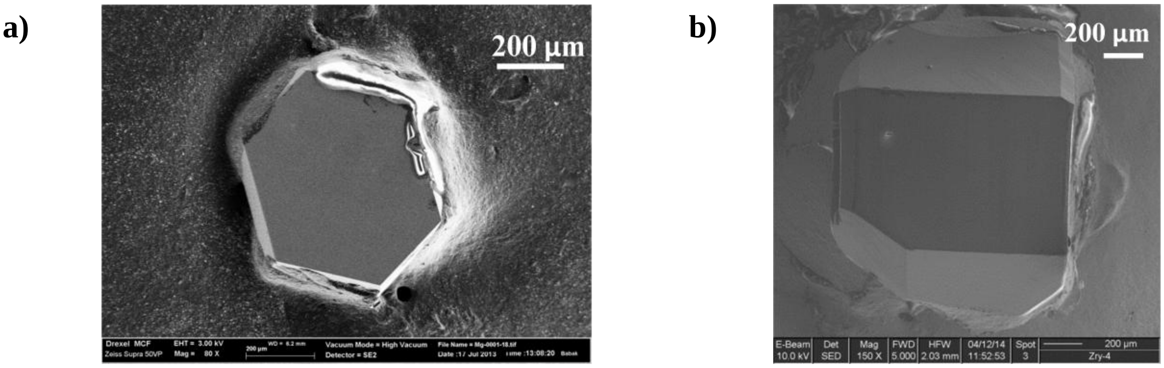

Figure 4-2. SEM images of Mg single crystals with, a) hexagonal symmetry and, b) on the prismatic face, both mounted on an Al mount using silver paint.

For this work, the focus was on selecting crystals in which the basal planes were mounted perpendicular, or parallel, to the loading direction. Said otherwise, single crystals with a hexagonal or rectangular symmetry (Fig. 4-2) were chosen and mounted so that loading was either applied on the (0001) plane, or on the side of the hexagonal crystal on the $(10\bar{1}0)$ plane. In the latter, the basal planes were loaded edge on. The surfaces of these crystals were quite shiny which permitted nanoindentation (NI) experiments to be performed without any polishing whatsoever. Since polishing was not required on this soft material, the likelihood of damaging the surfaces in the sample prep process was eliminated.

4.3 Nanoindentation experiments

Repeated NI experiments were performed in continuous stiffness mode (CSM) using a hemispherical indenter with a radius of 100 μm. The loading rate corresponded to a strain rate of 0.1 s^{-1}. Each test consisted of loading to a maximum load and unloading to a minimum load of 5 mN for 25 or 50 times in the same location followed by 5 incremental cycles loaded to approximately 20% – 100% of the maximum load with 20% load increments. The latter cycles resulted in a series of nested loops that were further analyzed. A total of 10 locations (see Table 4-2) were investigated on the same Mg single crystal using maximum loads 50 mN and 150 mN.

Similar experiments were also performed on a separate Mg single crystal in which loading was applied to 80 mN and 300 mN for 50 cycles; however, the focus of the NI results in this study was on the 50 mN and 150 mN series since drift could not be corrected very well at any location in the series loaded to 80 mN or 300 mN in the (0001) orientation. Typically, a minimum number of cycles are required to achieve an equilibrium microstructure before reversibility is achieved. The number of cycles depends largely on the material, and based on experimental observations, reversibility is achieved around 10 cycles in Mg. Hence, the number of cycles used was to ensure that reversibility would be achieved within this study.

Table 4-1. Summary of nanoindentation experiments performed in this work. Series A and B compare results using the same number of cycles at different loads, while series B and C compare results at the same load for different cycle numbers. In series A-C, loading was applied normal to the (0001) plane. Series D and E were performed to study the effect of orientation and compare results with series A-C. Loading was applied on the $(10\bar{1}0)$ plane at locations in series D and E.

Orientation	**Series**	**Load (mN)**	**Location**	**Cycles**
(0001)	A	50	1	50
		50	2	50
		50	3	50
		50	4	50
	B	150	1	50
		150	2	50
		150	3	50
	C	150	1	**25**
		150	2	**25**
		150	3	**25**
$(10\bar{1}0)$	D	80	1	50
		80	2	50
		80	3	5
	E	100	1	50
		100	2	50
		100	3	50

The contact radii of all 10 locations in series A-C were measured in the dual beam FIB-SEM. For the most part the indentation marks on the (0001) plane were found to be quite circular (Fig. 4-3a). To better understand what was occurring microstructurally below the indenter, cross sections of indents in both orientations were lifted out using a FIB and examined using a TEM. Dislocations beneath the indent were later identified using the same technique used by Agnew et al. [39], with g = [0002].

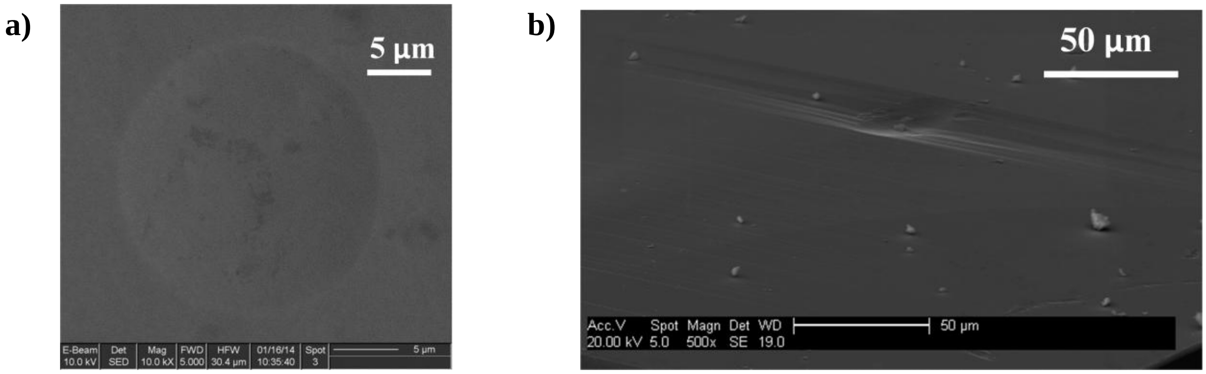

Figure 4-3. SEM image of, a) indent made on the (0001) plane and, b) indent made on the $(10\bar{1}0)$ plane of Mg single crystal.

On a separate crystal, loading was applied parallel to the basal planes and a SEM equipped with EBSD was used to generate an orientation map of an indentation to better understand the orientation change beneath the indent. Figure 4-3b shows a typical indentation on the $(10\bar{1}0)$ plane, which is not perfectly circular, but more oval shaped. Instrumental drift could not be corrected in the same manner as indentation on the (0001) plane as a result. Instead, for this data series, drift was corrected by first plotting each load vs. displacement cycle separately in the same figure (Fig. 4-4) and comparing the cycles to one another. When the load vs. displacement cycles appeared to be near to identical, they were shifted and superimposed to verify they were indeed identical. Raw load vs. displacement data was shifted to that particular cycle at which permanent deformation no longer resulted to correct for drift. Some TEM lift outs were also examined beneath indents made on the $(10\bar{1}0)$ plane.

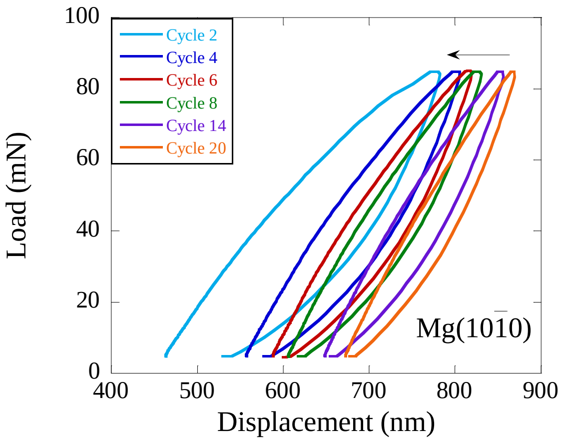

Figure 4-4. Load vs. displacement cycles plotted separately in same figure. The cycles were compared and later shifted to the left to account for drift when indenting on the prismatic face on Mg single crystal.

4.4 Results on (0001) plane indentation

4.4.1 Nanoindentation on (0001) plane

Figure 4-5a plots the load-displacement curves for two locations - 2A and 2B (see Table 4-1) - loaded to 50 and 150 mN, respectively. The load-displacement curves for cycles 5, 45 and 50 are compared in Fig. 4-5b. When the maximum load was 50 mN, and with the exception of a small shift to the right, cycles 5, 45 and 50 were identical. When the maximum load was 150 mN, cycles 45 and 50 are so reproducible that they are indistinguishable, and both are stiffer than the 5th cycle (see Fig. 4-5b).

Figure 4-6a plots the indentation stress vs. a/R curves for the two locations shown in Fig. 4-5a. Figure 4-6b compares the indentation stress vs. a/R curves for a location loaded to 150 mN, 25 times (2C in Table 4-1) to location 2B. From these and other results it is clear that: i) For most locations, the initial response was linear elastic, with a slope that corresponded to a modulus of ~ 61 GPa; ii) Pop-in events occurred at stresses in the range of ~ 280 MPa to 450 MPa; iii) Past the pop-ins, the stress drops to approximately 275 MPa and then slowly increases with further displacement into the surface. In this region, the hardening rate is of the order of 700 MPa. The pop-in event that occurred during the first loading cycle is an indication of homogeneous dislocation nucleation in an area of the crystal that had a low defect density initially. Catoor [45] et al. concluded that the pop-in events were due to the nucleation of basal dislocations in the 0001 orientation.

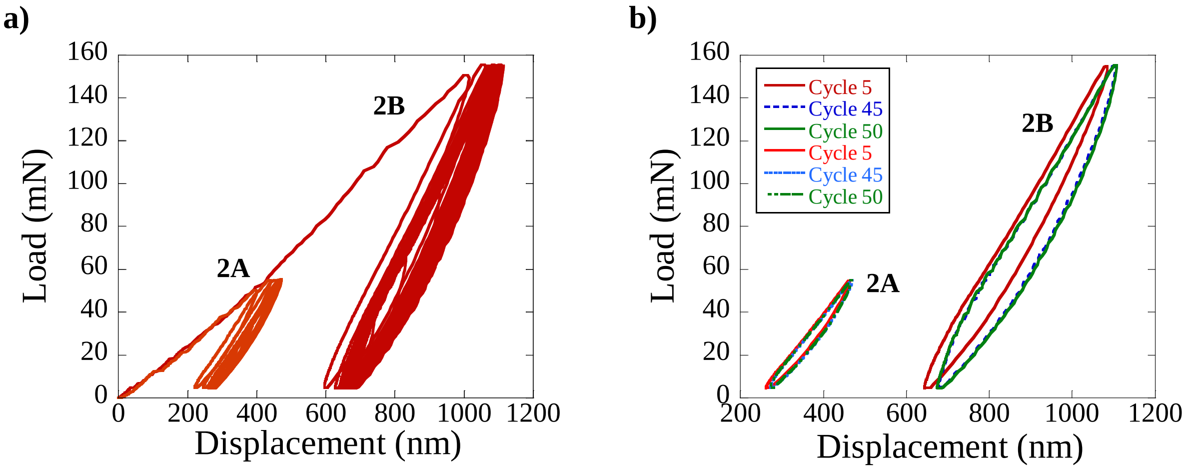

Figure 4-5. a) Load vs. displacement plot of indents loaded to 50 mN and 150 mN from series A-B. b) Load vs. displacement cycles from the latter portion of a single experiment are compared with cycle 5 from the same experiment. Note that in these two cases, the instrumental drift was negligible and no corrections were needed.

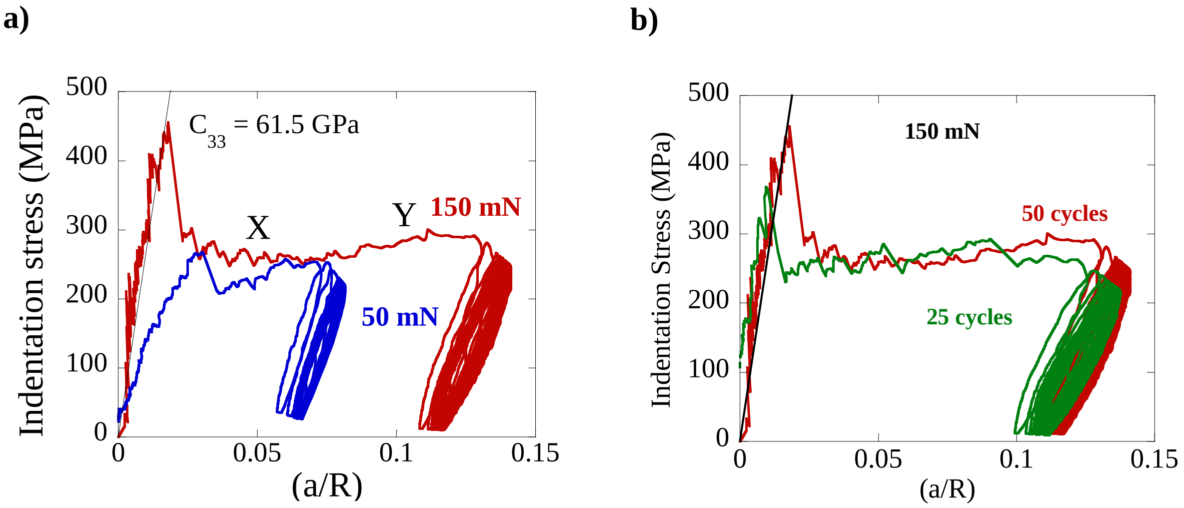

Figure 4-6. a) Indentation stress vs. a/R plots for locations loaded to 50 and 150 mN, 50 times and fitted to the solid inclined line corresponding to an elastic modulus of 61.5 GPa. b) Indentation stress vs. a/R plots for locations loaded to 150 mN, 25 and 50 times.

Note that the a/R values in series B and C were essentially the same: around 10-11% for each location (see Fig 4-6b). In series A, however, loaded to only 50 mN, a/R was around 6.5 % for each location. In other words, a/R was more or less independent of the total number of cycles, but dependent on the maximum loads.

Figure 4-7 plots the nested sequence of NI stresses vs. a/R for three locations loaded to: i) 50 mN for 50 cycles (2A in Table 4-1), ii) 150 mN for 50 cycles (2B in Table 4-1) and, iii) 150 mN for 25 cycles (2C in Table 4-1). These locations will henceforth be referred to as locations I, II and III, respectively. A comparison will first be made between the nested loops I and II cycled to 50 cycles each. These curves, like all other locations, are characterized by a linear elastic region, depicted by thin dashed inclined lines, whose slope is identical to that predicted from Hertz's relationships assuming $E = c_{33} = 61.5$ GPa (see Ch. 3).

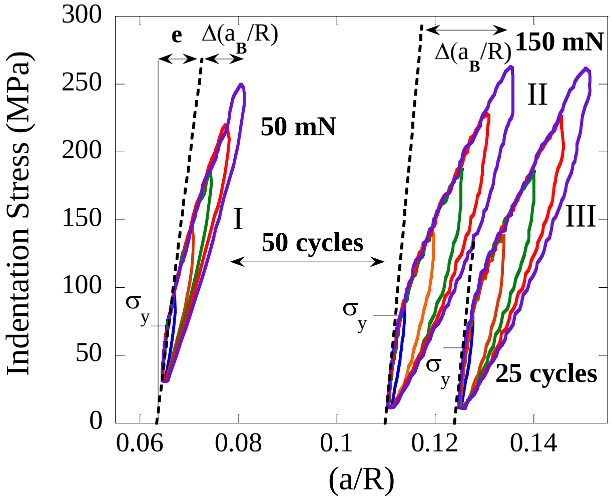

Figure 4-7. NI stress vs. a/R plots for locations loaded to, I) 50 mN, 50 times, II) 150 mN, 50 times and, III) 150 mN, 25 times. Dashed near vertical inclined lines are those corresponding to an elastic modulus of 61.5 GPa. The total change in contact radius (divided by the indenter radius R) at maximum loading is the sum of a linear elastic change labeled e and a nonlinear change given by Δa_B. In the plot, σ_y represents the yield stress of each nested sequence.

At a yield stress, σ_y, there is a change in slope that also corresponds to the emergence of the fully, and spontaneously, reversible indentation stress vs. a/R loops. When the load is removed, the NI stress vs. a/R curves return to the point of initial loading, completing the loop. As in previous work, the loading trajectory is identical in all cases [51]. By averaging σ_y for each location within each series, (see Table 4-2) the average threshold stress after 50 cycles were ~ 62.5±0.5 MPa and ~ 67±0.5 MPa after the 50 mN and the 150 mN indents, respectively.

Comparing loops II and III in Fig. 4-7 it is obvious that increasing the number of cycles results in slightly higher σ_y values and a general stiffening of the loops. The average threshold stress for the 150 mN indents were ~ 57.6±2 MPa and ~ 67±0.5 MPa after 25 and 50 cycles, respectively. Gratifyingly, the slopes of the linear elastic regimes are not a function of the number of cycles or applied load. The hardening rates in Table 4-2 are shown for each location in series A-C corresponds to the non-linear elastic regime, for stresses > σ_y in the nested cycles.

Table 4-2. Contact radius for different locations after the 1st cycle and last cycles, together with the value of a measured in the SEM, a_{SEM}. The yield stress, σ_y, for each location in the nested sequences is also shown in the table. The hardening rates of the nested loops are listed in the last column. The plots shown in Fig. 4-7 correspond to locations labeled I, II and III. Entries labeled t, were measured from titled images along with applying the automated tilt correction factor within the FIB-SEM measurement software. This was done since the faint outline of these indents from their top view made measurements difficult.

Series	**Load (mN)**	**Cycles**	**Loc.**	**1st (μm)**	**Last (μm)**	**a_{SEM} (μm)**	**σ_y (MPa)**	**Fig. labels**	**Hard. Rate (GPa)**
A	50	50	1	6.0	6.9	6.6 ± 0.3	62		10.8
A	50	50	2	6.5	7.4	6.5 ± 0.3 (t)	64	I	11.2
A	50	50	3	7.7	8.5	6.4 ± 0.3 (t)	63		9.4
A	50	50	4	7.6	8.4	6.4 ± 0.03	62		13.3
B	150	50	1	10.2	10.7	10.4 ± 0.2	67		10.0
B	150	50	2	10.8	11.7	11.1 ± 0.2	67	II	7.7
B	150	50	3	10.8	12.2	11.1 ± 0.2	68		7.7
C	150	25	1	11.9	13.2	10.9 ± 0.2	55		7.8
C	150	25	2	11.2	12.8	11.0 ± 0.2	59	III	7.6
C	150	25	3	11.4	13.2	11.1 ± 0.1	59		7.7

Loops II and III in Figure 4-7 also compare the effect of the number of cycles on the NI stress vs. a/R curves. In this case, not surprisingly, the strain hardening rates for locations loaded 50 times, are very similar, if not the same as than those loaded 25 times, with a small increase in hardening rate from 7.6 to 7.7 GPa. Note that this implies that the cycling is not 100% reversible. Intriguingly, however, when the locations loaded to 50 mN and 150 mN are compared (compare loops I and II in Fig. 4-7), the strain-hardening rate for the latter, at 11.2 GPa, is *higher* than that of 150 mN at 7.7 GPa. More work is certainly needed to understand this counterintuitive result.

Turning attention back to the nested cycles (Fig. 4-7), the total strain during a given cycle is given by:

$$\Delta\frac{a_{tot}}{a_o} = \Delta\frac{a_{el}}{a_o} + \Delta\frac{a_B}{a_o} \tag{4-1}$$

where a_o is the indentation radius at zero load and the first term on the right hand side is the linear elastic strain, denoted by e in Fig. 4.7. The second term is the non-linear elastic strain. In Fig. 4-7, e represents the ratio of *indent radius due to elastic strain* to the indenter radius, R, and $\Delta a_B/R$ represents the ratio of the *indent radius due to non-linear strain* to R.

Like previous work on KNE solids [13, 24-26, 30, 52, 53], Figure 4-8a plots the NI stress squared, i.e. σ^2 vs. $\Delta a_B/a_o$; Figure 4-8b, plots W_d vs. $\Delta a_B/a_o$ for two locations loaded to 50 mN (red circles) and 150 mN (green triangles) for 50 cycles, and one location loaded to 150 mN for 25 cycles (blue squares). Least squares fits of the results resulted in $R^2 > 0.99$, indicating a good fit to a straight line.

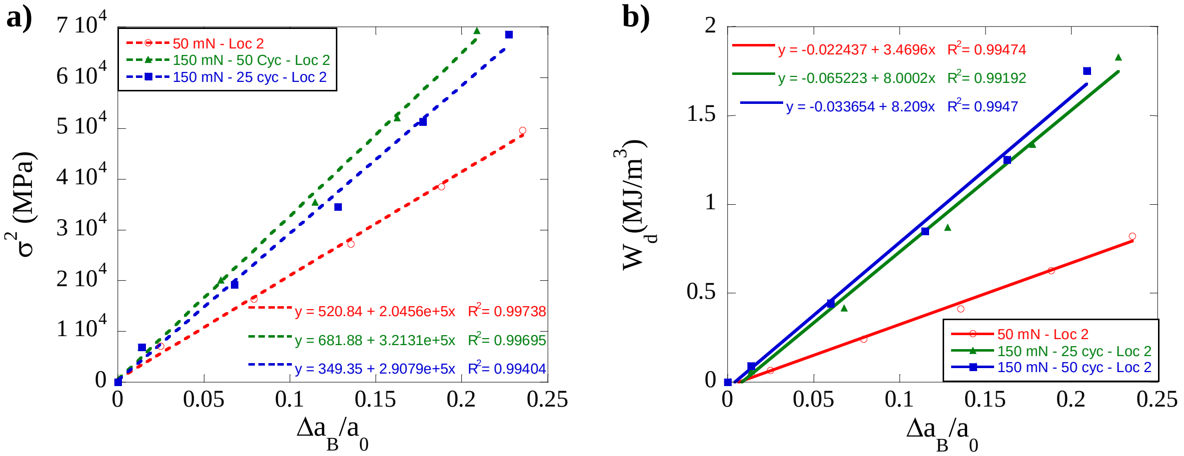

Figure 4-8. $\Delta a_B/a_o$ is plotted against, a) σ^2 and, b) W_d for the nested cycles loaded to 50 mN (open red circles) and 150 mN for 50 cycles (solid green triangles) and 150 mN for 25 cycles (solid blue squares). The values for R^2 are indicative of a reasonably good fit. The straight lines in b) have slopes $2\Omega\sigma_y\theta$ for a given series (see text).

4.4.2 TEM beneath (0001) indents

Three TEM liftoffs were prepared, one each for locations loaded to 50 mN and 150 mN on the same crystal, and one for a location loaded to 80 mN on a separate crystal on the (0001) plane. While the NI data was unusable due to abnormal drift for the 80 mN indent, the TEM observations remain valid. In every case, a low angle kink boundary, LAKB, separated the parent crystal from the indented region (top inset Fig. 4-9a). The KBs were perpendicular to the basal planes. A diffraction pattern across the boundary (lower inset in Fig. 4-9a) showed a slight misorientation. The misorientation angles, θ, were 3°, 4° and 6° for the indents loaded to 50, 80 and 150 mN, respectively. When imaged at higher magnifications (Fig. 4-9a), individual basal dislocations in the LAKB were discernible and could be counted. Since these dislocations make up the boundary between regions of different orientations, these dislocations are geometrically necessary dislocations. From the micrographs, the average dislocation spacing, d, in the 3°, 4° and 6° boundaries were, respectively, 12*c*, 8c and 6*c* - where *c* is the c-lattice parameter. The kink angle, γ_c, was plotted against the contact radius (Fig. 4-9b) for each location and fitted to a line through the origin. While more data points are certainly needed at various loads, the linear correlation shows a good fit to the data points from this study with $R^2 > 0.98$.

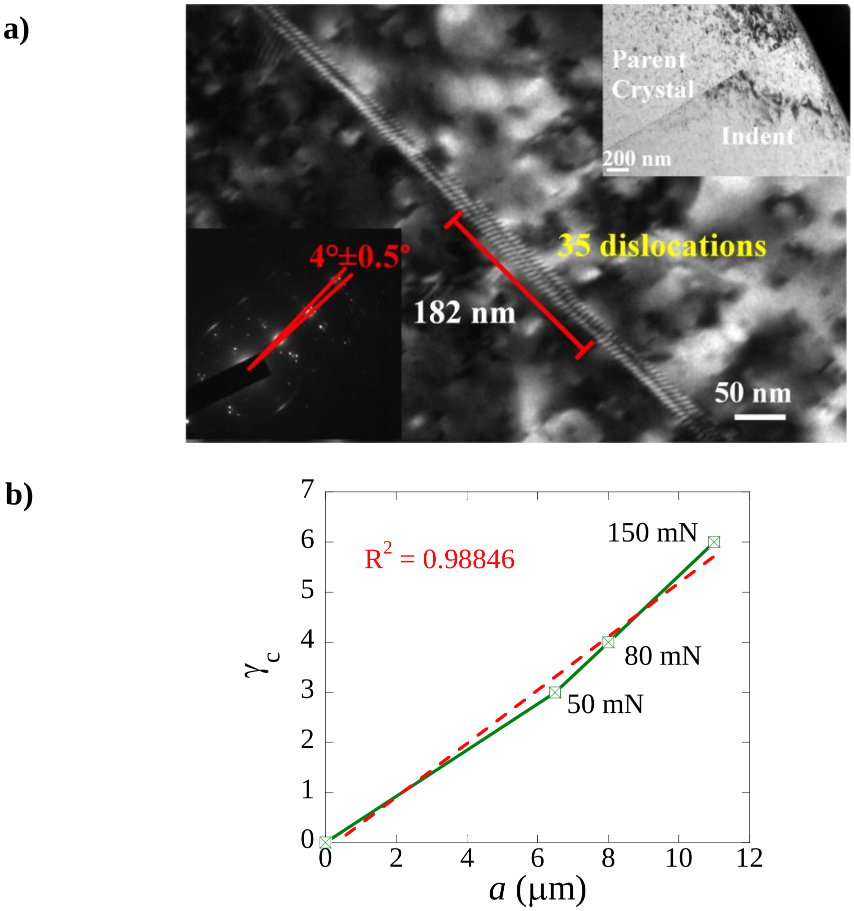

Figure 4-9. a) Cross-sectional TEM lift out of location loaded to 80 mN, wherein individual basal dislocations can be discerned. The distance between dislocations, d, is measured to be 8c where c is the lattice parameter. Thus b/d equals 4.35°, which is excellent agreement with the value measured from the SAED (lower inset). Top inset shows a low magnification TEM showing the location of the LAKB at the edge of the indent. b) The kink angle, γ_c, was plotted against the contact radius for the three indents loaded to 50 mN, 80 mN and 150 mN and fitted to a line. The point at the origin was included and the linear correlation resulted in $R^2 > 0.98$.

If one assumes the Burgers vector, **b**, to be 0.321 nm, and $\theta = b/d$, then the corresponding misorientations are – using the values of d measured from the TEM micrographs - calculated to be 2.9±0.5°, 4.35±0.5° and 5.8±0.5°. These values are in excellent agreement with those measured from the diffraction patterns. This result is important because it indirectly confirms that the dislocations are basal and that their Burgers vector is indeed 0.321 nm.

The other crucial observation is the fact that only *one* LAKB was observed in all cases, which unequivocally proves that these boundaries move with the indent edges (top inset in Fig. 4-9a). Said otherwise, the LAKB are mobile. Catoor et al.[54] – who also studied Mg single crystals with a spherical indenter - did not report the presence of LAKBs. However, since these authors did not cycle their load, it is reasonable to ascribe the discrepancy to the fact that some cycling is needed to render the LAKBs visible. For the 000l orientation they concluded – based on TEM observations of dislocations below the indent – that more than 90% of the dislocations beneath the indent were basal dislocations. Some <*c* + *a*> slip was observed, but could only account for a minor fraction of the total number of dislocations.

Figure 4-10a-b shows a bright field image of dislocations in contrast under the appropriate diffraction conditions beneath a 100 μm spherical indenter loaded to 50 mN and 150 mN. Since the 150 mN indent was more heavily deformed, dislocation analysis was done on the 50 mN indent to ensure more accuracy of results. Basal dislocations, with <*a*> Burger's vector as well as <*c* + *a*> dislocations were identified as seen in Fig. 4-10a, with a larger density of <*a*> type dislocations. This observation is consistent with those made by Catoor [45] et al. in which basal dislocations were more prevalent than <*c* + *a*> dislocations under a 3 μm spherical indenter. Under an applied load normal to the basal planes, c-axis strain must be accommodated either by the activation of <*c* + *a*> dislocations or twins. Twins were not observed beneath any indents loaded on the (0001) planes. Therefore, one has to conclude that c-axis displacement was accommodated by dislocations with a <*c* + *a*> Burgers vector.

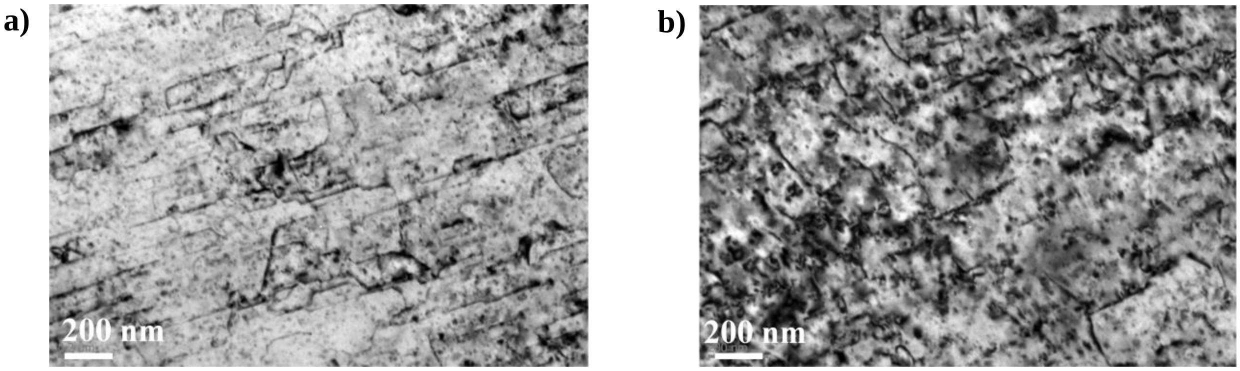

Figure 4-10. Dislocations are imaged using weak beam bright field beneath, a) 50 mN indent approximately 4 μm beneath the surface loaded for 50 cycles, and b) a 150 mN indent loaded for 25 cycles. The 150 mN indent appears to be more highly deformed.

To accommodate the shape change under a NI, in addition to statistically stored dislocations, SSD, geometrically necessary dislocations, GNDs, (shown schematically in Fig. 4-11a as green T's and red inverted T's, have to be nucleated). The density of the latter, ρ_{GND}, can be estimated from the LAKBs surrounding the indents since the dislocations in the boundary are GNDs. Given that $\theta = b/d$, and assuming that the LAKBs extend to a distance of $2a_o$ in the form of a cylinder, into the bulk (Fig. 4-11a), it follows that:

$$\rho_{GND} = \frac{2}{a_o d} = \frac{2}{a_o b}\theta \tag{4-2}$$

Thus, for indentation loads of 50, 80 and 150 mN, ρ_{GND} is estimated to be 6×10^{13}, 5×10^{13} and 6×10^{13} m^{-2}, respectively. It is crucial to note here that the signs of the GNDs under the indenter (colored green in Fig. 4-11a) have to be *opposite* of the ones in the LAKBs (colored red in Fig. 4-11a), that have, in turn, to be all the same sign. During the deformation process, they have to form in equal numbers.

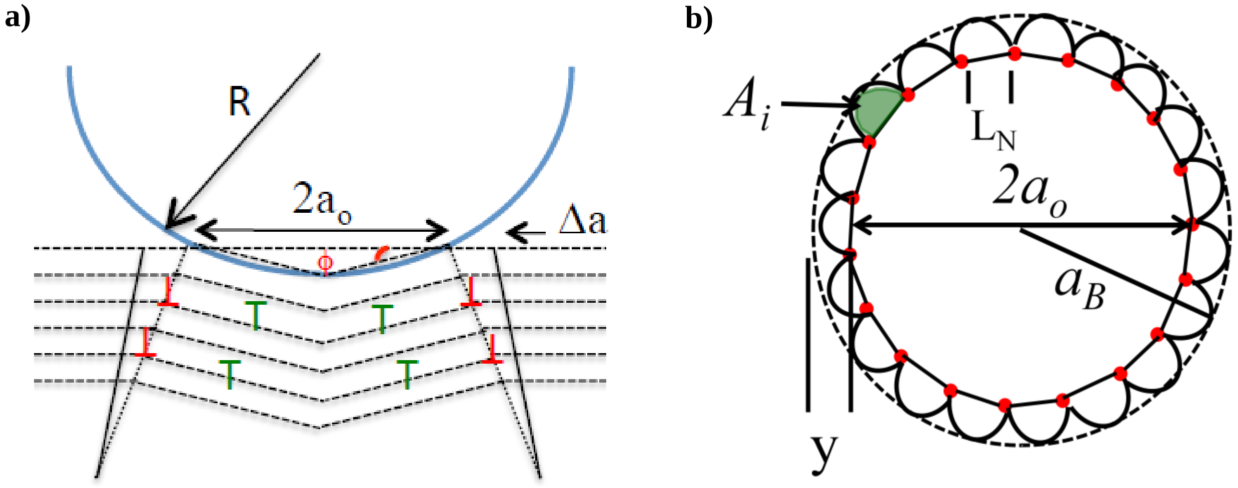

Figure 4-11. a) Schematic of cross-section of spherical indentation along [0001] in Mg. Dashed lines represent basal planes. The T's represent dislocations in LAGBs (red) and GNDs under the indenter (green); they must be of opposite sign. The angle across LAKB is θ and varied from 3° to 6 ° in this work. When the load is applies, the near vertical dashed lines move outwards to their new position given by the solid lines. The distance they move is Δa. b) Top view of indentation where the LAGBs are assumed to form a circle with diameter $2a_o$. When the surface is loaded, the dislocation segments of lengths L_N grow to a radius $y = \Delta a$; when the load is removed they revert to their initial configuration. A_i is the area shown in green.

As a rough approximate to the dislocation density, the total dislocation line length was divided by the volume giving an estimate dislocation density. A more accurate density would require tilting the sample to cause more dislocations to appear in contrast, which was not done in this study. Details for approximating the thickness of the TEM samples and the method for calculating the dislocation density were discussed in Ch. 3. The calculated dislocation densities underneath the crater of indents 4A and 1C (see Table 4-1) are listed in Table 4-3.

Table 4-3. Dislocation densities for indents 4A and 1C. The calculations underneath the indent were based on the average dislocation length divided by the volume. *Since indent 1C was heavily deformed, some dislocations were not accounted for when calculating the density within the indent. Thus, the dislocation count is considerably lower by at least an order of magnitude at this location.

Sample	Location	Dislocation Density (m^{-2})
4A	Indent	1.3×10^{13}
	Boundary	4.8×10^{13}
1C	Indent	*9.2×10^{12}
	Boundary	1.05×10^{14}

4.4.3 Dislocation bowing model

At this juncture the requisite information has been attained to make the following important hypothesis: It is the bowing out of GNDs, in the form of LAKBs, through SSD that is responsible for the energy dissipated per unit volume per cycle, W_d. This is best evidenced by understanding that the physics of what is occurring to produce the nested loops must be *different* than the physics is occurring during the classic work hardening regime, i.e. in moving from X to Y in Fig. 4-6a, for which the work hardening rate is 700 MPa. In contradistinction, at ≈ 7,766 MPa, the hardening rates within the cycles – i.e. the slope of the top portion of each loading cycle in Fig. 4-7 – are at least *an order* of magnitude higher. Since the hardening rate for the long range movement of the LAKBs through the SSDs is ≈ 700 MPa, it follows that the much higher hardening rates observed during cycling is most likely related to the bowing out of GNDs in the LAKBs. While this is not the only possibility, it is the most plausible possibility. The same conclusion was reached - viz. that the W_d they measured was due to the bowing of dislocations - by Roberts et al. [55, 56] when they deformed single crystals of Zn and Mg. Figure 12 shows some results obtained Roberts et al. [55, 56] from their study on Mg. Note that in their work the plastic strains were quite small and that since the work was on single crystals that were loaded along an easy shear direction, the relationships plotted in Fig. 4-12 may be characteristic of dislocation-dislocation interactions.

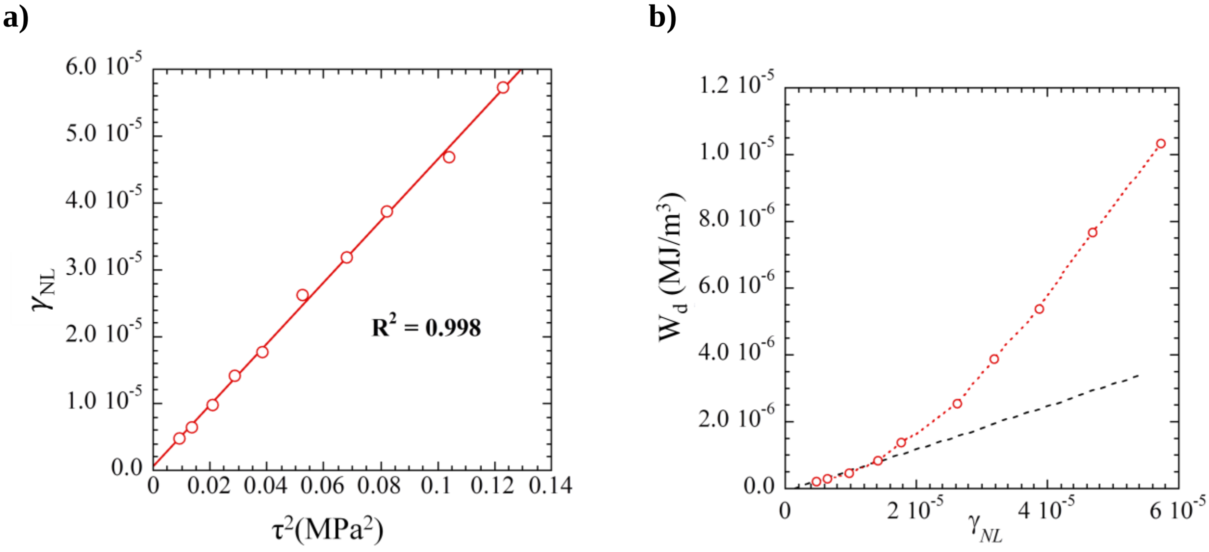

Figure 4-12. a) γ_{NL} vs. τ^2, and, b) W_d vs. γ_{NL}. All results extracted from Fig. 3 in Ref [55].

The following calculations are consistent with this idea. The shear strain, γ_B, associated with dislocations bowing in a network is given by [56]:

$$\gamma_B = \sum_{i=1}^{n} \frac{bA_i}{V} \approx \frac{nbA_i}{V} = \frac{b r_{av} \rho_{GND}}{2} \tag{4-3}$$

where A_i is the area swept (shaded green in Fig. 4-11b) by the ith dislocation in a mosaic block of volume V, n is number of dislocations which bow per mosaic block and r_{av} is their average radius of curvature. Equating r_{av} to the measured change in contact radius in the non-linear regime, Δa_B (Fig. 4-7) and combining Eqs. 4-2 and 3, it can be shown that:

$$\gamma_B = \frac{r_{av}}{a_o}\theta \approx \frac{\Delta_B}{a_o}\theta, \tag{4-4}$$

where θ = b/d is the angle of the LAKB. Note Δa_B is the change in contact radius due to the bowing of dislocations. For example, Δa_B is ≈ 1 µm for the 50 mN indents (see I in Fig. 4-7) and ≈ 1.7 nm (II in Fig. 4-7) for the 150 mN indents (Fig. 4-7). The respective γ_B values calculated from Eq. 4-4 are 0.008 and 0.016. More exact values of Δa_B are used to calculate γ_B shown in Table 4-4.

Now we shift the focus to W_d, which is equal to $2\tau_f\gamma_B$ [56] where the factor of 2 accounts for the energy dissipated loading and unloading and τ_f is the energy dissipated when a dislocation sweeps a unit area by a distance b. Making use of Eq. 4-4 and noting that near the yield point - defined as the point at which the NI stress vs. a/R curves deviate from linear elasticity in Fig. 4-7 – $\sigma_y \approx \sigma_f \approx \tau_f/\Omega$, it follows that:

$$W_d = 2\tau_f\gamma_B = 2\Omega\sigma_f\theta(\Delta a_B/a_o) \qquad (4\text{-}5)$$

where Ω is a factor that relates the shear stress on the basal planes, τ, to the applied NI stress, σ.

If τ_f is not a function of stress, then plots of W_d vs. $\Delta a_B/a_o$, should yield straight lines with a slope $\approx 2\Omega\theta\sigma_y$, as observed (Fig. 4-8b). From the slopes, and noting that σ_y = 62.5±0.5 MPa for the 50 mN indent and 67±0.5 MPa for the 150 MPa indent, the *average* respective values of Ω are 0.58±0.03 and 0.61±0.02. Table 4-4 lists the values for Ω along with γ_B for each location. Given the geometry of the setup, these values are probably too high, but nevertheless quite reasonable given all the simplifying assumptions made and that fact that no adjustable parameters were used to obtain them.

Table 4-4. Calculations of Ω, L_N and the shear strain due to bowing, γ_B, are shown.

Series	**Load**	**Cycles**	**Location**	**Ω**	**L_N (µm)**	**γ_B**
A	50	50	1	0.58	0.55	0.0101
A	50	50	2	0.54	0.55	0.0102
A	50	50	3	0.58	0.49	0.0092
A	50	50	4	0.64	0.49	0.0100
B	150	50	1	0.65	0.56	0.0188
B	150	50	2	0.59	0.64	0.0183
B	150	50	3	0.60	0.65	0.0196
C	150	25	1	0.71	0.64	0.0228
C	150	25	2	0.67	0.64	0.0208
C	150	25	3	0.69	0.63	0.0202

The bowing out idea is also consistent with the stress trajectory followed by the system when the maximum stress for a set of cycles is exceeded (i.e. in going from X to Y in (Fig. 4-6a). In that case, the hardening rate reverts to ≈ 700 MPa, and at this point it is reasonable to assume that the LAKB dislocations were freed from their moorings and start irreversibly moving over reasonably large distances to their new position given by the new maximum load. For example, according to Fig. 4-6a as the applied load increases from 50 to 150 mN, the LAKB moves a distance of ≈ 5 μm (i.e. going from loops I to II in Fig. 4-7). The fact that LAKBs are mobile is well established and has been documented previously in Zn [57] and other hexagonal metals.

One of the more intriguing results of this work is the fact that $\Delta a_B/a_o$ scales with σ^2 (Fig. 4-8a). This dependence, previously expressed in terms of non-linear strain vs. σ^2 , was taken as evidence for the existence of IKBs [52, 58]. In that formalism, the number of IKBs was assumed to be constant and the σ^2 dependence was assumed to arise from IKB growing in two dimensions in the basal planes. The results of this work suggest a different reason: namely that both A_i and n in Eq. 4-3 are linear functions of σ. The simplest approach to estimate A_i is to assume Lucke and Granato's rigid rod model [59], in which dislocations are assumed to move under a shear stress, τ, as a rigid rod and displaced a distance, y, that is constant along its whole length given by [59]:

$$y = \frac{L_N^2 \tau}{12\alpha G b} = \frac{L_N^2 \Omega \sigma}{12\alpha G b} \tag{4-6}$$

where is $\alpha \approx 0.5\text{-}1.0$ and G is the shear modulus (17 GPa for Mg); L_N is the length of the dislocation segments that are unbreakably fixed at their ends (see Fig. 4-11b). In the present configuration, $y \approx \Delta a_B$, and assuming $\alpha \approx \Omega \approx 0.5$, then L_N is estimated from Eq. 4-6 to be of the order of 0.54 μm to 0.7 μm, for locations I and II the 50 mN and 150 mN indents, respectively. These numbers are quite reasonable indeed. Here again *no* adjustable parameters are used. Note that since

$$A_i \approx 2a_o y = \frac{a_o \Omega L_N^2}{12\alpha Gb}\sigma, \tag{4-7}$$

A_i is a function of σ. Knowing L_N, the normal stress needed to bow such segments to a radius of 0.5 µm is given by:

$$\sigma = \frac{Gb}{2\Omega L_N} \tag{4-8}$$

Assuming $L_N \approx 0.5$ µm, then σ is ≈ 11 MPa, which is roughly a factor of 4 smaller than the actual yield point measured. The reason for this discrepancy in not clear at this time, but could be related to the inhomogeneous state of stress under the NI and/or the fact that dislocations are bowing into a high density of SSDs.

It is now possible to describe what is occurring under the indenter as it is repeatedly thrust into Mg in the (0001) orientation. Initially, none of the L_N segments in the LAKB bow out, which is why in all cases the initial response is linear elastic (inclined dashed lines Fig. 4-7). At σ_y, some but not all, the dislocation segments start to bow. According to Eqs. 4-3 and 8, the first segments to bow out will be the longest segments for which the Schmid factor is highest. With increasing stress, more segments bow out until the maximum stress is reached. At that maximal point, the segments in the LAKB are bowed out by a distance of $y \approx \Delta a_B$ (Fig. 4-11b). It follows that to explain the dependence of $\Delta a_B/a_o$ on σ^2 one needs only assume that n in Eq. 4-2, scales with σ, here again a reasonable assumption.

Equation 4-7 is important for another reason: It implies that the nonlinear strain, given by Eq. 4-4, must be *dominated by the longest dislocation segments* since it depends on A_i that, in turn - since $a_o \approx n_x L_N$ (Fig. 4-11b) - depends on L_N^2 where n_x is the number of segments per side. This result also implies that even if the SSDs bow out, their contribution to the total strain can be safely neglected. The same is true for W_d. Note that even if the energy dissipated is due to bowing out of SSD, they can still be considered since the LAKBs are still required to allow the

SSD to bow out and thus these solids can still be described as KNE. As discussed in the next chapter, the presence of dislocations, in the absence of LAKBs does *not* lead to energy dissipation.

In summary, from the totality of the results presented in this study, it is concluded that the origin of the energy dissipated during the fully reversible hysteretic stress vs. a/R cycles observed in this, and previous, work is most probably, the reversible bowing out of GNDs, in the form of LAKBs, through statistically stored ones. This conclusion most likely applies to the vast majority of KNE solids provided they do not twin and their c/a ratio is small enough to allow for plasticity along the c-axis.

4.5 Results on $(10\bar{1}0)$ plane indentation

4.5.1 Nanoindentation on $(10\bar{1}0)$ plane

As loading was applied parallel to the basal planes, twins formed beneath the indented region as shown in (Fig 4-3b). Instead of being spherical, the indents were oval shaped with long and short axes. Figure 4-13 shows a typical OIM map using EBSD on the prismatic face of a Mg single crystal after indentation, which shows the orientation change within the twinned region. Using the OIM data analysis software, the angle of misorientation between the twin boundary and matrix was found to be ~ 86.7°±5° about [1120]. This is certainly within the tolerance of $\{10\bar{1}2\}$ tensile twins, which rotates the basal planes by ~ 86° about the $<11\bar{2}0>$ directions.

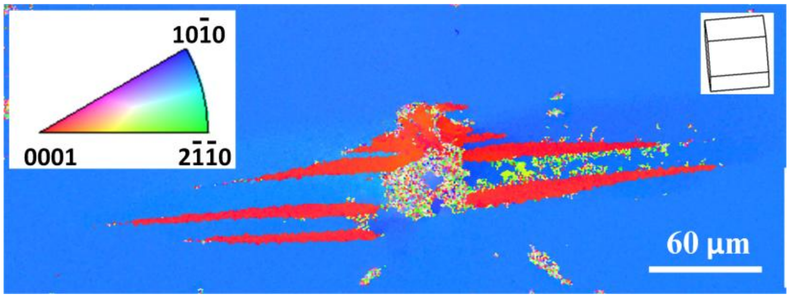

Figure 4-13. Orientation map of (10$\bar{1}$0) plane of Mg single crystal post indentation obtained using EBSD. Tensile twins are seen around the indented area, which was a typical observation when indenting on the prismatic plane in Mg.

The *drift corrected* load vs. displacement curve for a location loaded to 80 mN for 50 cycles is shown in Figure 4-14a. The load vs. displacement curve was converted to an indentation stress vs. a/R curve (see Fig. 4-14b) using the Hertz equation, as discussed in Ch. 3. Similar to observations made on (0001) plane indentation, a pop-in was observed at various locations under a sufficiently high applied stress (~ 275 – 325 MPa), which Catoor [45] et al. attributed to <a> dislocation nucleation as the first mechanism to initiate during a pop-in. The a/R values were around 10% for each location loaded to 80 mN and ~ 12% for locations loaded to 100 mN.

In Fig. 4-14b, the slope of the linear elastic region corresponds to an elastic modulus ~ 25.7 GPa, which is the elastic modulus calculated along the [1$\bar{1}$00] direction using Eq. 2-9, and the compliances for Mg (C_{11} = 59.3, C_{33} = 61.5, C_{13} = 21.4 and C_{44} = 16.4 GPa) [60]. During the first loading cycle, the crystal shows behavior consistent with the Hertz equation using a spherical indenter. The subsequent cycles showed behavior that was a better fit to the elastic modulus along the [0001] direction, which is 61.5 GPa, however. This suggests that by loading until the pop-in occurs, the indentation was likely spherical and largely indenting a single orientation. When the applied load was sufficient to induce twinning, the initial slope of the stress-strain curve upon re-loading increased from ~ 25.7 GPa to ~ 61.5 GPa. (Compare lines labeled A and B is Fig. 4-13b). As a load was applied with subsequent cycles, the mechanical response became coupled with the twins. The simplest explanation is that since the tensile twins rotate the crystal orientation by ~ 86 degrees about the <11$\bar{2}$0> directions, the indenter, on the second and subsequent cycles is going into the material that is closer to the (0001) orientation. Said otherwise, because the material beneath the indenter after the twins are nucleated is elastically harder than the initial matrix as a result of the crystal rotation, the elastic modulus must have increased.

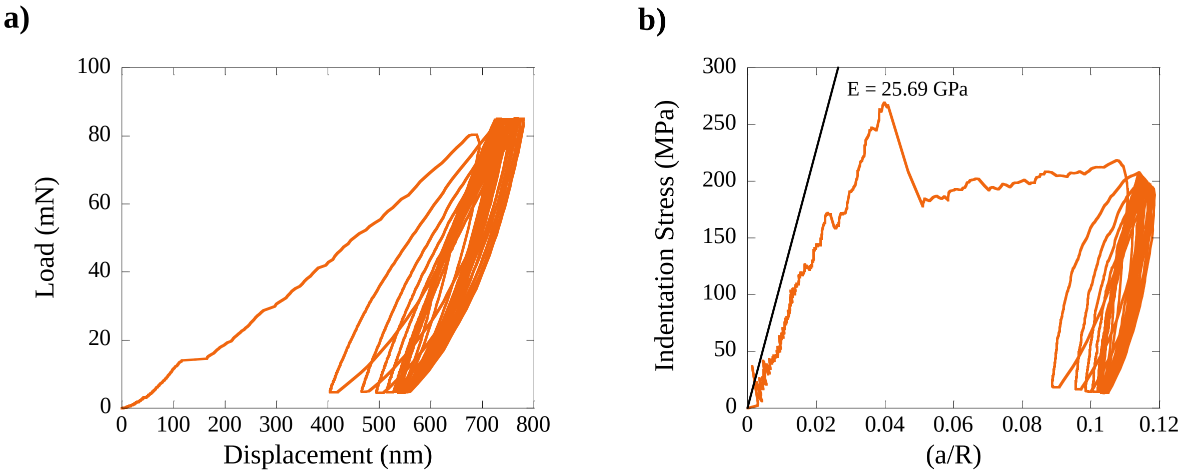

Figure 4-14. a) Drift corrected load vs. displacement plot at location loaded to 80 mN for 50 cycles along and, b) its corresponding indentation stress vs. a/R plot. Note that the elastic modulus during the first cycle is significantly lower than that one observed when a/R was ≈ 0.09, which was closer to 60 GPa.

Most importantly, with subsequent loading, reversible hysteresis (see Fig 4-15a) was observed as in the case of loading normal to the basal planes. However, given the nucleation of the twins and the absence of a LAKB, it is reasonable to assume that the mechanism of energy dissipation is related to *either* the reversible movement of the twin boundaries, dislocation-twin interactions, or both. The first conjecture is consistent with a previous study by Mann et al. [48], in which {10$\bar{1}$2} twins in Mg and Mg-Zn alloys were concluded as being partially reversible upon unloading resulting in reversible plastic strain. In their study, snapshots of $\{10\bar{1}2\}$ twins during loading and unloading showed a decrease in the twin width when a sample was unloaded, lending credence that twin boundaries can indeed move reversibly. In this present study, there are several observations that are consistent with the first conjecture. First, the fact that the indentation mark is not circular but oval and thus by necessity when the indenter is pushed into the surface, the narrow axis of the oval must move out of the way first. The principle of how this can be accomplished is shown schematically in Fig. 4-16. Under cyclic loading and unloading, the twins are assumed to widen and contract fully, spontaneously and reversibly.

The second conjecture – that dislocation twin interactions is the mechanism for energy dissipation – can be understood by the fact that <a> basal and prismatic dislocations in materials such as Co, Re, Zr, Ti, Hf and Mg interact repulsively with $\{101\bar{2}\}$ twin boundaries [14]. Since these dislocations do not contribute to the growth of twins in these materials, it is reasonable to assume that dislocation pile ups occur at the twin-matrix interface may contribute partially to the energy dissipation in the form of back stress on the dislocation source. In spite of these comments, more work is needed to better understand the origin of W_d in this orientation.

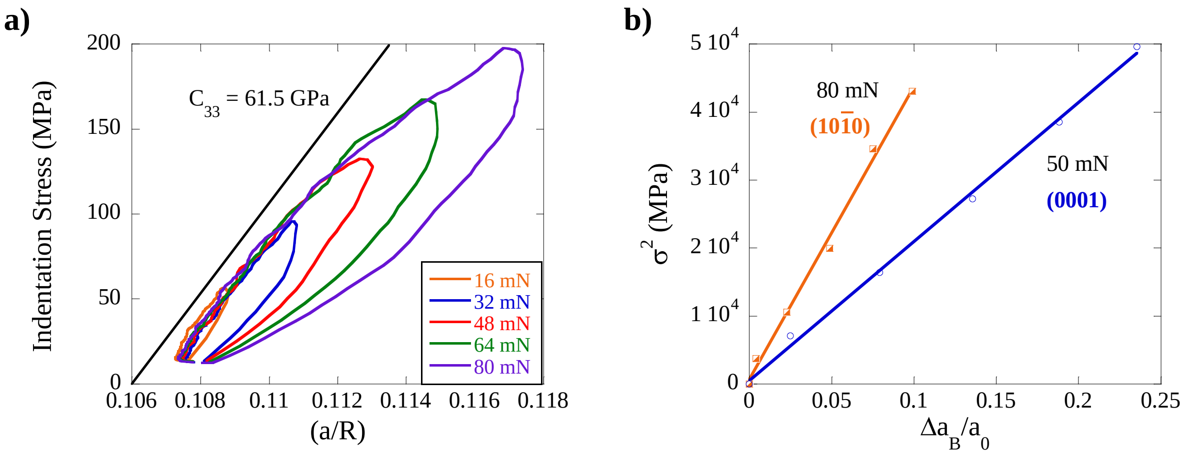

Figure 4-15. a) Indentation stress vs. a/R plot of nested cycles loaded to a maximum load 80 mN for 50 cycles. b) $\Delta a_B/a_o$ plotted against σ^2 for the same indent loaded to 80 mN for 50 cycles, and compared with a similar plot from (0001) plane indentation loaded to 50 mN for 50 cycles.

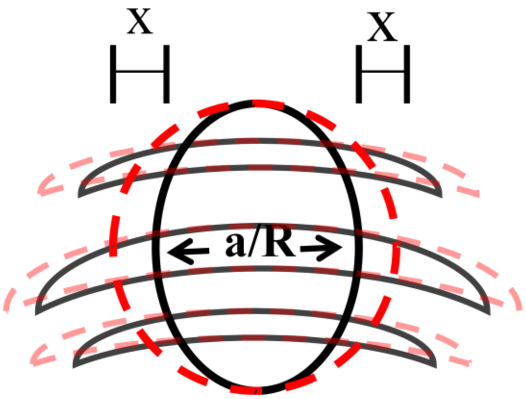

Figure 4-16. Schematic of indentation on the $(10\bar{1}0)$ plane in Mg single crystal. Under an applied load, the width of the short axis of the indent must move outward (red dotted lines) by some distance, x, to accommodate the indenter penetrating into the surface. As the short axis expands, the twins widen (faded red lines). When the load is removed, the twins and short axis contract to the minimal dimensions (black outlines).

Turning attention back to the nested cycles (Fig. 4-15a), $\Delta a_B/a_o$ was calculated and plotted against σ^2 (see Fig. 4-15b) for a location (D2) loaded to 80 mN on the $(10\bar{1}0)$ plane for 50 cycles and compared with a location loaded to 50 mN for 50 cycles on the (0001) plane. The value for R^2 for the 80 mN location was > 0.99, indicating a good fit to a line. The hardening rate within the cycles in Fig. 4-15a was ~ 13.6 GPa, which was much higher than the strain hardening observed during the first cycle (see Fig. 4-14), which was ~ 600 MPa. This observation is again indicative that the physics is different within the two regimes, as was postulated with nanoindentation on the (0001) plane. Table 4-5 shows the hardening rates for the various locations used in this study, which were typically higher than the hardening rates from indentation on the (0001) plane.

Table 4-5. The yield stress, σ_y, and hardening rates for the incremental cycles indented on the prismatic planes.

Series	Load (mN)	Cycles	Location	σ_y (MPa)	Hard. Rate (GPa)
D	80	50	1	45	16.8
D	80	50	2	50	13.6
D	80	5	3	39	7.9
E	100	50	1	45	12.0
E	100	50	2	45	16.1
E	100	50	3	37	14.1

4.5.2 TEM observations beneath $(10\bar{1}0)$ indents

Cross sections of indents to 80 mN for 50 cycles were lifted out and analyzed using TEM. Figure 4-17a is a TEM micrograph of one such indent, which essentially shows the cross section of a twinned region beneath the indent. This cross section was lifted out along the length of the indent so that the twins were perpendicular to the lift out. Various grains of different orientations were observed to have formed with no apparent LAKB at the edge of the indent. Diffraction patterns (Figure 4-17b) showed some of the variation between the different grains. Since the indent was lifted out along the length, some <*c* + *a*> dislocations appeared in contrast and were observed within a select region (not shown in data).

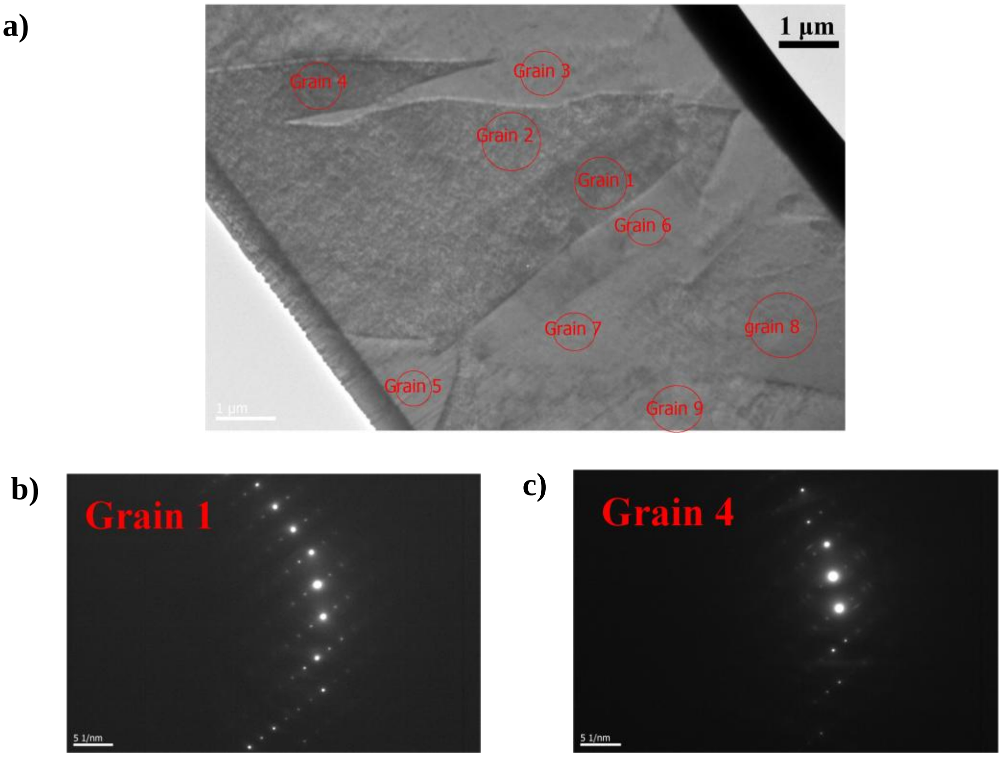

Figure 4-17. a) TEM micrograph of an indent cross section loaded to 80 mN for 50 cycles on the (10$\bar{1}$0) plane in Mg single crystal. The twinned region consists of various grains as shown in figure. b-c) Diffraction patterns taken from two grains, of more than 5 grains identified in one region, shows some variation in the orientations between different grains.

A cross section was also lifted off along the width of the indent (parallel to the twins) to investigate the features within the twins. Figure 4-18a shows the extent of a twin to a depth ~ 6-7 µm, while Fig. 4-18b shows the bottom edge of the twin. Dislocations observed beneath the twin boundary in this lift out appeared to be mostly <a> basal and prismatic dislocations based on the TEM micrographs. Since the basal planes were normal to the cross section of the lift out, dislocations with an <a> component appeared in contrast in Fig. 4-18a. In comparison to micrographs of lift outs taken perpendicular (not shown) to the twins, more dislocations with <a> component were observed in a similar sized region. These observations help to support the idea that dislocation-twin boundary interactions may contribute to the loops in the indentation stress vs. a/R curves. This idea is certainly consistent with the notion that {10$\bar{1}$2} twin boundaries in

Mg are capable of growing and shrinking, as reported by Mann et al. [48] in a study on Mg and others [16, 61]. More work is needed to fully understand the exact role and to what extent the dislocation-twin interactions contribute to W_d.

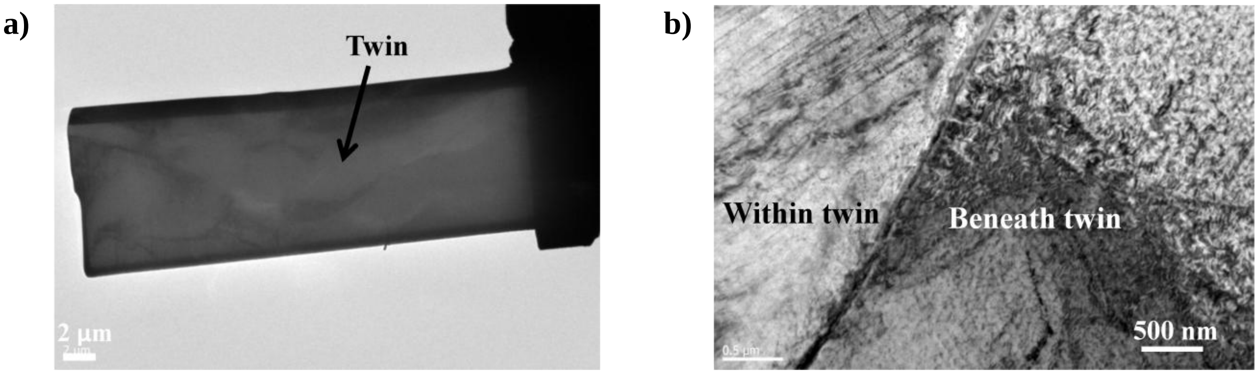

Figure 4-18. a) Cross section of an 80 mN indent lifted out parallel to twins. The twin is shown extending to a depth ~ 6-7 µm beneath the surface of the indent. b) TEM micrograph of a region at the bottom interface twin and matrix.

In summary, when indenting on the $(10\bar{1}0)$ plane, tensile twins form beneath and around the indented region, but no LAKBs. These twins are believed to either expand and contract under loading and unloading, and/or interact with <a> basal and prismatic dislocations. It is the to and fro motion of these twins or dislocations that leads to energy dissipation, i.e. W_d. It is unclear from this study whether W_d depends on the twin type and material, or if other types of twins in general will result in similar observations made in this study.

CHAPTER 5: ZINC

5.1 Background on Zinc

Belonging to the space group P6$_3$/mmc, Zn has an hcp crystal structure with lattice parameters a = 2.66 Å and c = 4.94 Å. Zinc has been subjected to various studies to better understand its deformation modes and mechanical behavior. Parison et al. [62] investigated the deformation modes in Zn coatings and bulk Zn under tension at strains beginning at the onset of plasticity to macroscopic strains ~ 4%. Basal slip was observed as being the predominant deformation mode in this study, while non-basal slip can be activated by loading a crystal either perpendicular or parallel to the basal planes since the shear stress on the basal planes is zero. In a study by Gilman [20], slip was observed as occurring on the $\{10\bar{1}0\}$ plane in the $<11\bar{2}0>$ directions when Zn was loaded in tension parallel to the basal planes between 250 – 400° C. Slip in zinc crystals has been observed on the second order pyramidal $\{1\bar{1}22\}$ planes in the $<\bar{1}\bar{1}23>$ directions in a study by Bell and Cahn [63, 64] at room temperature as well.

The primary twinning modes in Zn are $\{11\bar{2}1\}$, $\{11\bar{2}2\}$, $\{10\bar{1}1\}$ and $\{10\bar{1}2\}$; however, since Zn exhibits limited ductility, it only twins by the $\{10\bar{1}2\}$ twin [14]. Since zinc has a c/a ratio of 1.854, which is greater than the ideal ratio, 1.633, the $\{10\bar{1}2\}$ twin is a c-axis compressive twin. Yoo et al. [65] used nanoindentation on zinc single crystal loaded perpendicular to the basal planes to induce twinning, which again is a result of the large c/a ratio for Zn since a sufficient compressive stress will induce twinning when loaded perpendicular to the basal planes [65, 66].

In addition to slip and twinning as deformation modes, Zn has also been known to deform by kink band formation. As noted above, Orowan [9] was a pioneer in theory of kinking when he theorized a new type of plastic deformation in metals when he observed kinks when Zn and Cd wires that were compressed parallel to their basal planes. Gilman [8] observed kink bands within rods of Zn single crystals when compressed parallel to the basal planes (i.e. edge on) and at angles greater than 2.5° from the orientation axis. In a study by Rosenbaum [64], kinks were observed when Zn single crystals were compressed normal to the basal planes under indentation and four point bending tests. This same study also revealed the activation of basal and non-basal dislocations with non-basal dislocations being diffuse when loading normal to the basal planes. When loading was applied parallel to the basal planes, Rosenbaum [64] reported that non-basal slip was activated, but no kinks were formed. The difference between the studies by Gilman [8] and Rosenbaum [64] was that the loading conditions in Gilman's study compressed the entire sample, leaving free surfaces to accommodate a kink to form, whereas in the latter study by Rosenbaum, loading was applied parallel to the basal planes and locally confined to within the matrix, which quite possibly inhibited kinking.

Like other hexagonal materials, Zn has been known to exhibit exceptional mechanical properties, such as reversible hysteresis loops [56] in the stress-strain curves during cyclic loading. Studies [19, 25, 26, 48, 67, 68] have investigated this very unique phenomenon on various hexagonal materials. The large plastic anisotropy in the hcp crystal structure is believed to be related to this unique mechanical response. The fact that Zn can deform by kink band formation and is also capable of exhibiting reversible non-linear strain suggests that Zn is a KNE solid (see Ch. 2).

In addition to Zn, ZnO is also a KNE solid [13]. In a study on ZnO by Basu et al. [19], cyclic nanoindentation was performed on ZnO single crystals on the A and C-planes using a 13 or 1 μm spherical tip. Hysteresis loops were observed when indenting on the C-plane, but no loops were observed when indenting on the A-plane. The C-plane was found to be twice as hard as the A-plane as determined from Vicker's indentations, which was attributed to the orientation of the basal planes relative to the indentation direction. The hardness was also a function of tip size on the C-plane. Pyramidal slip bands were observed in SEM images, and pyramidal dislocations nucleated under C-plane indentation in addition to basal dislocations, which were also as observed by Bradby et al. [69], were believed to account for the higher hardening rate. The hysteresis loops observed in this study was attributed to incipient kink bands (IKBs) (see Ch. 2) in the form of to-and-fro motion of basal dislocations.

In a study by Roberts and Brown [56], Zn single crystals were grown using the Bridgman method from highly pure cast Zn, and the microstrain in the Zn single crystals was studied in tension using an Instron testing machine with a strain sensitivity of 10^{-6}. Both micro and macro stress-strain curves were studied and non-linear behavior was observed at nearly zero stress – well below the macroscopic yield stress. The macroyielding process was believed to be a unique process – noting the sharp transition from micro to macrostrain. Closed hysteresis loops were observed below the macroscopic yield point, which was noted to fit the prediction that Granato and Lucke [70] made on the presence of hysteresis loops and being strain amplitude dependent. Roberts and Brown [56] observed closed hysteresis loops at strains 5×10^{-5} and found the loops to be strain dependent, and samples required some permanent strain before closed hysteresis loops were observed. It was concluded that the reversible strain associated with the closed hysteresis loops were due to bowing of dislocation networks, where the nonlinear strain was the result of unbowing of dislocations in the network. When the results of Roberts and Brown are plotted, plots similar to those shown in Fig. 4-12 are recovered indicating that the plots shown in Fig. 4-12 are valid for more than one hexagonal metal.

Few nanoindentation studies on pure Zn have been reported in literature, with a recent study [71] in 2014 investigating the anisotropy of hcp metals Mg, Zn and Ti. This study used a spherical-conical indenter tip with 1 μm radius on select grains of each material, and reported that the hardness values for Zn varied by a factor of 2 with respect to the orientation of plane of indentation, and the hardness values for Mg varied by orientation by a factor ~3.6. Limited details and results were provided from this study, which leaves opportunities to investigate the response of Zn to nanoindentation.

5.2 Experimental details for zinc

A polycrystalline zinc (99.9% basis, Rotometals, San Leandro, CA) ingot with grain sizes ranging from approximately 200 to > 700 μm was cut into a small cubes (~ 5 mm x 5 mm x 5 mm), hot mounted in resin and ground down using 800 – 1200 SiC grit paper. The small cubes were mechanically polished down to ¼ μm diameter sized particles using a water based diamond suspension. Since Zn can oxidize rapidly in an aqueous environment, an alcohol based suspension (DP-Suspension A, Struers, Westlake, OH) with 0.25 μm diameter sized diamond particles was used for the final polishing step. To minimize oxidation, the polished sample was stored under vacuum until ready for use in the nanoindenter, FIB or SEM. EBSD was used to generate OIM map of the different grains on which the nanoindentation tests would be performed. Figure 5-1 shows the EBSD patterns of the four grains used in this study.

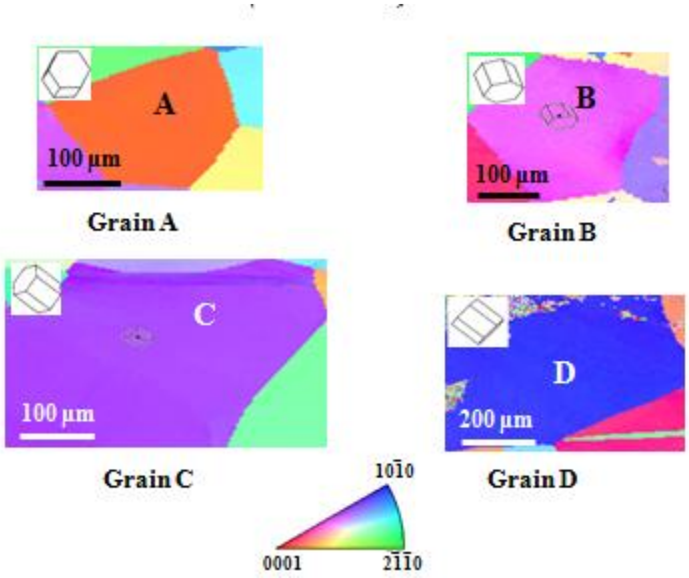

Figure 5-1. EBSD was used to generate an orientation map of the grains shown here. The inverse pole figure map is also shown here. Each pattern was cleaned up with a minimum grain size 10 µm and a tolerance 5 degrees.

The nanoindentation tests were performed in continuous stiffness mode (CSM) on select grains using a 100 µm radius tip for each location at a strain rate 0.1 s^{-1}. Since the grain sizes were significantly larger than the size of the indent, nanoindentation within a single grain was equivalent to indenting a quasi-single crystal. Each test involved loading to a maximum or peak load (50 mN or 150 mN) and unloading to a minimum load (5 mN) 50 times, followed by a series of five nested cycles consisting of 20 – 100% of the peak load. Some tests were loaded to a maximum of 50 mN to investigate whether or not the applied stress had any significant effect on the reversible hysteresis effect, while all other tests used a peak load of 150 mN. All tests on zinc were performed using 50 cycles. Table 5-1 details a summary of nanoindentation tests used in the study on zinc.

Table 5-1. Various grains were identified using EBSD and the grain orientations along with the peak applied loads. Each location was cyclically loaded 50 times to a peak load, followed by an incremental cycle sequence consisting of 20 – 100% of the peak load.

Grain	Orientation	Location	Load (mN)
A	**(0001)**	1	50
		2	
		3	150
		4	
		5	
		6	
B	**$(10\bar{1}2)$**	1	50
		2	
		3	
		4	150
		5	
		6	
C	**$(10\bar{1}1)$**	1	150
		2	
		3	
		4	
		5	
		6	
D	**$(10\bar{1}0)$**	1	150
		2	
		3	
		4	

The contact radii of all locations in series A-D were measured in a dual beam FIB-SEM. For the most part, the indentation marks were found to be quite circular (Fig. 5-2). Instrumental drift was corrected (see Ch. 3) as needed. In an attempt to better understand what was occurring microstructurally below the indenter, cross sections of indents in the various orientations were lifted out using a FIB and examined using a TEM. However, the TEM sample preparation in the FIB became the ultimate challenge for reasons that are unknown in their totality. It is possible that residual stresses may have been present in the samples, which made thinning lamellae to <

100 nm impossible due to bending and twisting during sample preparation. Thus limited amount microstructure information could be obtained in this study.

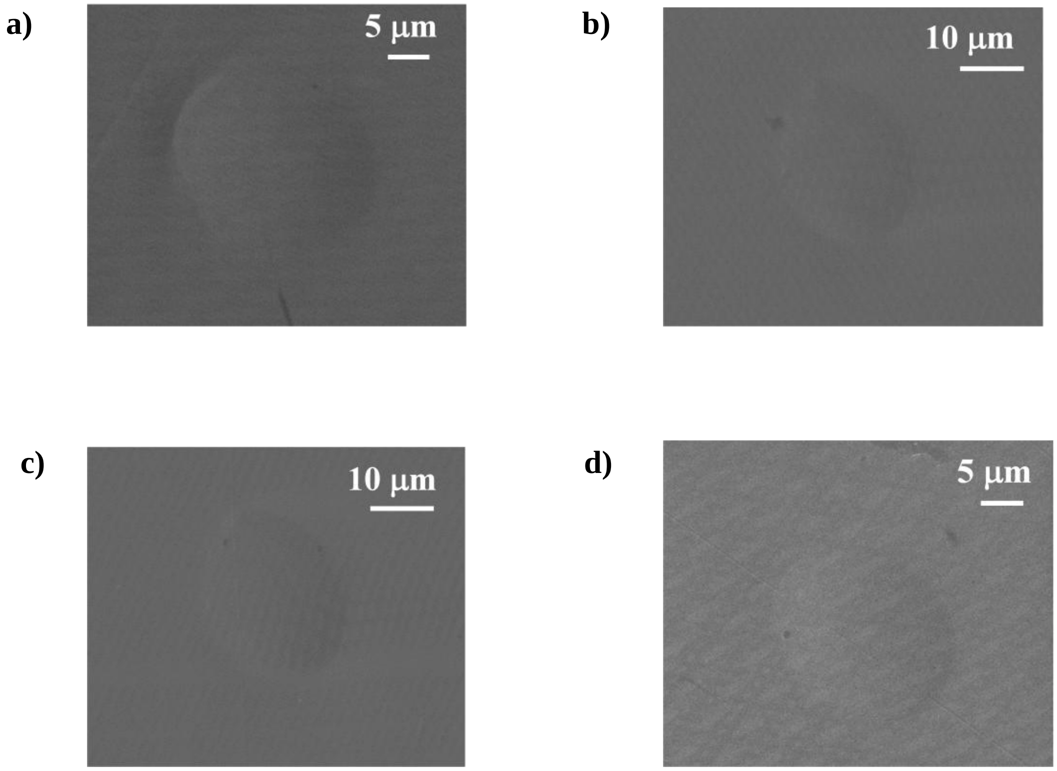

Figure 5-2. SEM images of typical indent craters after spherical nanoidentation on was applied normal to the a) (0001), b) $(10\bar{1}2)$, c) $(10\bar{1}1)$ and d) $(10\bar{1}0)$ planes.

5.3 Results and observations on Zn

5.3.1 Nanoindentation results

Typical load vs. displacement curves from select indents loaded on the (0001), $(10\bar{1}2)$, $(10\bar{1}1)$ and $(10\bar{1}0)$ planes for 50 cycles are shown in Figs. 5-3a to d, respectively. Figure 5-4 shows the load vs. displacement curve for the 50^{th} cycle for each of the four locations loaded to 150 mN in Fig. 5-3. It is important to note that the loading and unloading curves for the 50^{th} cycle of the load vs. displacement curves for indentations made on the $(10\bar{1}0)$ plane are essentially two parallel lines separated by a small distance (< 3 nm); a value that is within error of machine measurements. This is in contrast to the other orientations, where the 50th cycle clearly outlines a loop during which energy is dissipated.

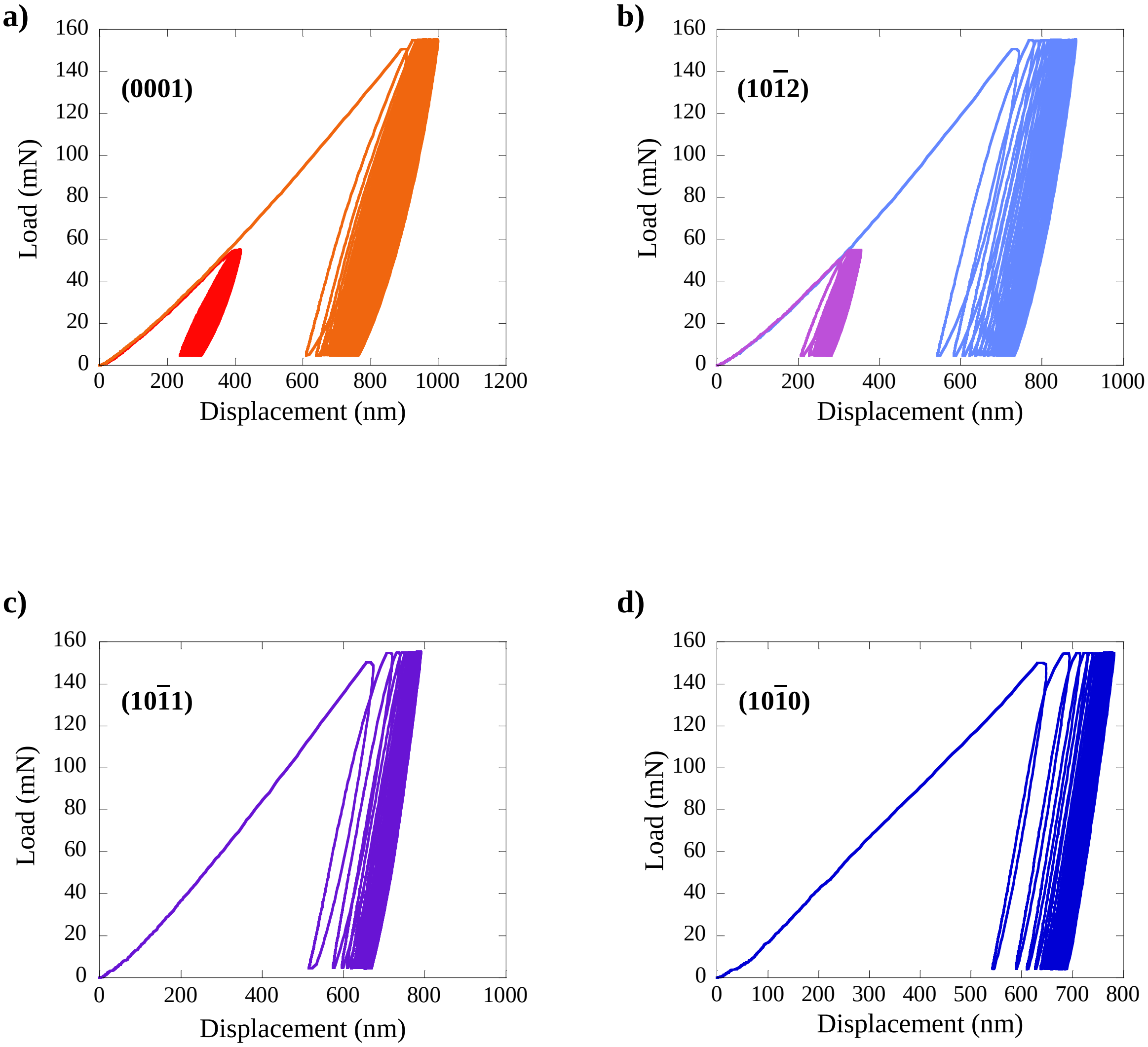

Figure 5-3. Load vs. displacement curves at select locations from nanoindentation on the a) (0001), b) $(10\bar{1}2)$, c) $(10\bar{1}1)$ and d) $(10\bar{1}0)$ planes are shown. Each location was loaded 50 times.

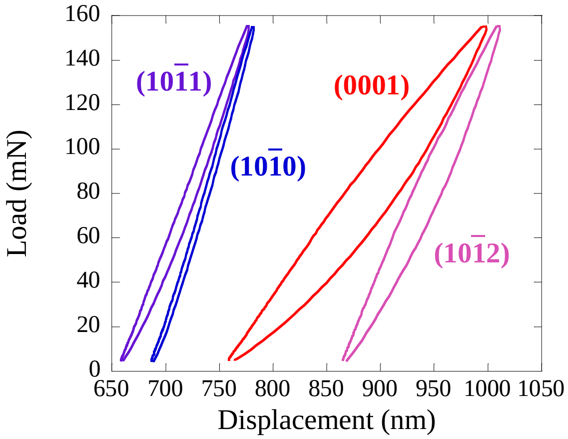

Figure 5-4. Load-displacement curves of the 50th cycle as a function of the different orientations. The width of the hold segment and the width between the start and end of the 50th cycle for (10$\bar{1}$0) orientation are very similar, if not, identical. The loading and unloading curves are essentially parallel lines separated by a small distance that may have been due to drift or creep.

Representative indentation stress vs. a/R curves for each orientation are shown in Fig. 5-5. In general, there was good agreement between the elastic moduli expected from Hertzian analysis and the elastic moduli measured during the first cycles, with the exception being nanoindentation on the (0001) plane. The elastic modulus measured during the first (initial) loading cycle on the (0001) planes was compared to the expected elastic modulus along the [0001] direction, which is $E = c_{33} = 61.8$ GPa. The measured slope however, was lower as seen in Fig. 5-5a. It is unclear why this discrepancy occurred. On the contrary, in all other orientations, the same discrepancy did not occur. The slope during initial loading on the (10$\bar{1}$2) and (10$\bar{1}$1) planes was fit to the elastic modulus expected on the (10$\bar{1}$2) and (10$\bar{1}$1) planes in which the c-axis was assumed to be ~50° and ~70° relative to the loading directions respectively. The expected elastic moduli for each case was calculated using Eq. 2-9 to be 53.6 GPa and 45 GPa on the (10$\bar{1}$2) and (10$\bar{1}$1), respectively. The elastic constants for Zn used in this calculation were $C_{11} = 165$ GPa, $C_{33} = 61.8$ GPa, $C_{13} = 50$ GPa and $C_{44} = 39.6$ GPa, which were taken from Smithell's metal reference book [60]. Lastly, loading applied on the (10$\bar{1}$0) plane fit well with the expected elastic modulus in the $[10\bar{1}0]$ direction, which was E = 62.6 GPa using Eq. 2-9. It is worth while pointing out that when the slope of the elastic moduli (red lines in Fig. 5-5a-d) along a specific direction was compared with with the NI stress vs. a/R curve after cycling, the stiffness was much higher. It is unclear why the stiffness increased by so much after cycling. The reproducibility of the NI stress vs. a/R plots for the surfaces loaded to 50 mN and 150 mN in Figs. 5-5a and b is noteworthy.

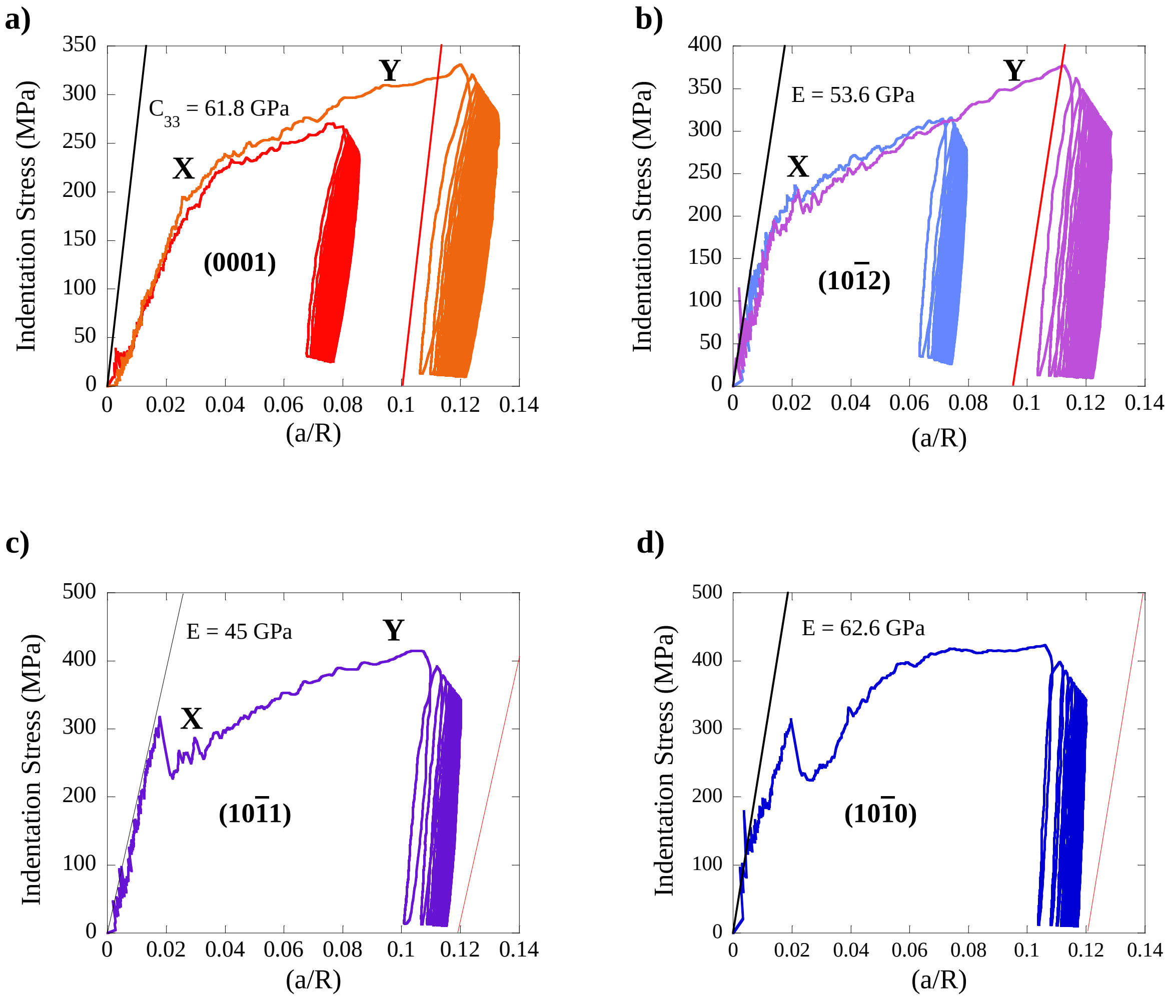

Figure 5-5. Indentation stress vs. a/R curves on the, a) (0001), b) $(10\bar{1}2)$, c) $(10\bar{1}1)$ and, d) $(10\bar{1}0)$ planes of the various orientations. The modulus during the first cycle was a reasonable fit to the expected elastic modulus from Hertzian analysis in most cases. The (0001) orientation didn't fit as well as the other locations for reasons that are unknown. The red lines in each plot correspond to the elastic moduli in each respective orientation. The slope of the curves after cycling is much greater than the elastic moduli indicating higher stiffness after cycling.

Note that pop-ins occurred at some locations (Fig. 5-5c-d), as evidenced by the sudden drop in stress in the indentation stress vs. a/R curves during initial loading, followed by work hardening. Pop-ins were observed in similar nanoindentation studies on ZnO [19] and Mg [45], and result from homogenuous dislocation nucleation in a defect free [72] or a low dislocation density region in a small volume, i.e., dislocation starvation. From these, and other results, it is clear that: i) For most locations, the initial response was linear elastic with some deviation from Hertzian analysis in the (0001) orientation; ii) Pop-in events occurred at stresses ~ 300 MPa on the $(10\bar{1}1)$ and $(10\bar{1}0)$ planes; iii) Past the pop-ins, the stresses dropped to approximately 225 MPa and then slowly increased with further displacements into the surface. In this region, the hardening rate was on the order of 1 – 2 GPa, depending on orientation.

Note that the values for a/R for locations loaded to 150 mN throughout all series ranged between 11-13%. When loaded to only 50 mN in series A and B, however, a/R was typically around 7% with one exception at 6.5%. It follows as expected, and as observed in the case for Mg, a/R was dependent on the maximum loads.

The results presented herein are consistent with similar observations made by Roberts et al. [56], in which closed hysteresis loops were observed on Zn single crystals that were loaded below the macroscopic yield point after some permanent deformation. Figure 5-6 shows typical indentation stress vs. a/R curves for one nested sequence from each orientation loaded to 150 mN for 50 cycles (see Table 5-1). These curves, as with all other locations in each series, are characterized by a linear elastic region, whose slopes were significantly larger (131.5 GPa on the (0001) plane, 217.8 GPa on the $(10\bar{1}2)$ plane, and 244 GPa on the $(10\bar{1}1)$ plane) than those predicted from Hertzian analysis (see Fig. 5-6a). The expected slope (Fig. 5-6a) in the elastic region for indentation on the (0001) plane should be 61.8 GPa, while the slopes for the $(10\bar{1}2)$,

$(10\bar{1}1)$ and $(10\bar{1}0)$ orientations should be 53.6 GPa, 45 GPa and 62.6 GPa, respectively (shown in Fig. 5-6 as dashed lines), which corresponds to the elastic modulii calculated using Eq. 2-9. It remains unclear why the measured slopes were much higher than the theoretical expectations. One possible explanation is elastic kickback as the dislocations run back upon unloading. This comment notwithstanding, more work is needed to fully understand this fascinating discrepancy. In passing, a similar phenomenon was also observed when ZnO [19] single crystals were loaded parallel to the basal planes and in a nanoindentation study [73] on rutile (TiO_2) with loading applied on the (001) plane. One final note to make is that Roberts et al. [56] made observations of closed hysteresis loops at strains on the order of $2x10^{-5}$, which is at least three orders of magnitude smaller than the observations made in this study. In their study, it was pointed out that reversible hysteresis was strain amplitude dependent.

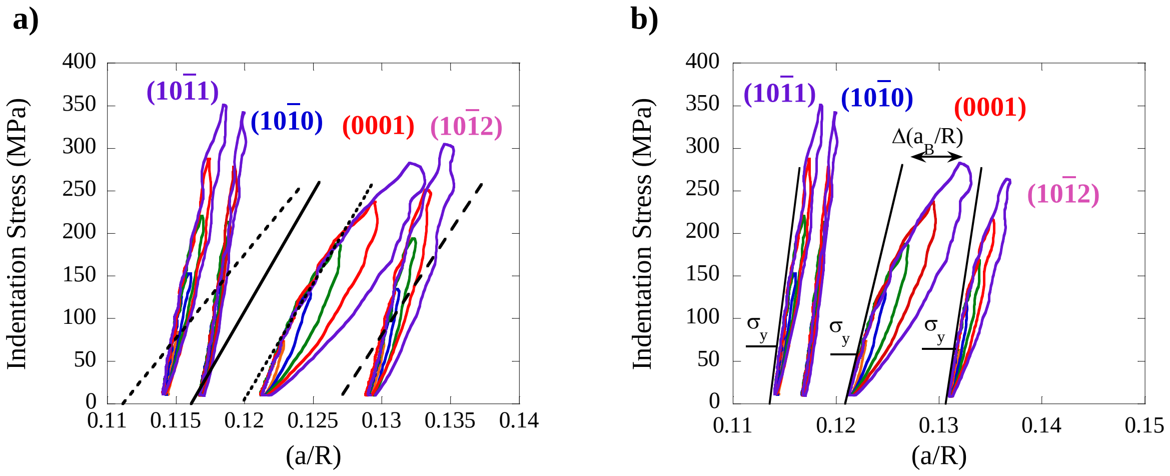

Figure 5-6. Nested cycles from the different orientations are plotted. Loops were observed in the (0001), $(10\bar{1}2)$ and $(10\bar{1}1)$ orientations, but not in the $(10\bar{1}0)$ orientation. The $(10\bar{1}2)$ data set was shifted to the right by 0.0075 for clarity. a) The lines next to each series are the calculated theoretical slopes of the elastic moduli for each specific orientation, which correspond to 61.8 GPa for the (0001) plane, 53.6 GPa for the $(10\bar{1}2)$ plane, 45 GPa for the $(10\bar{1}0)$ plane and 62.6 GPa for the $(10\bar{1}0)$ plane. b) The yield stress, σ_y, was determined by fitting a straight line to the measured linear elastic region and determining where the curve transitions from linear to non-linear. $\Delta(a_B/R)$ is the total a/R value minus the a/R in the linear elastic region within a nested cycle.

Since there was a deviation from the theoretical elastic moduli expected, a line was fitted to the slope in the elastic region for each nested sequence, and the (microscopic) yield stress, σ_y, was taken as the point at which the curve changes slope. At a given yield stress, σ_y, the change in slope corresponds to the emergence of the fully, and spontaneously, reversible loops in the indentation stress vs. a/R curves. When the load was removed, the curves returned to their point of initial loading, completing the loop as shown in Fig. 5-6.

The yield stresses were weakly dependent on the applied load in the (0001) and $(10\bar{1}2)$ orientations, but varied slightly on orientation. Indenting on planes closer to normal to the basal planes resulted in slightly lower values for $\sigma_{y,}$ while indenting on planes that were closer to parallel to the basal planes resulted in slightly increased values for $\sigma_{y.}$

In addition to determining the yield stresses, the hardening rates, HRs, for the nested loops were also calculated for each location (see Table 5-2). Surprisingly, the hardening rates did not show a strong variation as a function of applied load. However, the hardening rates showed significant variation as a function of orientation. The strain HR for the nested loops was typically ~ 20 GPa for indentations on the (0001) plane, ~ 40 GPa for indentations on the $(10\bar{1}2)$ plane and ~ 75 GPa for indentations on the $(10\bar{1}1)$ plane. Interestingly, the HRs due to classic work hardening ranged between ~ 1 GPa to 2.3 GPa with the highest values observed in the $(10\bar{1}1)$ orientation and the lowest (965 MPa) in the (0001) orientation. The classical work HR is simply the rate of strain hardening that results from an increased dislocation density as the material is plastically deformed beyond its yield point. Values for the HRs were calculated by measuring the slope from X to Y in Fig. 5-5.

Table 5-2. Nanoindentation contact radius, a_{NI}, contact radius measured in the SEM, a_{SEM}, the total change in contact radius, Δa_{tot}, the yield stress, σ_y, and hardening rates are shown. The hardening rates were calculated from indentation stress vs. a/R plots.

	Load	**Cycles**	**Loc**	**a_{NI} (μm)**	**a_{SEM} (μm)**	**Δa_{tot} (μm)**	**σ_y (MPa)**	**Hardening Rate (GPa)**
0001	50	50	1	7.6	7.3 ± 0.1	0.86	51.7	19.2
	50	50	2	7.6	7.0 ± 0.1	0.82	52.8	22.3
	150	50	1	12.1	11.6 ± 0.5	1.06	59.4	20.8
	150	50	2	12.3	11.7 ± 0.5	1.14	60.4	23.4
	150	50	3	12.3	11.9 ± 0.2	1.10	55.4	20.3
	150	50	4	12.5	11.72 ± 0.3	1.08	58.4	19.2
$10\bar{1}2$	50	50	1	7.4	6.5 ± 0.1	0.50	64.4	43.7
	50	50	2	7.7	6.9 ± 0.2	0.46	64.4	40.4
	50	50	3	8.0	7.1 ± 0.2	0.44	60.0	45.0
	150	50	1	12.8	12.2 ± 1.2	0.55	64.4	44.5
	150	50	2	12.9	12.4 ± 1.0	0.54	58.3	45.4
	150	50	3	13.1	12.7 ± 1.4	0.56	61.4	39.0
$10\bar{1}1$	150	50	1	12.0	11.3 ± 0.7	0.41	70	79.7
	150	50	2	13.0	11.9 ± 0.5	0.42	66	72.4
	150	50	3	12.4	11.3 ± 0.7	0.44	67	75.2
	150	50	4	11.8	11.1 ± 0.8	0.42	67	75.2
	150	50	5	11.8	*9.74 ± 0.2	0.40	66	71.4
	150	50	6	11.4	11.5 ± 0.4	0.43	66	77.4

*Radius measurement at location 5 in ($10\bar{1}1$) orientation may have been a bad measurement in the SEM; however, since drift was minimal, the true contact radius was taken to be a_{NI} = 11.4 μm at this location.

Focusing on the nested cycles (Fig. 5-6) once again, $\Delta(a_B/R)$ was calculated as the difference between the total a/R and the a/R in the linear elastic region of a given cycle, and represents the non-linear reversible region in the indentation stress vs. a/R curve. As with Mg, $\Delta a_B/a_o$ was calculated and plotted against σ^2 (see Fig. 5-7a) and W_d (see Fig. 5-7b) for one location of each orientation in Table 5.2 loaded to 150 mN for 50 cycles. The values for R^2 ranged from > 0.94 to > 0.99, which was a reasonable fit to a line in each plot.

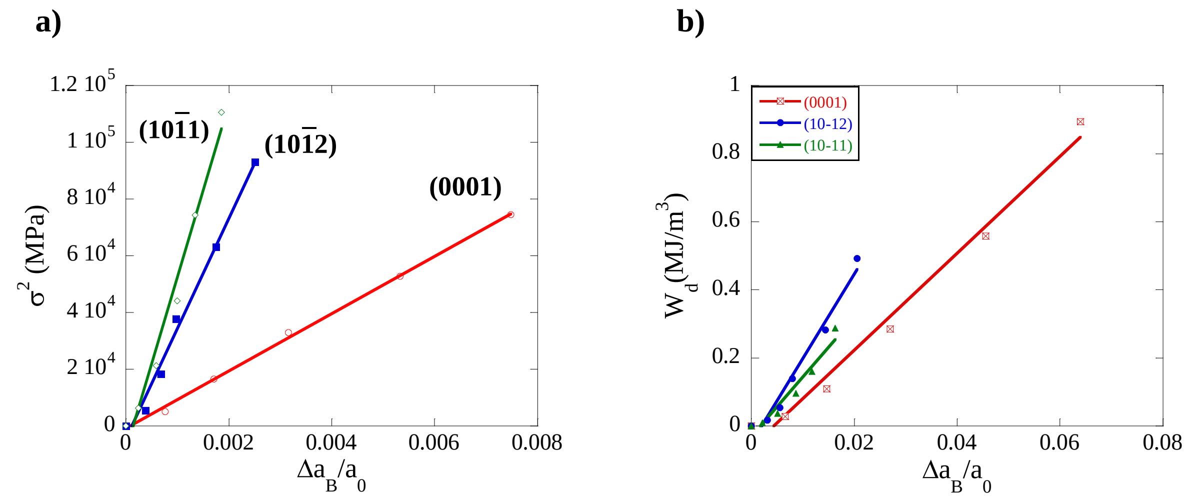

Figure 5-7. $\Delta a_B/a_o$ is plotted against, a) σ^2 and, b) W_d. The values for R^2 in plot (a) were > 0.977 to > 0.99, while those in plot (b) ranged between > 0.94 and > 0.98.

5.3.2 TEM Observations

Indent cross sections were lifted out using a FIB from locations on the (0001), $(10\bar{1}2)$ and $(10\bar{1}0)$ planes (see Fig. 5-8a-b (insets)). However, the TEM results were either not good or scarce due to the difficulty in preparing samples thin enough for proper TEM analysis (< 100 nm) possibly due to high residual stresses in the lift outs that caused them to twist. Figure 5-9 illustrates the difficulty in sample prep. In spite of the limited TEM analysis, some useful observations were nonetheless made. Whenever loading was applied on the (0001), $(10\bar{1}2)$ or $(10\bar{1}1)$ planes (series A-C), a kink formed (see Fig. 5-8a and 5-8b) as a result of indentation with a faint, but sometimes discernible kink boundary near the edge of the spherical indent crater (see Fig. 5-8a).

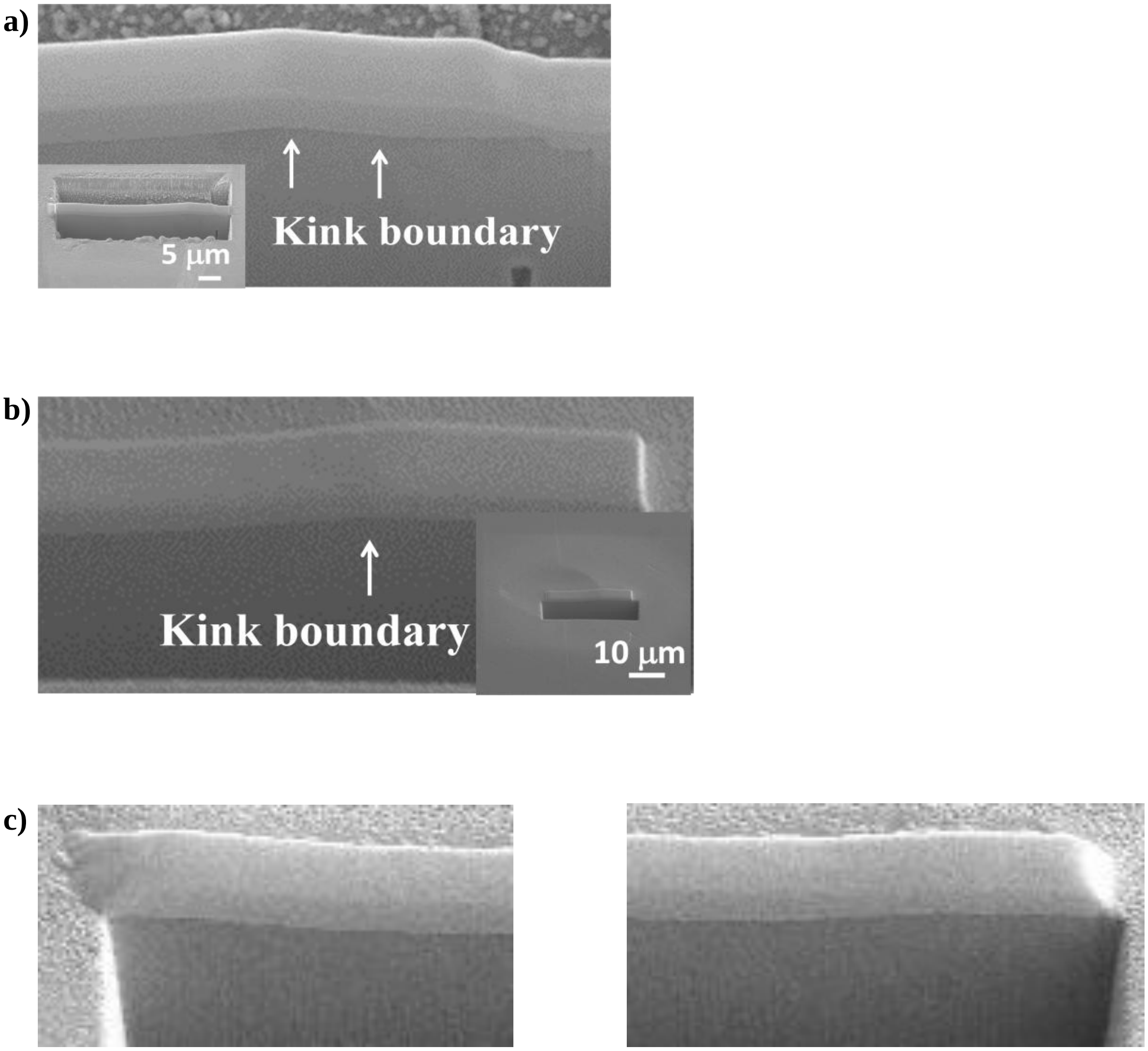

Figure 5-8. SEM images kink boundaries taken from cross section lift outs in the progress at locations on the, a) (0001) plane and, b) (10$\bar{1}$2) planes. c) SEM image taken at both edges of indent made on the (10$\bar{1}$0) plane shows no kink boundary formed. The lower corners of each images (a) and (b) shows the FIB lift out of the indent in progress. The bulk Zn sample oxidized before a lift out on the (10$\bar{1}$1) plane could be attempted.

Figure 5-10 shows a bright field image of a lift out indented on the (0001) plane. It is unclear as to whether or not a true KB was imaged in this micrograph since the sample was heavily damaged in the area where a kink is suspected. This damage was the result of ion milling as bending occurred simultaneously. Figure 5-11 shows diffraction patterns taken at various areas beneath and around an indent made on the (0001) plane. There is the possibility of very slight orientation change beneath the indent in the area near the KB and further away, although it is difficult to make the claim without better data. A diffraction pattern taken between the edge of the lift out and the kink shows a cluster of spots, which may result from orientation changes or possibly from oxidation.

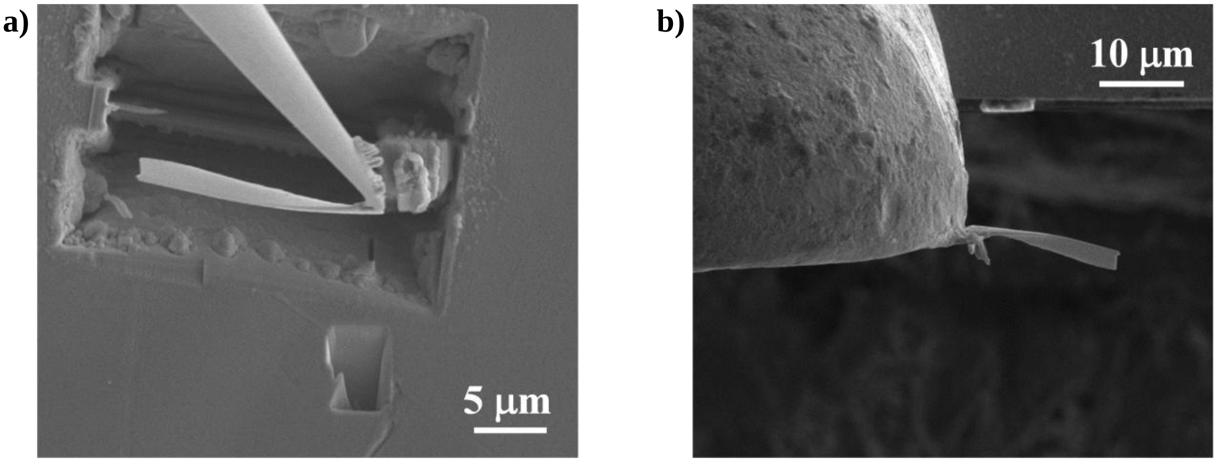

Figure 5-9. SEM images showing attempted lift outs on $(10\bar{1}2)$ orientation for TEM analysis. a) Lift out is shown welded to an omniprobe needle in the FIB, and, b) shows the sample welded to an omniprobe grid. The sample showed heavy bending and twisting during thinning.

No TEM data was collected for indents on the $(10\bar{1}2)$ plane due to the difficulty in sample prep (see Fig. 5-9), and the Zn sample oxidized before a lift out attempt could be made for indents made on the $(10\bar{1}1)$ plane. Some data was collected from indents made on the $(10\bar{1}0)$ plane, however. Figure 5-12 shows bright field images from different areas beneath an indent made on the $(10\bar{1}0)$ plane. There are two possible adjacent grains with slightly different orientations (see Fig. 5-12a) with their diffraction patterns shown in Fig. 5-13a-b. A diffraction pattern taken at the interface is shown in Fig. 5-13c. Figure 5-12b shows features beneath the indent with possible Moiré fringes at some grain boundaries. A diffraction pattern (see Fig. 5-

13d) was taken near the interface of these features and shows some distinction from the previous diffraction patterns.

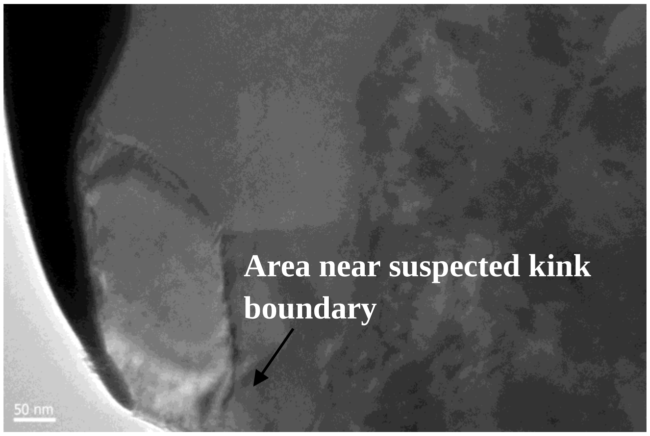

Figure 5-10. Bright field image taken in the area of the kink boundary at the edge of an indent made on the (0001) plane. Since bending caused ion milling to damage the area of interest, it is unclear as to whether or not the kink boundary at the edge of the indent is shown in the image.

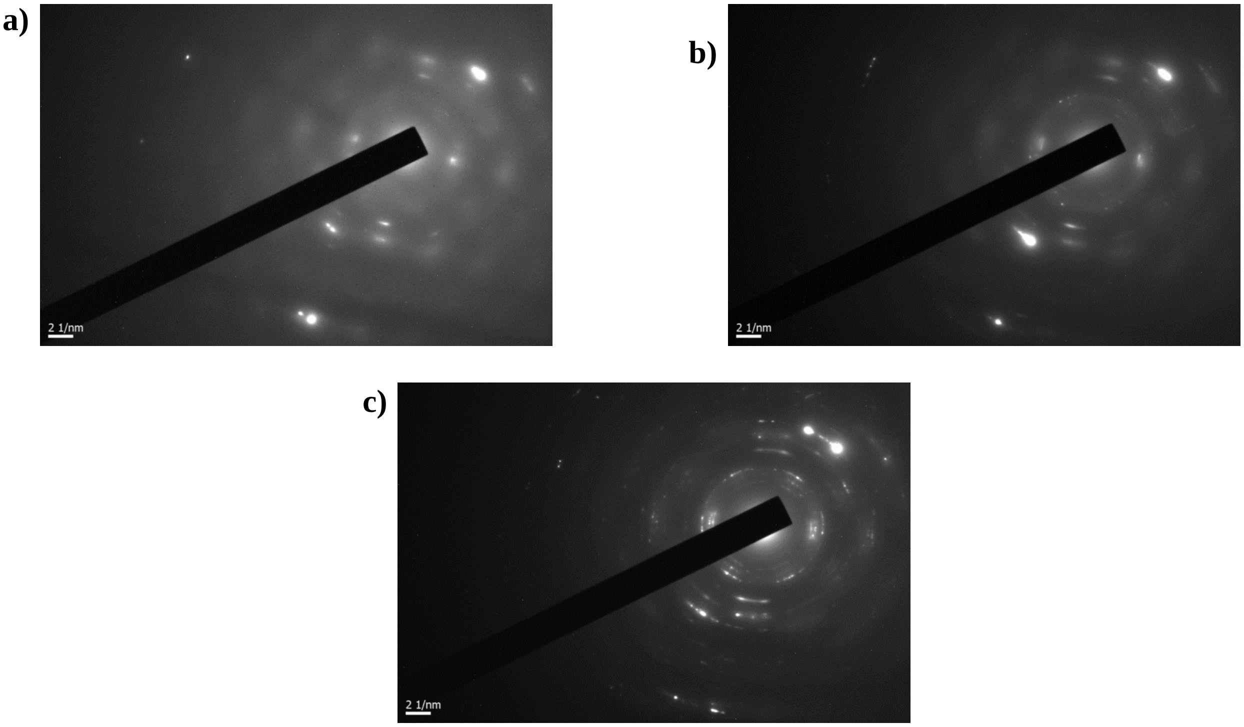

Figure 5-11. Diffraction patterns taken at two locations beneath the indent on the (0001) plane. a) Pattern taken closer to the middle of indent. b) Pattern taken beneath indent, but closer to area around the KB. Both patterns are nearly identical, with the possibility of very slight misorientation between the two. c) Pattern was taken between edge of lift out and area where kink boundary was believed to be, which may indicate orientational changes or oxidation.

The lattice spacing in Fig. 5-13a was calculated to be 2.64 Å, which is close to the *a* lattice parameter for Zn (2.66 Å). This suggests that the lift outs were viewed close to edge on. If dislocations appeared in contrast, then they would have likely possessed a c-component. Unfortunately, due to the difficulty in preparing better samples for TEM analysis (i.e., thinning the samples to less than 100 nm), dislocation studies and analysis was not possible. Kinking was not observed at any indent location made on the $(10\bar{1}0)$ plane. SEM images near the edges of an indent made on the $(10\bar{1}0)$ plane are shown in Fig. 5-8c, which gives no indication of a KB similar to the KBs observed on other orientations. Lastly, no evidence for twinning was observed in any of the lift outs examined in the TEM for any orientation.

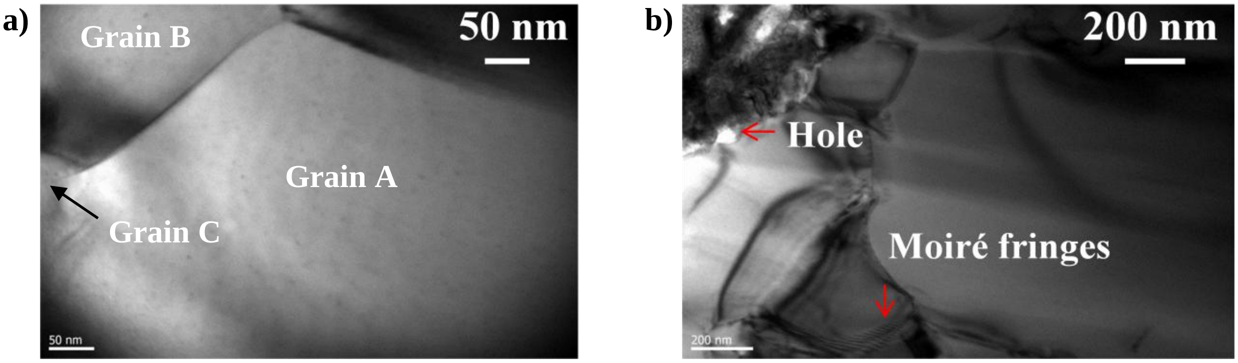

Figure 5-12. Bright field images of different areas beneath an indent made on the $(10\bar{1}0)$ plane. a) Adjacent grains with slightly different orientations and, b) Bright field of features beneath indent such as moiré fringes, holes and possible grain boundaries. The moiré fringes may result from diffraction from grains of different orientations, or a result of the imaging condition.

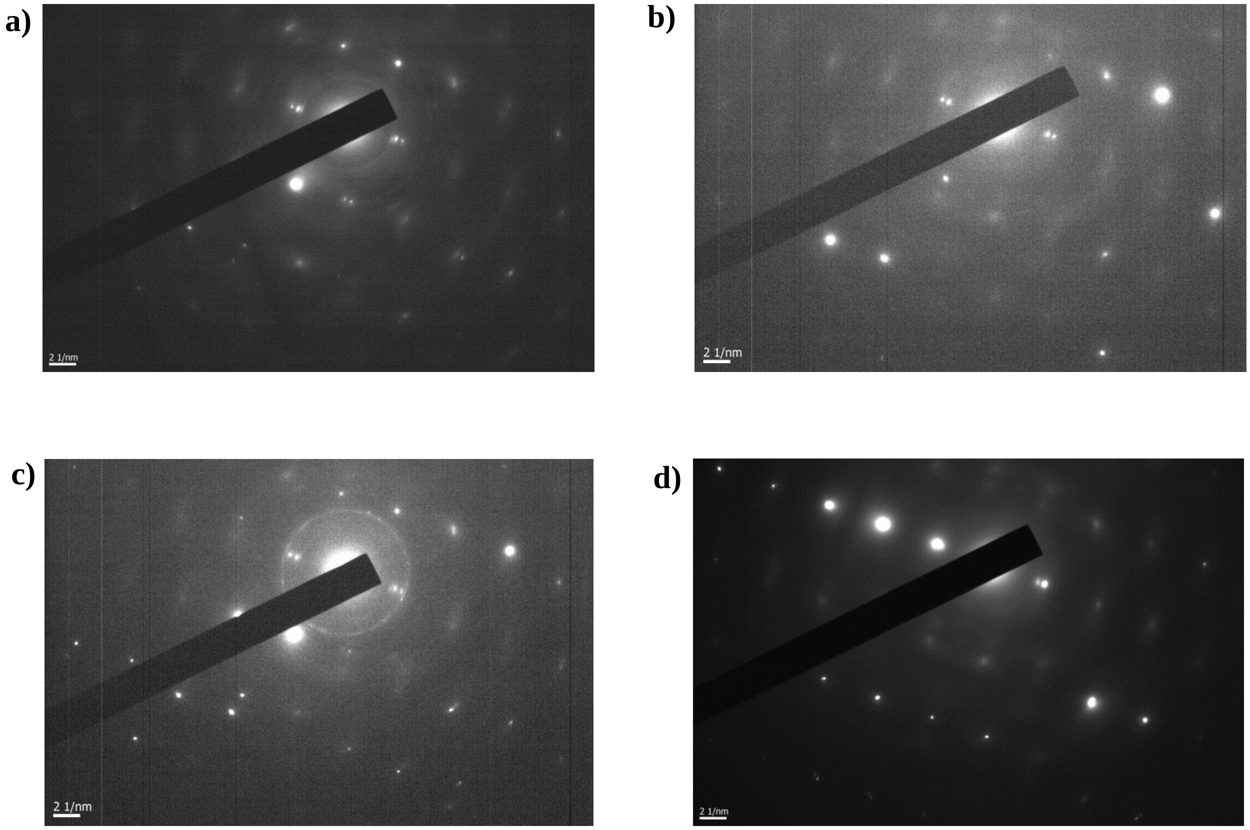

Figure 5-13. a) Diffraction pattern taken within a grain in Fig. 5-12a showing a slightly different orientation than b) the diffraction pattern taken from grain A in Fig. 5-12b. c) Diffraction pattern taken near the interface of grains A and B and the intersection of a possible third grain labeled as C. d) Diffraction pattern taken from a different area beneath the indent, showing a possible slight orientation variation from areas in the previous patterns.

5.4 Discussion

5.4.1 Results on the (0001), $(10\bar{1}2)$ and $(10\bar{1}1)$ planes

The best evidence for LAKBs comes essentially from the SEM images of post indentation marks (Fig. 5.8a and 5-8b) where kinks appeared to have formed on the (0001), $(10\bar{1}2)$ and $(10\bar{1}1)$ planes, especially since the boundaries were either diffuse or evasive. Since twins were not observed, it is reasonable to assume that non-basal slip was activated to accommodate the permanent c-axis strain, as observed in the study by Rosenbaum [64] where indentation and four point bending tests applied normal to the basal planes in Zn single crystal activated diffuse non-basal slip. Assuming non-basal dislocations were activated, then their numbers are likely to be very small compared with basal dislocations, as Catoor et al. [45] showed that more than 90% of dislocations beneath an indentation on the basal planes in Mg single crystal were basal. To accommodate the shape change under the indenter, both geometrically necessary and statistically stored dislocations were nucleated, as mentioned in Ch. 4. The fact that there are LAKBs beneath the indents made on the (0001), $(10\bar{1}2)$ and $(10\bar{1}1)$ planes - in the absence of twins - and loops were present in the NI stress vs. a/R curves for each of these orientation (see Fig. 5.6) suggests that the LAKBs play a vital role in the development of these reversible loops. This conclusion is bolstered by the fact that in the *absence* of KBs on the $(10\bar{1}0)$ plane, no NI stress vs. a/R loops were observed.

In the previous chapter, it was shown that the shear strain, $\gamma_{B,}$ due to dislocations bowing in a network [56] is given by:

$$\gamma_B = \frac{r_{av}}{a_o}\theta \approx \frac{\Delta a_B}{a_o}\theta, \tag{5-1}$$

which is Eq. 4-4. In the case of Zn, since the LAKB angles could not be imaged in the TEM, the angle between the indenter edge and sample surface, was used instead. This angle was calculated assuming $\theta = \tan^{-1}(\frac{h}{a_0})$, where h is the displacement into the surface and a_o is the contact radius measured in the SEM. This calculation for the angle is based on the work of Nix and Gao [74] in deriving an expression for the GND density. The values for θ were calculated to be θ = 3.7±0.14, 3.5±0.6 and 3.4±0.14 for locations loaded to 150 mN for 50 cycles on the (0001), $(10\bar{1}2)$ and $(10\bar{1}1)$ orientations, respectively.

Assuming a Burger's vector, **b** = 2.66 Å, and that the KBs extend to a depth of $2a_o$ into the material in the form of a cylinder, and making use of the angles derived above, the GND density was estimated using Eq. 4-2 to be approximately $4.2\text{x}10^{13}$ m^{-2} for locations loaded to 150 mN for 50 cycles on the (0001) plane, ~4.3x10^{13} m^{-2} for locations loaded to 150 mN for 50 cycles on the $(10\bar{1}2)$ plane and ~ 4x10^{13} m^{-2} for locations loaded to 150 mN for 50 cycles on the $(10\bar{1}1)$ plane. As mentioned previously (Ch. 4), GNDs must form in equal pairs with dislocations beneath the indent and have the opposite sign (see Fig. 4-11a). This enables a crude underestimate of the dislocation density beneath the indent.

5.4.2 Dislocation bowing model for the (0001), $(10\bar{1}2)$ and $(10\bar{1}1)$ planes

It is reasonable to conjecture that the bowing out of GNDs, in the form of LAKBs, through SSDs is responsible for the energy dissipated per unit volume per cycle, W_d. A similar interpretation was reached by Roberts et al. [56] when it was concluded that bowing of dislocation networks were responsible for the hysteresis loops and reversible non-linear strain. The claim made herein is based on the fact that the physics involved in producing the nested loops must be *different* than the physics that is occurring during the classic work hardening regime, for which the work hardening rate is on the order of 1 GPa. In contradistinction, the hardening rates within the nested cycles – i.e. the slope of the top portion of each loading cycle in Fig. 5-6 – are at least *an order* of magnitude higher for each orientation. Since the hardening rate for the long range movement of the LAKBs through the SSDs is ≈ 1 GPa, it follows that the much higher hardening rates observed during cycling, might be related to the bowing out of GNDs in the LAKBs. In other words, the same mechanism invoked to explain the loops observed in the last chapter applies here as well.

Using Eq. 5-1, γ_B was calculated for each location as shown in Table 5-3. Assuming the measured change in contact radius due to dislocation bowing, $\Delta a_B \approx 0.7$ μm for 150 mN indents on the (0001) plane, $\Delta a_B \approx 0.25$ μm for 150 mN indents on the $(10\bar{1}2)$ plane and $\Delta a_B \approx 0.18$ μm for 150 mN indents on the $(10\bar{1}1)$ plane, the corresponding values for γ_B were 0.004, 0.0014 and 0.001 respectively.

Focusing now on W_d, which was defined as the area of a loop, and also equal $2\tau_f\gamma_B = 2\Omega\sigma_f\theta(\Delta a_B/a_o)$ (see Ch. 4 for derivation), where the factor of 2 accounts for the energy dissipated during loading and unloading, and τ_f is the energy dissipated when a dislocation sweeps a unit area by a the Burgers vector, **b**. As mentioned in the previous chapter, Ω is a factor that relates the shear stress on the basal planes, τ, to the applied NI stress, σ. Plots of W_d vs. $\Delta a_B/a_o$ (Fig. 5-7b) were generated for each orientation and these plots yield straight lines with a slope $\approx 2\Omega\theta\sigma_y$, further confirming that if τ_f is a function of stress it is a weak function.

Using the slopes from W_d vs. $\Delta a_B/a_o$ and values for σ_y at various locations on the different planes, values for Ω were calculated. As shown in Table 5-3, values of Ω varied in the range of 1.62 to > 3 with no strong dependence on orientation. Since the largest possible value of Ω is 0.5, these values are obviously too high However, given that these values were obtained using some quite simplifying and very crude assumptions and the lack of any adjustable parameters, suggests that the physics of the problem has been captured. The object of this exercise is to show that the dislocation bowing out model is indeed plausible.

Table 5-2. The values for Ω, L_N and the shear strain associated with dislocations bowing in a network, γ_B, are shown for each location on each orientation. The values for L_N in the table are calculated using the corresponding value for Ω and $\alpha = 0.5$.

Series	Load	Cycles	Location	Ω	L_N (μm)	γ_B
0001	50	50	1	1.79	0.31	0.0033
	50	50	2	1.93	0.27	0.0032
	150	50	1	2.33	0.26	0.0034
	150	50	2	1.89	0.31	0.0041
	150	50	3	2.21	0.28	0.0037
	150	50	4	1.79	0.31	0.0043
$10\bar{1}2$	50	50	1	1.86	0.18	0.0016
	50	50	2	1.69	0.20	0.0017
	50	50	3	1.62	0.21	0.0016
	150	50	1	2.80	0.15	0.0014
	150	50	2	2.56	0.15	0.0013
	150	50	3	1.95	0.20	0.0016
$10\bar{1}1$	150	50	1	3.26	0.10	0.0009
	150	50	2	2.88	0.11	0.0008
	150	50	3	2.72	0.11	0.0009
	150	50	4	1.72	0.15	0.0011
	150	50	5	2.15	0.13	0.0010
	150	50	6	2.48	0.11	0.0008

Similar to the results on the (0001) plane indentation in Mg in this study (Ch. 4), the bowing out idea is consistent with the stress trajectory when the maximum stress for a set of cycles is exceeded. The hardening rate regresses to a rate on the order of 1,000 MPa, at which point the dislocations in the LAKB that were freed from their moorings and start moving irreversibly over reasonably large distances to their new position given by the new maximum load. As an example, in Fig. 5-5a-b, as the applied load increases from 50 to 150 mN on the (0001) and ($10\bar{1}2$) planes, the LAKB moves a distance of ≈ 5 μm.

The fact that $\Delta a_B/a_o$ scaled as σ^2 (Fig. 5-7a) in this work on Zn can be attributed to the fact that both the area swept by the ith dislocation in a mosaic block of volume V, A_i, and the number of dislocations which bow per mosaic block, n are linear functions of σ (see Eq. 4-2).

Following Lucke and Granato's [75] rigid rod model, dislocations are assumed to move under a shear stress, τ, as a rigid rod and displaced a distance, y, that is constant along its whole length. Applying Eq. 4-5, with $y \approx \Delta a_B$, and assuming $\alpha \approx 0.5$ and $\Omega \approx 1$, then L_N is estimated to be of the order of 0.4 µm, 0.25 µm and 0.19 µm for indents loaded to 150 mN for 50 cycles on the (0001), the $(10\bar{1}2)$ and the $(10\bar{1}1)$ planes. Assuming these values for L_N, the normal stresses needed to bow dislocations to a radius 0.4 µm, 0.25 µm and 0.19 µm on the (0001), $(10\bar{1}2)$ and $(10\bar{1}1)$ planes were calculated using Eq. 4-8 to be $\sigma \approx$ 16 MPa, 27.6 MPa and 35 MPa respectively. And while these values are not equal to the measured yield stresses (see Table 5-2), they are reasonable being off by factors ranging between 2 and < 4. Here again, these results show that the physics of the problem has been successfully captured.

The results of this study enable an explanation of what is occurring beneath the indenter on the (0001), $(10\bar{1}2)$ and $(10\bar{1}1)$ planes. As in the case of nanoindentation on the (0001) plane in Mg, initially, no L_N segments in the LAKB bow out, which explains why the initial response is linear elastic until the yield stress σ_y, is reached. At σ_y, some of the dislocation segments begin to bow out. More segments bow out with increasing stress, until the maximum stress is achieved. The energy dissipated during the fully reversible hysteretic indentation stress vs. a/R cycles observed in this present study on Zn is thus due to the reversible bowing out of GNDs, in the form of LAKBs, through statistically stored ones. This conclusion is consistent with the claim made in the previous chapter on Mg for KNE solids that do not twin. Note that at this time we cannot exclude a contribution to W_d from motion of the <c+a> dislocations that must be present to explain the movement of the indenter normal to the surface indented, especially for the (000l) plane.

5.4.3 Discussion on the $(10\bar{1}0)$ plane nanoindentation

As previously mentioned in the results of nanoindentation on the $(10\bar{1}0)$ plane, neither reversible loops in the indentation stress vs. a/R curves (see Fig. 5-6a), twins or KBs (see Fig. 5-8c) were observed. When loading was applied on the $(10\bar{1}0)$ plane cyclically, the crystal work hardened after achieving a maximum stress, and subsequent cycles were loaded with a linear correlation until the maximum stress was achieved – as observed during classic work hardening. Since indentation was applied on the $(10\bar{1}0)$ plane, the in-plane deformation must account for strain both parallel and perpendicular to the c-axis to yield a spherical crater shown in Fig. 5-2d. It is thus reasonable to assume that non-basal slip was activated in lieu of twinning to accommodate c-axis strain. Non-basal slip was observed in a similar study [64] by Rosenbaum in which loading was applied parallel to the basal planes in Zn single crystals, as was the case in this study. It is worth noting that non-basal slip could also be activated when loading normal or parallel to the basal planes since the shear stress on the basal planes would be zero. Comparing the $(10\bar{1}0)$ orientation with the other orientations, where the rigid rod model [75] for dislocations bowing in a network was applicable, this same model is not valid in this orientation since dislocations did not form a LAKB. Thus, their motion is completely irreversible.

The material beneath indents on the $(10\bar{1}0)$ plane was polycrystalline with a variety of orientations (see Fig. 5-12), which may cause non-uniform stress distributions beneath the indent under loading. It remains unclear why reversible hysteresis loops in the NI stress vs. a/R curves were not observed; however, the absence of KBs and a sufficient number of basal dislocations capable of bowing out in a network are believed to be the reason for the absence of loops.

5-5 Summary

The reversible hysteresis effect of Zn was investigated under cyclic nanoindentation as a function of grain orientation. Fully and spontaneously reversible hysteresis loops were observed in the indentation stress vs. a/R curves when indentations were made on the (0001), $(10\bar{1}2)$, and $(10\bar{1}1)$ planes. This effect is most likely due to dislocations in LAKBs bowing out through statistically stored dislocations, as evidenced by the higher hardening rate compared to classic work hardening.

LAKBs were indirectly observed (see Fig. 5-8a and 5.8b) at each location where the hysteresis effect was observed, further supporting the idea of LAKB dislocations bowing out. Whenever no kinks were observed, (see Fig. 5-8c) - such as beneath indents on the $(10\bar{1}0)$ plane - no hysteresis loops were observed. No evidence for twinning was observed at any location in this study. Instead, non-basal slip is believed to be activated in the absence of twinning to accommodate c-axis strain – in which it was deduced these dislocations are irreversible. More detailed TEM analysis of the microstructure beneath indents is needed to fully understand why loops were not observed in the absence of LAKBs, or to even understand the microstructure beneath indents when KBs formed. Lastly more work is needed to understand why, after cycling, the stiffness of the Zn in most orientations, but especially in the case of the $(10\bar{1}0)$ plane, is significantly greater than what is predicted from the elastic constants.

CHAPTER 6: NANOINDENTATION ON Ti_3SiC_2

6.1 Background on Ti_3SiC_2

Jeitschko et al. [76] were among the early pioneers in 1963 to synthesize a new class of materials known as H-Phases, which are ternary layered carbides with certain properties that would later become included in a larger class of materials known as MAX phases. Belonging to the space group P63/mmc and possessing a hexagonal crystal structure, some outstanding properties of the MAX phases includes good electrical [77] and thermal conductivity [78, 79], easily machinable, excellent thermal shock resistance [79] with some compounds being high temperature oxidation resistant. To date, more than 60 MAX phase compounds have been synthesized. Some examples of well studied MAX phases include Ti_2AlC, Ti_3SiC_2 and Cr_2GeC.

As a complex layered material, the deformation micromechanisms in the MAX phases have yet to be explained. Several studies [11, 53, 67, 80, 81] have investigated deformation of MAX phases and it is well established that both kink band formation and basal slip are primary deformation mechanisms in the MAX phases. Molina et al. [82] used nanoindentation on Ti_3SiC_2 thin film using a Berkovich tip, and examined a cross sectional lift out of the indentation in the TEM revealing kink bands and delamination. It was believed that mobile dislocation walls (MDWs), which were identified in TEM micrographs, accumulated to form the kink boundaries, lending some credence to the possible existence of IKBs (see Ch. 2).

The basal slip system is believed to be the only operative slip system in the MAX phases and the basal interatomic vector, $\frac{1}{3}\langle 11\bar{2}0\rangle$, is the shortest full translation vector. Non-basal dislocations would require a large Burgers vector due to the large c/a ratio (typically > 3) in the MAX phases, which makes their existence impossible. No evidence to date has identified dislocations in MAX phases deformed at room temperature (RT) which are non-basal, although in an early study on the MAX phases at RT by Farber et al. [80], very few dislocations were observed in an isolated case that did not lie totally in the basal plane. Despite the fact that some out-of-plane dislocations having been observed in some MAX phases [83, 84], these dislocations do not contribute to plasticity.

No evidence for dislocation entanglement or cross slip has been reported in deformation of MAX phases at RT; however, in a study by Guitton et al. [85], evidence of dislocation cross slip at high temperatures (900° C) was observed. At RT, basal dislocations are mobile, which glide along their basal planes leading to dislocation arrays (pile-ups) or walls [29, 67], the latter of which are believed to form kink boundaries (see Ch. 2). Lastly, twinning has not been reported in the MAX phases, as the likelihood of twin formation is small owing again to the large c/a ratio [67].

One of the more unique and fascinating phenomena observed in the MAX phases is their unique ability to deform plastically without any physical damage [23], evidenced by fully reversible hysteresis stress-strain loops result after cyclic loading. Numerous studies have investigated possible explanations to this phenomenon in the MAX phases [27, 67], and also the nonlinear reversible strain in other materials ($LiNbO_3$ [68], mica [30], sapphire [24], graphite [18], Mg [25]) in which this effect has been observed. One study [67] investigated both coarse grained (CG) and fine grained (FG) polycrystalline Ti_3SiC_2 under compression at RT and at high temperature (1000 °C), and the FG Ti_3SiC_2 exhibited reversible loops up to 1 GPa and a strain of 0.006 at RT, while open loops resulted at higher temperatures. At RT, this study also found the stress-strain loops to be very reproducible and strain rate independent. The reversible non-linear plastic strain was attributed to both IKBs and dislocation pile ups [28, 67] on Ti_3SiC_2, where the strain due to dislocation pile ups was said to be reversible due to the layered structure of KNE solids. It was concluded in the same study that the strain due to dislocation pile ups on different planes was negligible compared with the strain due to the IKBs.

A study by Murugaiah et al. [23] reported fully reversible stress-strain loops under nanoindentation (NI) of Ti_3SiC_2 with loading applied normal to the basal planes, and little physical damage was observed. On the contrary, when indentation was applied parallel to the basal planes, delamination and cracking occurred. The mechanism believed to be responsible for the stress-strain loops was the growth and annihilation of IKBs.

Other studies [86, 87] have suggested that the reversible hysteresis is the result of micro-cracking. Lawn and Marshall [86] developed a microscale model to explain the nonlinear hysteresis in stress-strain curves based on friction due to sides of cracks sliding past one another and also crack configuration parameters. Poon et al. [87] studied Ti_2AlC under cyclic uniaxial compression and developed a microscale model based on the previous model by Lawn and Marshall [86] to explain the stress-strain hysteresis loops observed in their study. They concluded that the hysteresis effect in Ti_2AlC could be explained based on the crack density and friction coefficient.

In 2014, Jones et al. [88] used in situ x-ray diffraction (XRD) to study lattice strains of Ti_3SiC_2 under uniaxial compression, and nanoindentation on Ti_3SiC_2 and Ti_3SiC_2/TiC films on Al_2O_3 to study the reversible hysteresis loops in the stress-strain curve. Residual elastic lattice strains were noted as developing during the first loading cycle and remaining approximately constant for all subsequent cycles. Jones et al. [88] conjectured that the origin of the hysteresis loops was the result of residual elastic lattice strains, which result in part due to a limited number of slip systems. This explanation was in contrast to IKBs as the dislocation based mechanism that was used to describe the same effect. The origins of the hysteresis loops in the stress-strain curves remains an open question both in the MAX phases and in other KNE solids.

6.2 Experimental details

A highly oriented coarse-grained (CG) Ti_3SiC_2 bulk sample was used in this study. The sample was synthesized by mixing Ti (99.9% metal basis, Alfa Aesar), Si and C (Alfa Aesar) elemental powders in stoichiometric ratios and hot pressing at 1450° C under a stress of 25 MPa for 4h. To coarsen the grains, the sample was annealed at 1550° C for 72 h in Ar resulting in average grain sizes 200–500 μm. X-ray diffraction (XRD) was used to verify the purity and identify any possible secondary phases (Fig. 6-1). The sample was mostly pure with only trace amounts of SiC present.

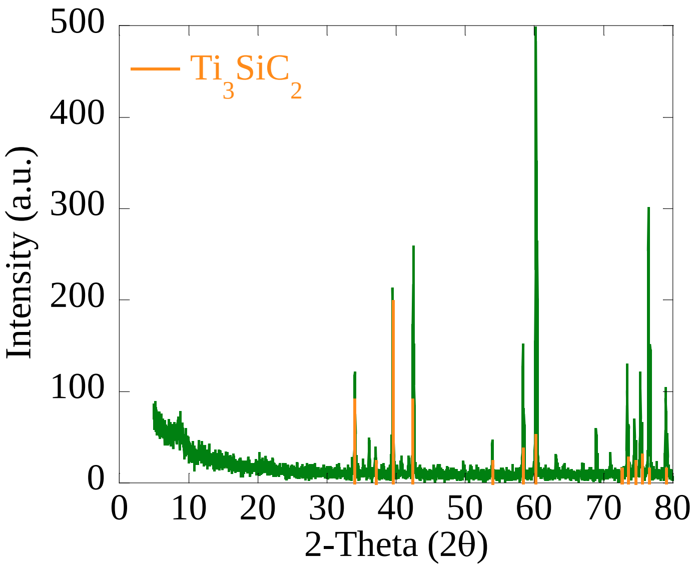

Figure 6-1. X-ray diffraction (XRD) pattern of highly oriented coarse-grained Ti_3SiC_2 sample used in this study.

The sample was mounted onto an Al mount, ground using 600–1200 SiC grit paper and polished down to ¼ diameter particle size using a water-based suspension. Finally, the sample was vibropolished to 0.05 μm diameter sized particles using an alumina suspension. Since the MAX phases are typically oxidation resistant, the sample was stored in air between experiments.

A SEM equipped with EBSD was used to generate an OIM map of the different grains, whose size was on the order of 200-400 μm (see Fig. 6-2). The focus of this study emphasized grains on which indentation could be applied on the (0001) or the $(10\bar{1}0)$ planes.

Repeated nanoindentation, NI, in the same location was performed in CSM mode on selected grains using a 100 μm spherical tip initially with a targeted strain rate of 0.1 s^{-1}. Each NI experiment consisted of loading to a maximum load and unloading to a minimum load (5 mN) either 25 or 50 times followed by a series of nested cycles consisting of 20 – 100% of the maximum load. Table 6-1 shows a summary of NI experiments on Ti_3SiC_2 in this study.

Since most indentation marks made using the 100 μm spherical tip were below the resolution limits of the SEM, even when using the maximum load of 550 mN, a 21 μm spherical tip was also used to achieve a higher stress so that indents could be observed in the SEM (see Table 6-1). Once the indents were observed, cross-sectional lift outs at select locations became feasible using a FIB.

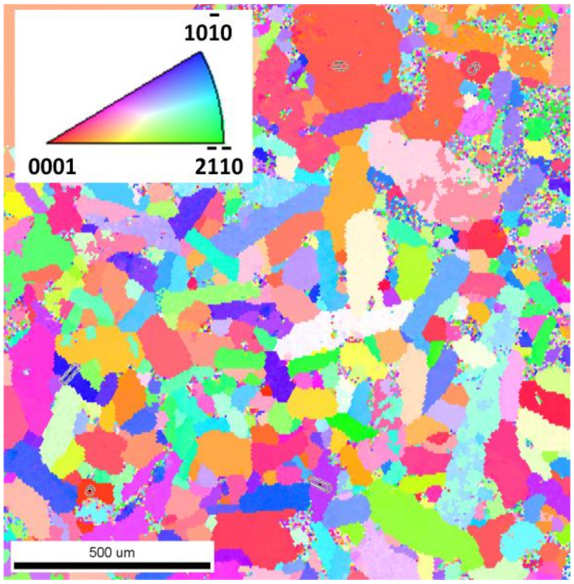

Figure 6-2. OIM map generated using EBSD of different grains in Ti_3SiC_2.

In most metals and glasses subjected to cyclic loading, the first indentation stress vs. a/R cycle is open. Subsequent cycles become less open, until the area of the loops, W_d, become vanishingly small [89]. However, in previous work, mostly, on single crystal ceramics, a quite different response was observed [30, 90, 91]. The first cycles were again open, but subsequent cycles were less open, until ultimately fully and spontaneously reversible, closed, load-displacement and concomitant NI stress-strain loops developed. In this study, the indentation stress vs. a/R curves are studied, since a/R is related to the strain as mentioned in Ch. 3. More importantly as in this thesis, $\Delta a_{B/} a_o$ can be directly related to shear strain under the indenter (see Eq. 4-4). The number of cycles needed for full reversibility varies from material to material, but is typically of the order of 8-10 cycles in MAX phases. By cycling 25 or 50 times, the loops were assured to be closed.

Table 6-1. A list of nanoindentation experiments carried out herein. The list includes details about the grain orientation, tip size, load and number of cycles.

Orientation	Grain	Loc	Tip (µm)	Load (mN)	Cycles
(0001)	**A**	1	100	550	25
		2			
		3			
		4			50
		5			
	B	1	100	500	50
		2			
		3	21	500	50
		4			
		5			
		6			
	C	1	100	500	50
		2			
	D	1	21	500	50
		2			
		3			
		4			
$(10\bar{1}0)$	**E**	1	100	550	25
		2			
		3			
		4			50
		5			
		6			
	F	1	21	400	50
		2		500	

After the cyclic NI experiments were performed, the contact radii of the indents that were within the resolution limits of the FIB-SEM were measured. Some indents were circular with no cracks or kinks (Fig. 6-3a), while others showed some visible damage in the form of cracks (Fig. 6-3b-c). In a few cases, indents were mistakenly made near, or at, grain boundaries as shown in Fig. 6-3d. Figure 6-3e shows a typical area where an indent was made using a 100 µm tip loaded to the maximum load, which was below the SEM resolution limits.

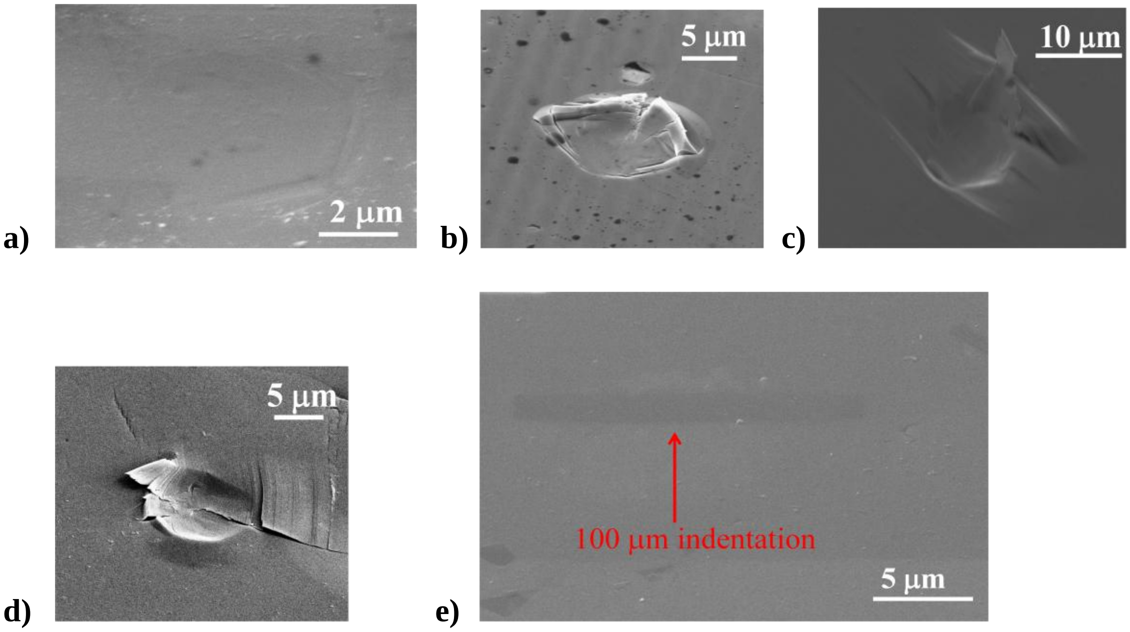

Figure 6-3. SEM images of indentations made on different Ti_3SiC_2 grains. a-b) Indentations on (0001) plane using a 21 µm tip. c) Indentation on $(10\bar{1}0)$ plane using 21 µm tip. d) Indentation made at grain boundary of (0001) and adjacent grain using a 21 µm tip. e) SEM image of area where indent B2 (See Table 6-1) was made using 100 µm and loaded to 500 mN at the beginning of Pt deposition in the FIB. Image is taken at a 52° tilt, which should make detecting the indent trivial. However, as seen in this image, the indent is essentially below the SEM resolution limits.

The surface topography around select indents was examined using an AFM, especially when the residual marks were near the resolution limits for the SEM, i.e. for the 100 µm indents. Cross-sections of select indents were lifted out and examined in the TEM to better understand the microstructure beneath the indents.

Instrumental drift was corrected in one of two ways; i) load vs. displacement data was shifted to correspond to the contact radius measured in the SEM, a_{SEM}, when the latter could be measured or, ii) load vs. displacement cycles were plotted separately to determine when adjacent cycles were identical, and all subsequent cycles were shifted accordingly. The latter was used when indent contact radii were beneath the resolution limits of the SEM.

6.3 Experimental Results on Ti_3SiC_2

6.3.1 NI results using 100 μm spherical tip

The load vs. displacement curves at one location on the (0001) and $(10\bar{1}0)$ planes are shown in Fig. 6-4a and 6-4b respectively. The specific locations correspond to location 4 on grain A and location 4 on grain E (see Table 6-1), hereinafter referred to as A4 and E4, respectively. The maximum load used was 550 mN for 50 cycles. These curves were then converted to NI stress vs. a/R curves (see Fig. 6-5a-b) using the analysis discussed in Ch. 3.

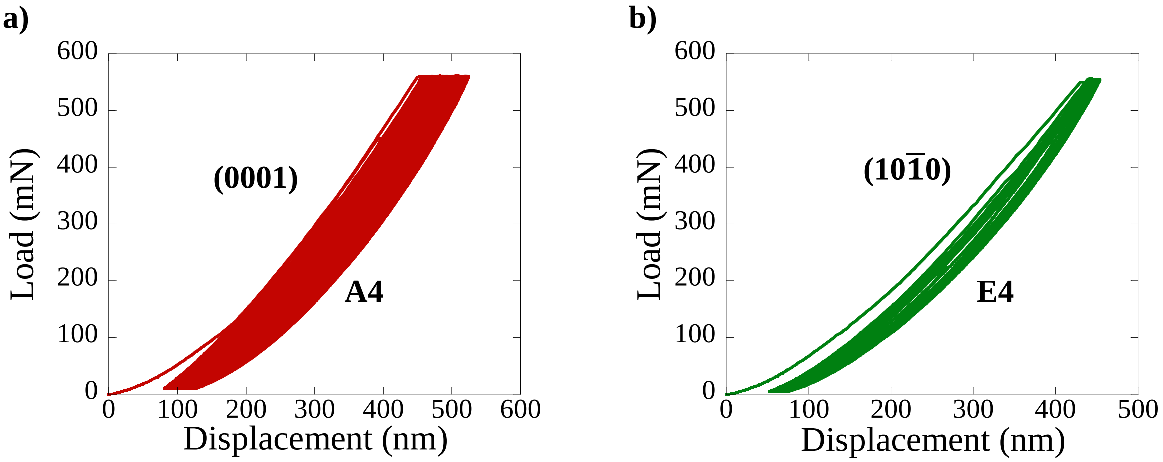

Figure 6-4. Load vs. displacement curves for, a) location 4 on grain A (refer to Table 6-1) on the (0001) plane and, b) location 4 on grain E on the $(10\bar{1}0)$ planes loaded to 550 mN for 50 cycles.

The first cycle mechanical response varied from location to location, and it remains unclear why such discrepancies were observed. For example, the slope during the first cycle of loading deviated from the expected modulus, 325 GPa, for both locations A4 and E4 as shown in Fig. 6-5, while other locations (see Fig. 6-9a) showed a more reasonable fit to the elastic modulus expected from Hertzian analysis during the first cycle. It is important to note that all of the initial slopes of the nested loops obtained after cycling (see dashed lines in Fig. 6-6) corresponded to moduli of ≈ 325 GPa.

The values for a/R ranged between < 4% for indents made on the $(10\bar{1}0)$ plane to approximately 5% for indents made on the (0001) plane at locations similar to those shown in Fig. 6-5. As noted above, despite these a/R values and using the instrument's maximum applied load in both planes, indents were below the resolution limits of the SEM and were thus not investigated in the TEM. This fact suggests that between when the indentation experiment are carried out and when they are observed in the SEM, the surface recovers. It would thus be very instructive to carry out some in situ NI studies in a SEM to observe this recovery in real time.

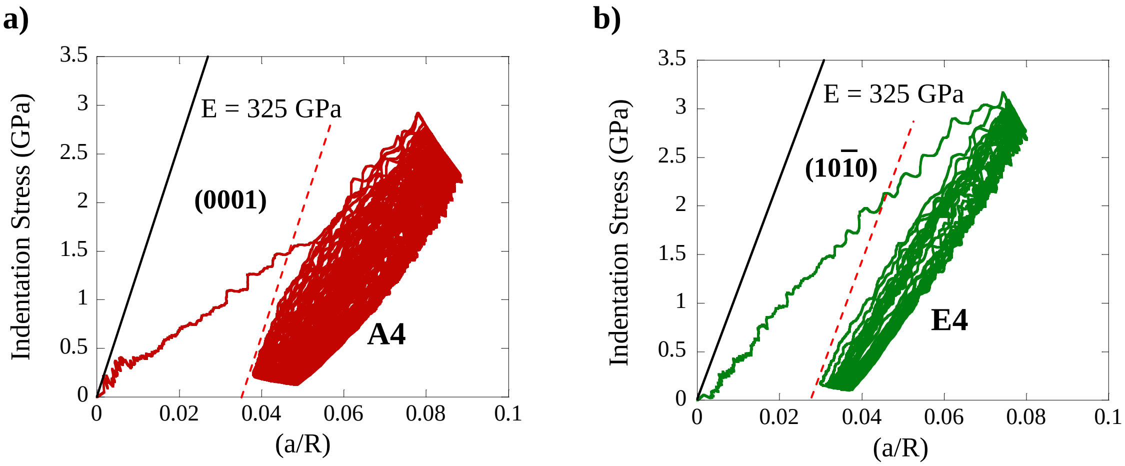

Figure 6-5. Indentation stress vs. a/R curves for locations, a) A4 on (0001) and, b) E4 on $(10\bar{1}0)$ planes. The indenter radius was 100 µm and the load was 550 mN, as shown in Table 6-1.

The indentation stress vs. a/R curves for the nested cycles at locations A4 and E4 were plotted in Fig. 6-6a. These curves are quite typical of all other locations. The nested cycles from the location loaded on the $(10\bar{1}0)$ plane were shifted to the left by 0.0015 for clarity. In contrast to the first loading cycle, the slope in the linear elastic regime of the nested cycles was a reasonable fit to the Young's modulus for Ti_3SiC_2, which is 325 GPa. Each nested sequence started as linear elastic until the yield stress, σ_y, was reached, at which point the indentation stress vs. a/R curve changed slope. As in previous chapters, the point at which the curves changed slope was designated as the yield stress, σ_y. The change in slope also corresponds to the emergence of the fully, and spontaneously, reversible loops.

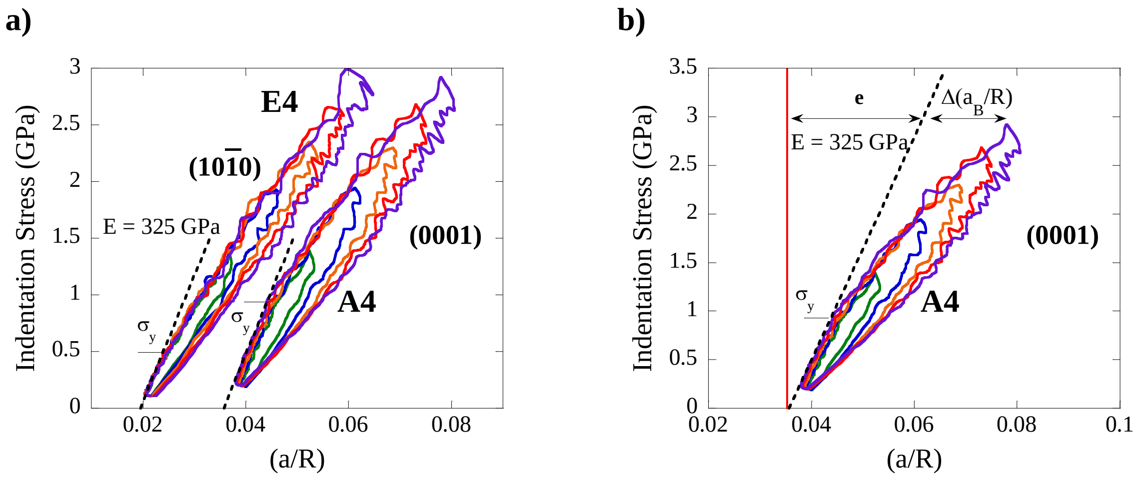

Figure 6-6. a) Indentation stress vs. a/R curves for nested cycles on the (0001) and $(10\bar{1}0)$ planes. The nested sequence for the $(10\bar{1}0)$ plane was shifted to the left by 0.0015 for clarity. Dashed lines corresponds to an elastic modulus of 325 GPa, and σ_y is the yield stress for a given nested sequence. b) $\Delta(a_B/R)$ is equal to the total non-linear reversible a/R, which is calculated by subtracting the elastic portion from the total a/R.

In Fig. 6-6a, σ_y observed for the indentation made on the (0001) plane at location A4 was ~ 1 GPa; the yield stress for the indent made on the $(10\bar{1}0)$ plane at location E4 was ~ 0.5 GPa. Both nested sequences showed reversibility up to ~ 3 GPa with no damage observed in post-indentation SEM micrographs (see Fig. 6-3e). A similar observation was made when Murugaiah et al. [23] who performed NI on Ti_3SiC_2 normal to the basal planes and reported hysteresis loops in the stress-strain curves with no detectable imprint or post-indentation damage.

The change in contact radii in the post-yielding regime, $\Delta a_B/R$ (defined in Fig. 6-6b) were measured for each cycle. The latter was then converted to $\Delta a_B/a_o$ values. Since no permanent mark was visible in the SEM after indentation in both cases, a_o was taken as the contact radius after the 10th cycle, beyond which the material is not believed to deform plastically. The values for $\Delta a_B/a_o$ were then plotted against σ^2 (see Fig. 6-7a) and W_d (see Fig. 6-7b) for both locations

A4 and E4 with better values for R^2 resulting from the location A4, which was indented on the (0001) plane. The values for R^2 from plots of $\Delta a_B/a_o$ vs. σ^2 and W_d were > 0.99 and > 0.98 for the indent made on the (0001) plane (location A4), and > 0.99 and for the indent made on the $(10\bar{1}0)$ plane (location E4). It is important to note that these linear fits are approximations.

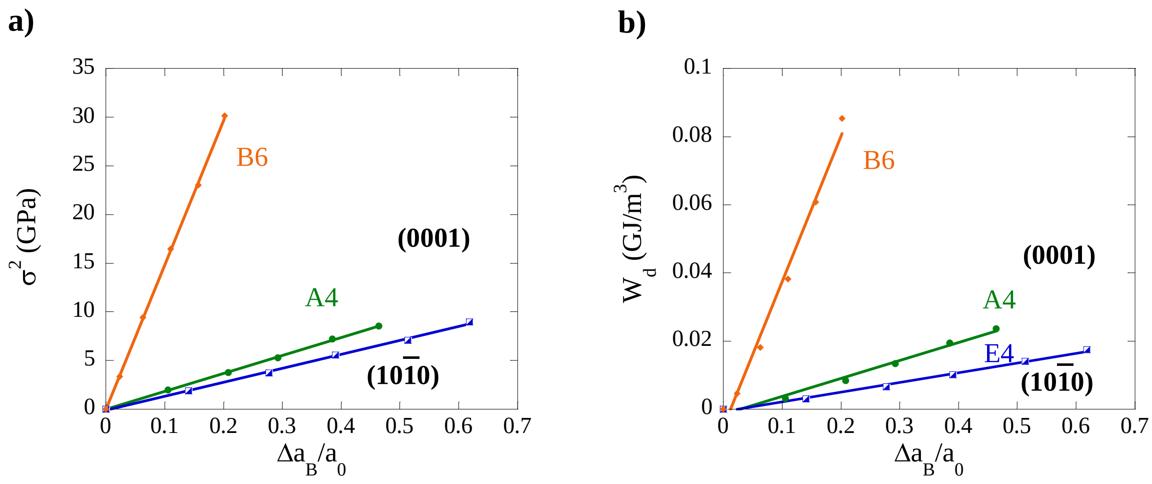

Figure 6-7. $\Delta a_B/a_0$ plotted against, a) σ^2 and, b) W_d at locations A4 (green circles) and E4 (blue squares) on the (0001) and $(10\bar{1}0)$ planes. The maximum load was 550 mN and 50 cycles were used along with a 100 μm tip. Also plotted is $\Delta a_B/a_0$ vs. σ^2 and W_d at location B4 (orange), which was loaded to 500 mN using a 21 μm tip.

Lastly, it is worth mentioning that the difference between using 25 and 50 cycles was small, with more cycles resulting in slightly harder material and slightly larger loops. Thus, for the sake of consistency, locations where 50 cycles were used were presented in this section. For plots obtained after 25 cycles, refer to Fig. A1 in Appendix A.

6.3.2. NI results using 21 μm spherical tip

The load vs. displacement curves from indents made on the (0001) (location B6) and the $(10\bar{1}0)$ (location F2) planes using a 21 μm spherical tip are shown in Fig. 6-8a and 6-8b respectively. As shown in Table 6-1, the loads were applied 50 times in the same location to a maximum load of 500 mN. Figure 6-8a shows the typical load vs. displacement curve when loading was applied on the (0001) plane with a small amount of drift. Figure 6-8b, shows the response that was observed when using a 21 μm spherical tip on the $(10\bar{1}0)$ plane to a maximum load of 500 mN. The load vs. displacement curve is separated into two regimes, the first of which consists of only the first two cycles, and the second regime contains all other cycles beginning with the third cycle. A similar observation (not shown) was made in this study when loading to 400 mN on the $(10\bar{1}0)$ plane. One distinction between indents on both planes was the presence of cracks around indents made on the $(10\bar{1}0)$ plane (see Fig. 6-3c) and the absence of cracks when indenting on the (0001) plane (see Fig. 6-3a) under such high stresses. The observations made herein are consistent with those reported in a study by Murugaiah et al. [23], in which nanoindentation applied parallel to the basal planes on Ti_3SiC_2 using a 13.5 μm spherical tip resulted in two load vs. displacement regimes, which was attributed to the delamination cracks that were observed in SEM images.

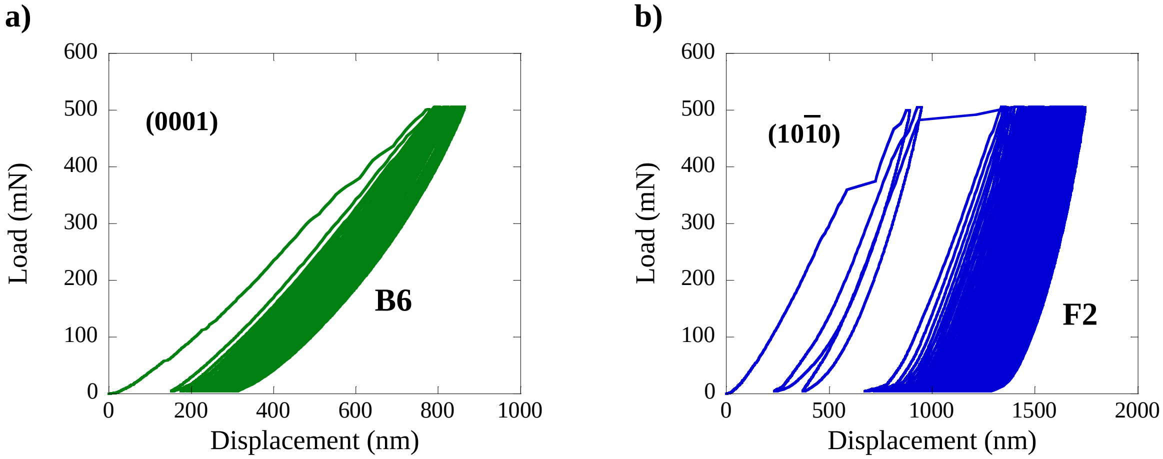

Figure 6-8. Load vs. displacement curves for, a) location 6 on grain B on the (0001) plane, and b) location 2 on grain F loaded on the $(10\bar{1}0)$ planes to 500 mN for 50 cycles using a 21 μm tip.

In this study, when the NI stress vs. a/R curves (see Fig. 6-9), are plotted, each curve started as linear elastic with a reasonable fit to the elastic modulus (325 GPa) for Ti_3SiC_2 and achieved a maximum stress ~ 7 GPa during the first cycle. In Fig. 6-9a, loading of subsequent cycles was similar to that which was observed when using a 100 μm spherical tip. However, Fig. 6-9b shows two regimes in the NI stress vs. a/R curve. After the first regime consisting of only two cycles, the crystal beneath the indenter becomes significantly softer as the maximum stress for all subsequent cycles decreasing to > 2 GPa. As discussed below, this was likely due to crack nucleation and growth.

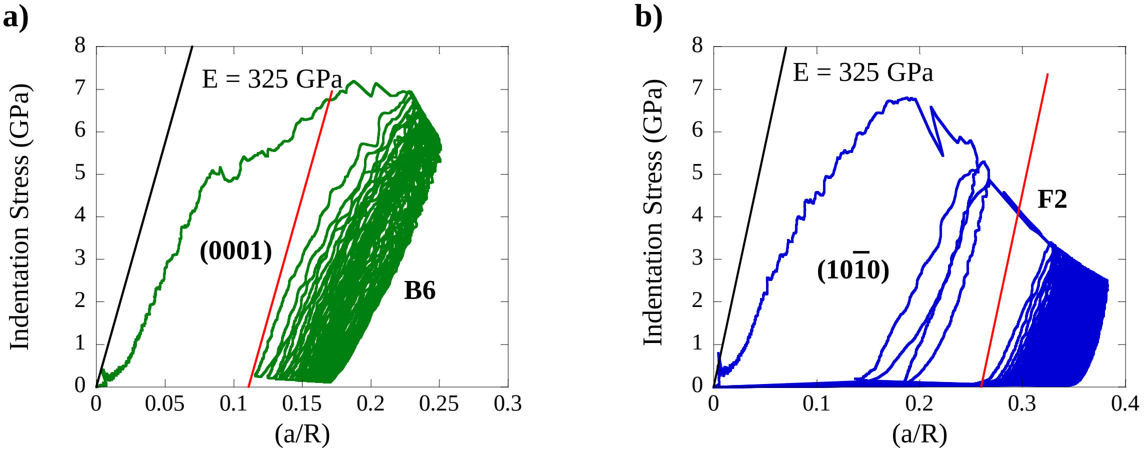

Figure 6-9. Indentation stress vs. a/R curves - loaded to 500 mN for 50 cycles using the 21 μm tip - for locations, a) B6 on (0001) and, b) $(10\bar{1}0)$ planes.

Figure 6-10a and b shows the NI stress vs. a/R curves for the nested cycles at locations B6 and F2, respectively. Fully reversible loops to a maximum stress > 6 GPa are shown in Fig. 6-10a, where loading was applied on the (0001) plane. Murugaiah et al. [23] reported stresses as high as ~ 9 GPa in their NI study on Ti_3SiC_2, which are slightly higher than those observed in this study. Note the similarities in the shape of the loops in Fig. 6-10a with those in Fig. 6-6. The values for a_o were obtained from a post-indentation SEM image for indent F2, and AFM was used to measure a_o for indent B6 since the resolution at this location in the SEM made measurements difficult and imprecise.

Figure 6-10b shows the nested loops when loading was applied to the prismatic plane, which shows a different shape and character than the loops previously observed. Note that the drift was not corrected at this location on the prismatic plane since these loops were not used in further analysis. The shape of the loops is the key observation to be made. The radius measured in the SEM at this location was 5.2 ± 0.3 μm, which corresponds to an a/R value ~0.25. Thus, much of the displacement in Fig. 6-8 is simply drift.

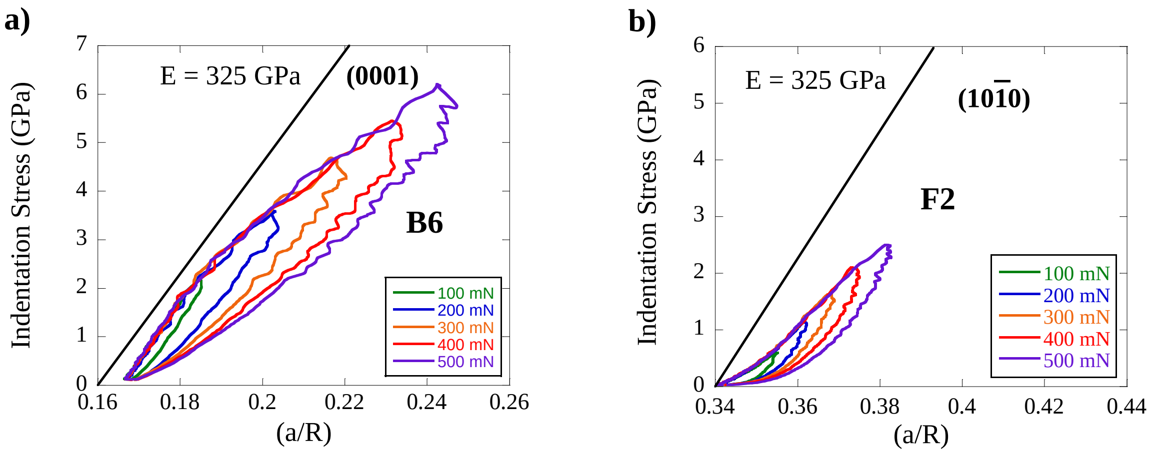

Figure 6-10. Nested cycles for the locations, a) B6 on 0001 and, b) F2 on $10\bar{1}0$ planes.

A similar observation was made in a different grain at a location on the (0001) plane, in which kinks and cracks were present beneath and around the indent. Figure 6-11a-c shows the load vs. displacement, indentation stress vs. a/R and the nested cycles at this location, respectively. The nested loops are the feature to focus on here, since the loops are very similar to those which were observed when the indentation applied was on the $(10\bar{1}0)$ plane (Fig. 6-10b) using a 21 μm tip.

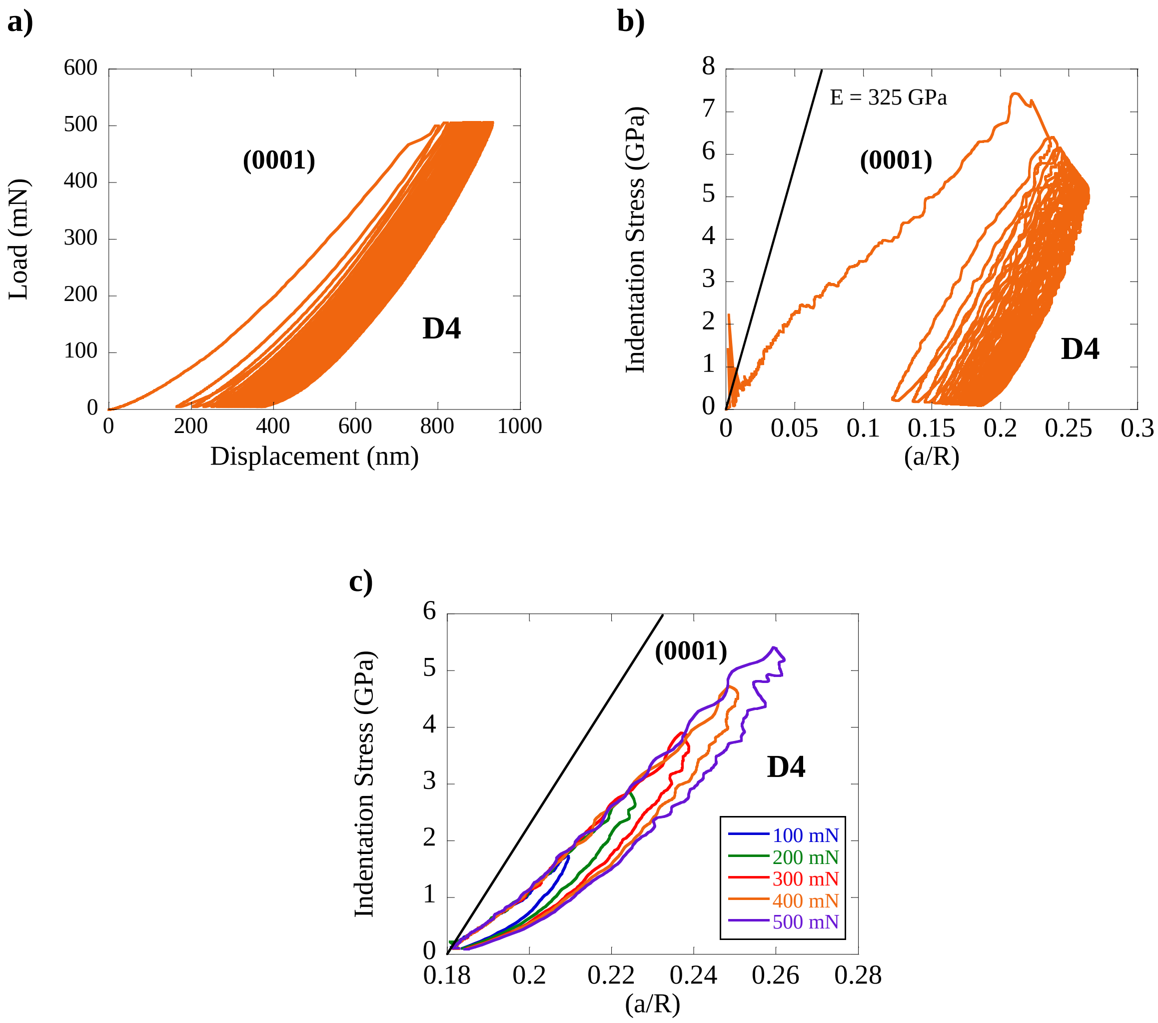

Figure 6-11. a) Load vs. displacement, b) indentation stress vs. a/R and, c) nested cycles are shown for indent D4 (location 4 on grain D). The maximum applied load was 500 mN for 50 cycles using a 21 μm tip. An SEM image of this indent is shown in Fig. 6-2b, where cracking was clearly observed.

Focusing once again on the nested cycles at location B6, Δa_B, was calculated and plotted against σ^2 (see Fig. 6-7a) and W_d (see Fig. 6-7b). The values for R^2 from these two plots were > 0.99 and > 0.98 respectively, which indicate reasonable fits to the lines.

6.3.3 AFM and TEM observations

Indentations made using the 100 µm tip were, in general, below the threshold limits of the FIB-SEM. An attempt was made to study the area around indent B2, which was made using a 100 µm tip and a maximum load of 500 mN. However, for reasons that are not understood, the indent was not located in the area where it was made as seen in the AFM data (see Fig. 6-12a-b). When using a 100 µm tip, the NI data typically records indent depths to be on the order of ~ 70 nm after the first cycle. However, the NI data at location B2 during initial loading was imprecise in that the load vs. displacement and indentation stress vs. a/R curves exhibited an unusual amount of displacement and deformation at such low stresses. Indentations made using a 21 µm tip were typically located and imaged in the SEM (see Fig. 6-3). Once an indentation was located within a small area, AFM was used in the small area to study the topography within and around the indent (see Fig. 6-12c), confirming the shape of the crater was indeed spherical. Line scan profiles taken across the indent confirmed the depth of the crater was on the order of ~ 170 nm, as shown in Fig. 6-12d. The indentation depth in the load vs. displacement curve at this location after the first cycle was ~ 150 nm, and ~ 174 nm after the second cycle and finally ~ 300 nm after the final cycle (see Fig. 6-8a). Much of the excess displacement was due to drift. Therefore, the AFM measurement used as the accurate measurement of the total displacement into the surface for later calculations discussed below.

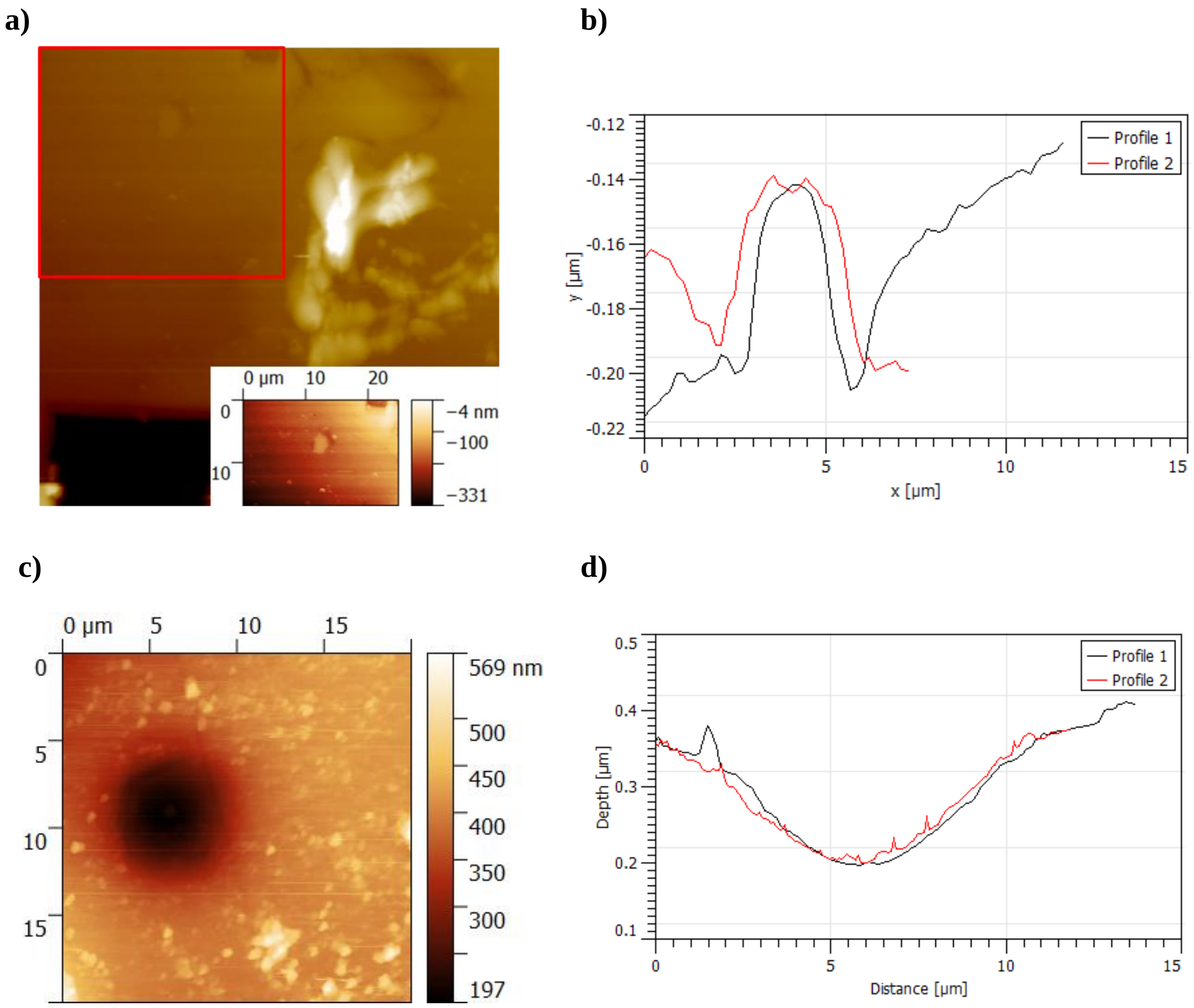

Figure 6-12. a) AFM image of area where indent B2 was made using a 100 µm tip and 500 mN load (see Fig. 6-3e for SEM image). The red box is the area where the indent should be with a distinguishable feature (inset) in the area that resembles the indent. However, the line scan profiles in b) suggests it may be a surface feature and not the indent. c) Atomic force microscopy (AFM) image of indent B6 loaded to 500 mN for 50 cycles using a 21 µm tip (see Fig. 6-3a for SEM image). d) Line scan profile across indent horizontally (profile 1) and vertically (profile 2).

Shifting focus now to the TEM work, cross sectional lift outs were made of select indents. The TEM data in Fig. 6-13 shows low magnification bright field images of the cross section of indents B2 and B6. Indent B2 (Fig. 6-13a) appeared to be more FIB damaged and thicker than indent B6 (Fig. 6-13b –c). Periodic streaks that were parallel to the basal planes were observed throughout the TEM micrograph in regions directly beneath both indents. The streaks are more discernible beneath indent B6 (Fig. 6-13b –c), which was loaded to 500 mN using a 21 μm tip. Figure 6-14 shows a weak beam dark field image beneath indent B6, where the bright spots in the image correspond to c-axis strain. The parallel streaks were imaged at a higher magnification (Fig. 6-15a) and further investigated. Bragg filtering (see Fig. 6-15b) was applied to the TEM micrograph to reveal that some atomic layers appeared to bend in areas surrounding the dark streaks. Away from the streaks, the basal planes appeared undistorted as shown in the Fig. 6-15b. No definite boundary between the indent and surrounding matrix was identified, nor were subsurface cracks or delaminations observed beneath indent B6. Selected area diffraction (SAED) patterns taken at different locations beneath the indent, and surrounding region (Fig. 6-16), did not reveal any changes in orientation. This is perhaps among the first MAX phase samples to exhibit clear permanent deformation with c-axis strain that did not result in kinking or failure. Other studies which observed c-axis deformation either resulted in kinking and/or delamination [82], or no damage [23] at all.

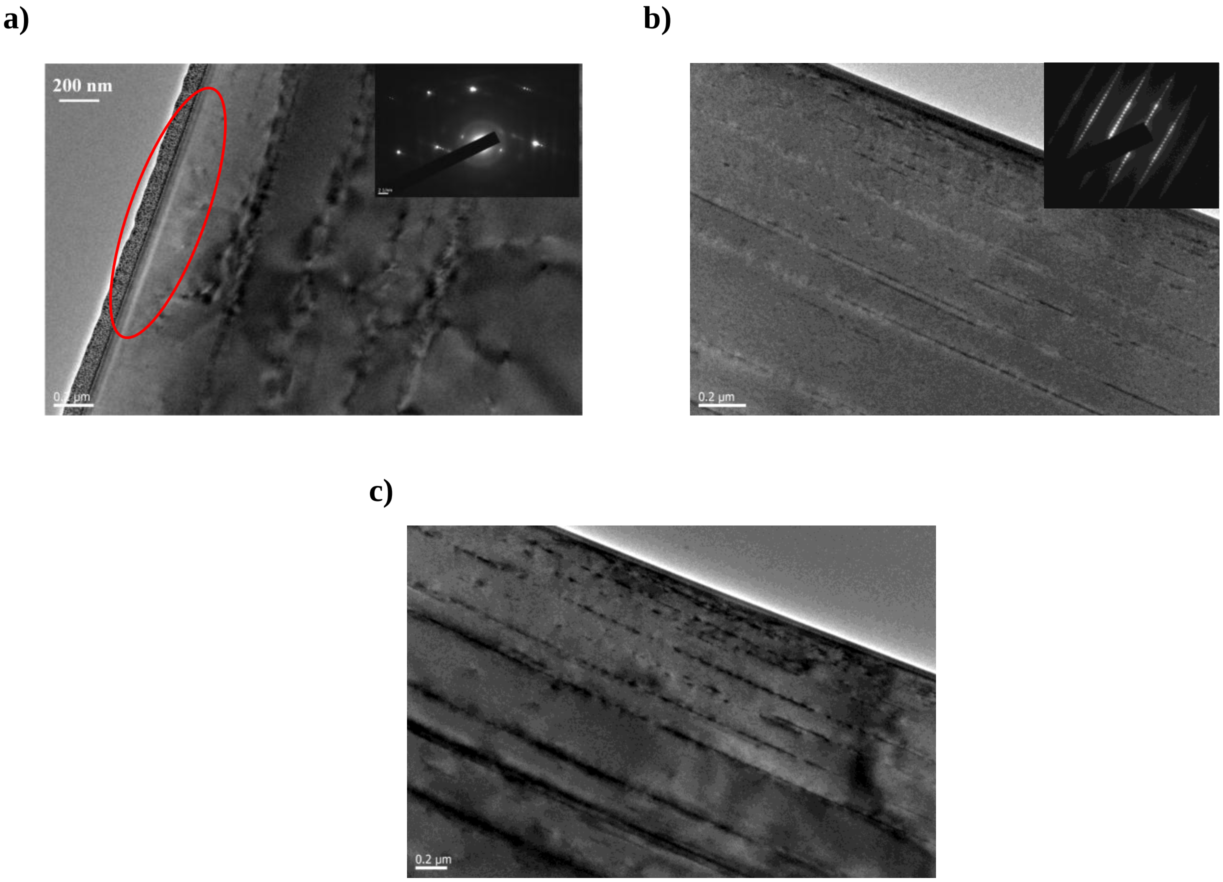

Figure 6-13. a) Low magnification bright field images taken beneath indent B2, which was loaded using a 100 μm tip at 500 mN. The red oval is where the indent is approximately located in the image. This image was not taken on zone axis, as seen from the DP in the inset. (b-c) Low magnification bright field images taken beneath indent B6 showing streaks parallel to the basal planes throughout the entire lift out. The zone axis from which images were taken is shown in inset. The streaks are seen more easily in image (b) due most likely to the strain contrast in the image, especially around the streaks.

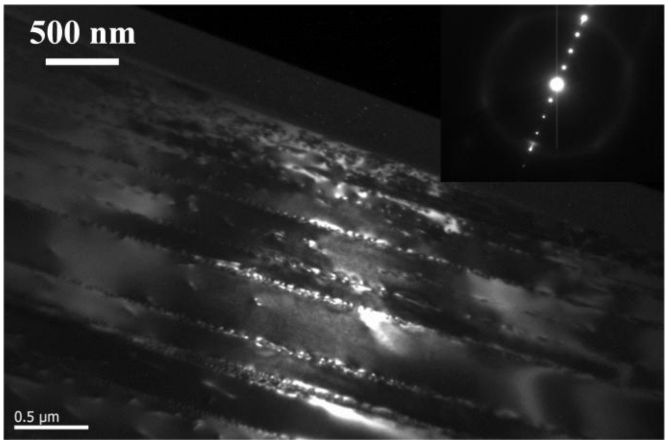

Figure 6-14. Low magnification weak beam dark field TEM image of indent cross section. Bright spots in the image correspond to c-axis strain appearing in contrast. Diffraction pattern of imaging condition is shown in inset.

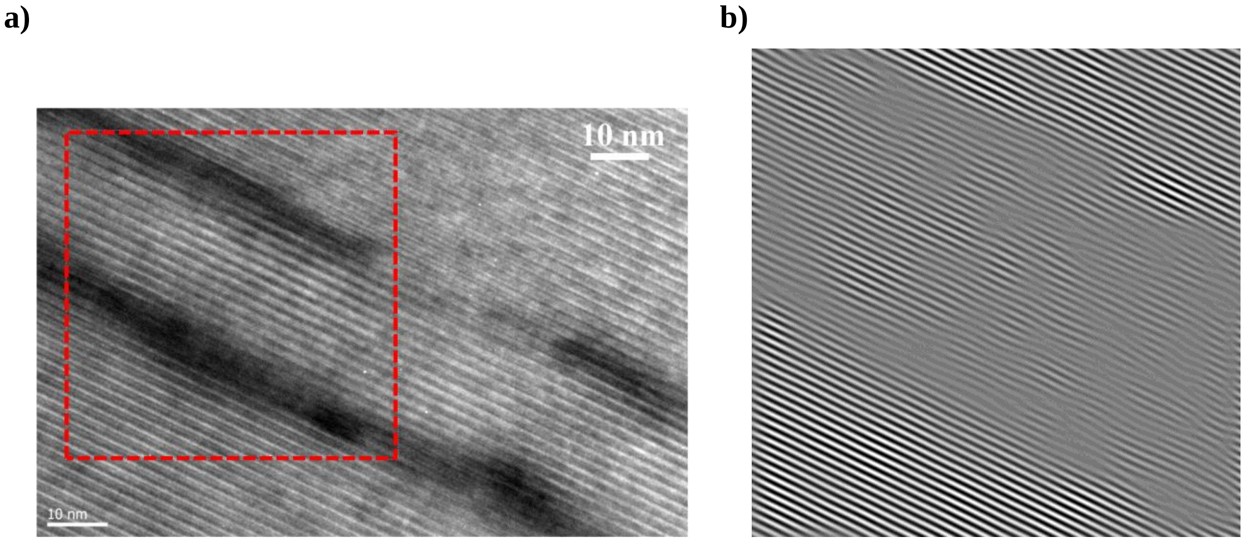

Figure 6-15. a) High magnification image of streaks in bright field image. The red rectangle is a region of interest (ROI) in which further analysis was done. b.) Image of ROI after Bragg filtering showing bending of atomic planes around the streaks with no distortion away from the streaks.

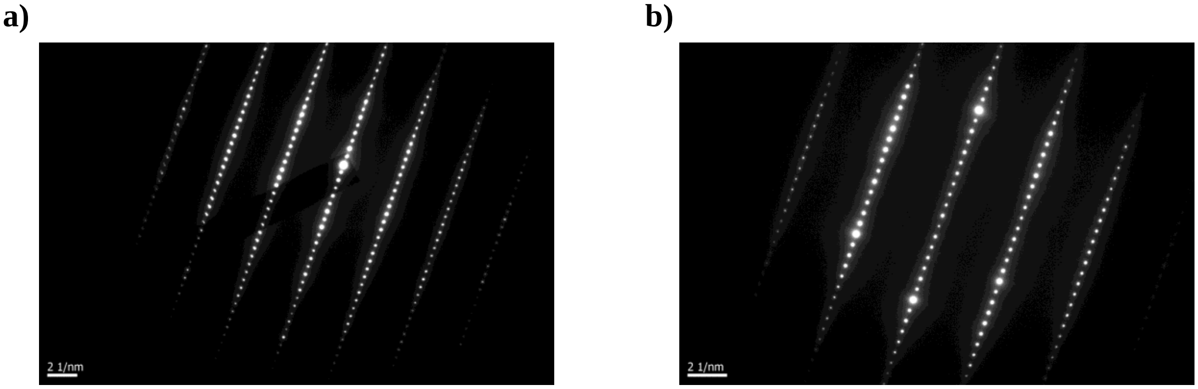

Figure 6-16. SAED patterns a) beneath indent B6 and, b) away from indented region using largest aperture.

After an indentation was made near a grain boundary, delaminations and cracks were observed as shown in Fig. 6-17. Cracking may have been a result of the grain boundaries pushing apart (see Fig. 6-18a). Kinks were also observed as shown in the dark field image in Fig. 6-18b. The presence of MDWs also appears to be present in the micrograph of the kinks. Around the kinked regions voids caused by delamination and layers spreading apart to accommodate the kink were observed. These observations are consistent with those made by Molina et al. [82], in which cross sectional TEM micrographs revealed the presence of MDWs, kink bands and delamination after NI on Ti_3SiC_2(0001) thin films.

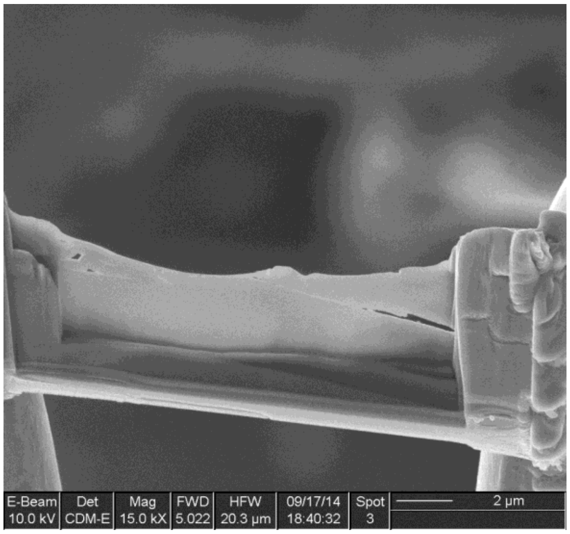

Figure 6-17. TEM sample of indent B5, which was made near a grain the boundary of a (0001) and adjacent grains. A crack is seen in the image, which resulted from the two grain boundaries pushing apart.

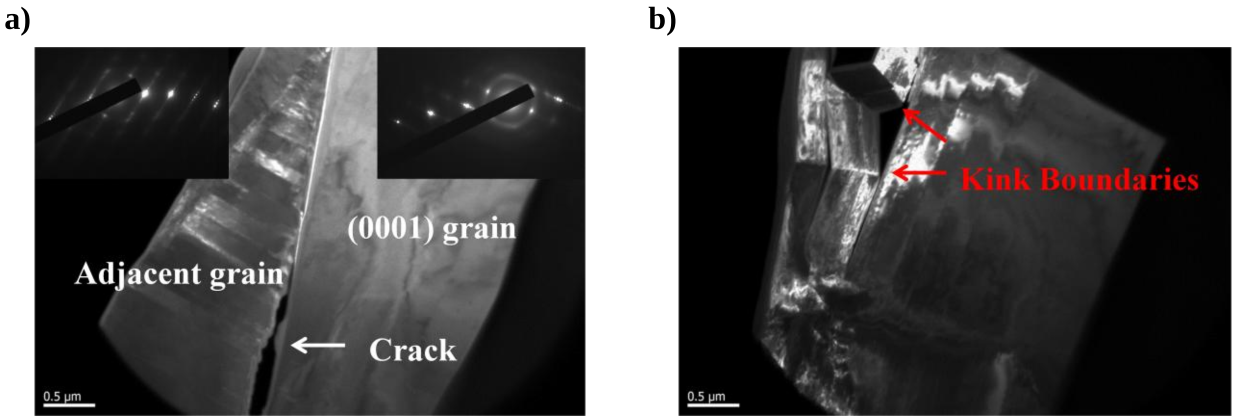

Figure 6-18. Darkfield images of indent B5 showing, a) crack at the grain boundary with diffraction patterns above the crack (top left inset) and below the crack (top right inset), and b) kinks that formed at the edge of the indent. The bright regions within the kink are evidence for c-axis strain.

Finally, a cross section of indent F2, which was loaded to 500 mN for 50 cycles on the $(10\bar{1}0)$ plane, is shown in Fig. 6-19. In the FIB-SEM image, some cracks and voids could be resolved very faintly. Indentation on the prismatic plane at such a high stress resulted in the creation of a number of grains of different orientations beneath the indented region that appear in contrast in Fig. 6-20a-b. Here again, delamination cracks (see Fig. 6-20c) and kinks were observed (Fig. 6-20d).

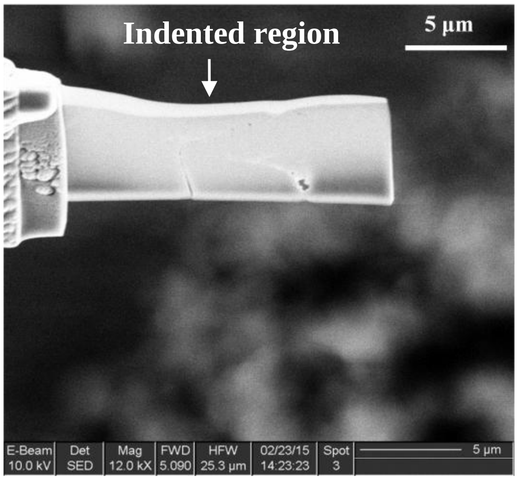

Figure 6-19. TEM sample of indent F2, which was made on the $(10\bar{1}0)$ plane using a 21 µm tip and a maximum load of 500 mN for 50 cycles. Cracks were observed beneath the indentation.

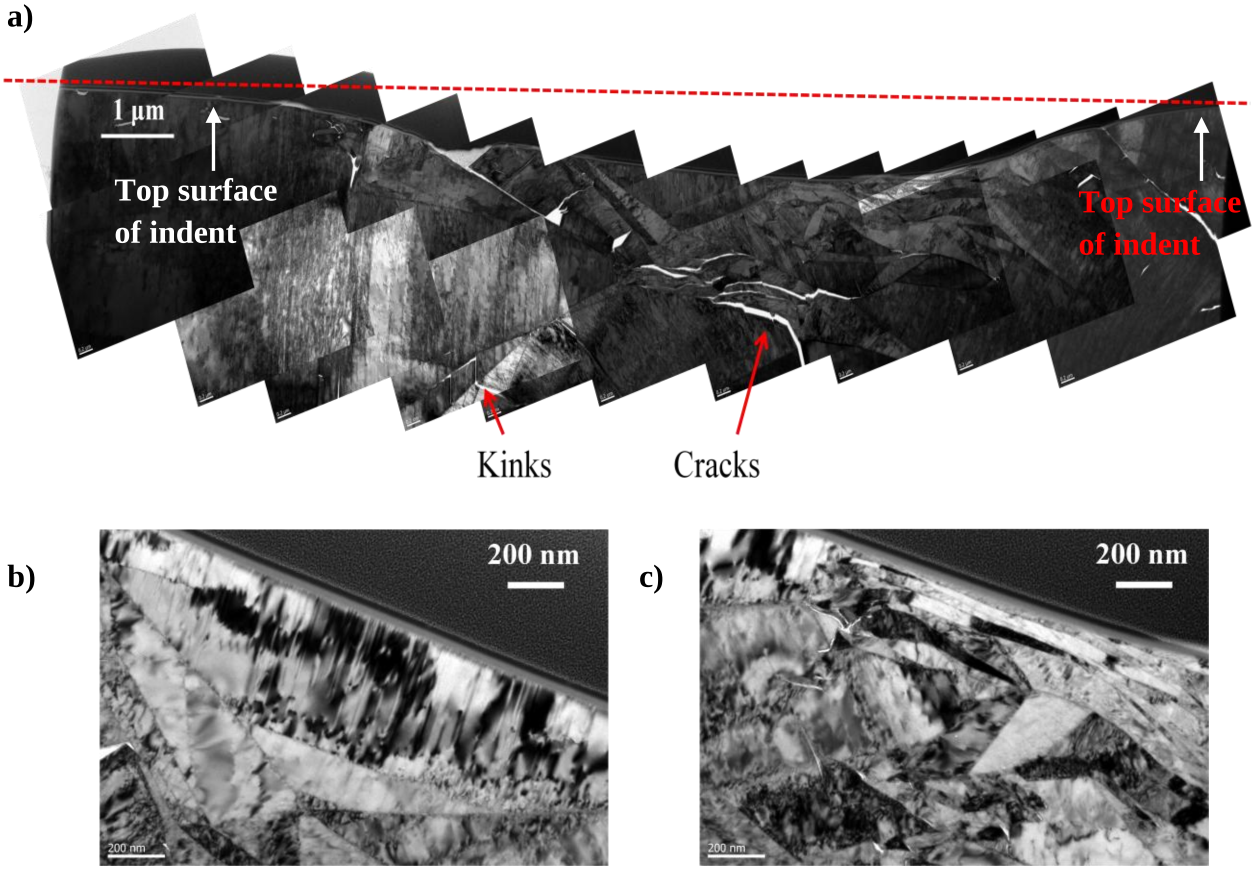

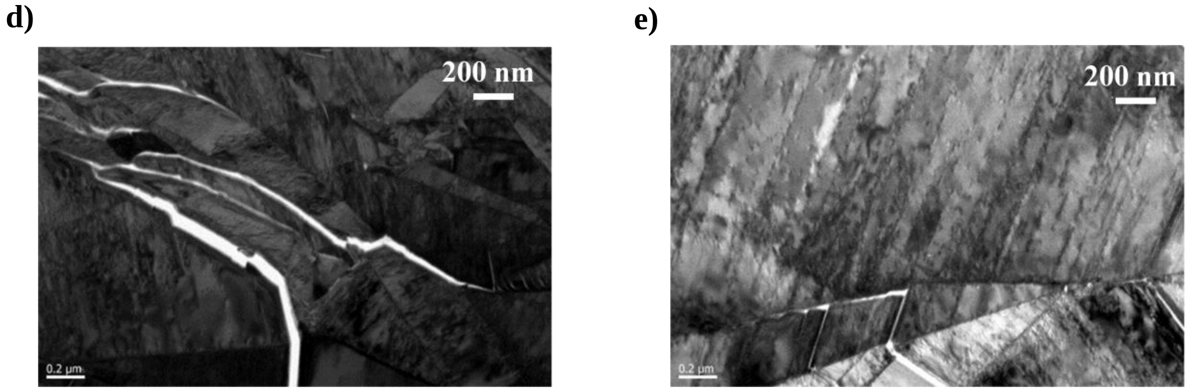

Figure 6-20. a) Collage of TEM micrographs of indent F2 – which was made on the $(10\bar{1}0)$ plane using 21 μm tip. Various cracks, kinks and grains appear in the collaged image. The red dotted line represents the material height around the indentation crater. b-c) Brighfield images beneath indent showing different grains in contrast. d) Magnified images of cracks and voids are shown as well as e) magnified images of kinks at different areas beneath the indent.

6.4 Discussion

Based on the results presented thus far in this study, it is clear that reversible hysteresis loops can be present in the indentation stress vs. a/R curves, in the absence of a definite kink boundary (see Fig. 6-10a), and/or when cracking and delamination are present (Fig. 6-10b, Fig. 6-11c). More importantly, loops can be present without any noticeable indentation marks or permanent damage, consistent with previous NI studies on Ti_3SiC_2 [23]. When indentations were made on the (0001) plane using a 21 μm (indent B6, for example), the nested loops were larger than the loops that resulted from using a 100 μm tip. Fig. 6-7a shows a plot of $\Delta a_B/a_o$ vs. σ^2 for two indentations made with both sized tips, and it is clear that σ^2 is significantly larger at a given value of $\Delta a_B/a_o$ when the 21 μm tip was used. The same is true when comparing $\Delta a_B/a_o$ vs. W_d. Comparing results from both the (0001) and the $(10\bar{1}0)$ orientations using a 100 μm tip shows that σ^2 (see Fig. 6-7a) and W_d (see Fig. 6-7b) are slightly larger for indentations made on the (0001) plane than the $(10\bar{1}0)$ plane.

The shape of the loops offers a signature when cracking may be present and contributes to the mechanical response in the initial stages of loading. For example, in Figs. 6-10b and 6-11c, upon *initial* loading, the material appears to be soft until reaching a threshold a/R value, at which point the material gives a stiffer response to the applied stress. This initial loading segment is most likely due to the cracks being pushed together, after which the material registers the expected response to mechanical loading. The question that remains to answer is, what causes the energy dissipation, W_d? Before discussing a few possibilities in the following section, the ideas by Jones et al. [88] will be discussed in detail and considered.

In the study by Jones et al. [88], a couple of experiments were preformed: i.) ex-situ and in-situ cyclic compression tests using X-ray diffraction were performed on polycrystalline Ti_3SiC_2 bars with a non-random bimodal grain structure; ii.) cyclic nanoindentation tests were performed on TiC(001) and Ti_3SiC_2(0001) single crystal films, and TiC(111)/Ti_3SiC_2(0001) multilayers, with each grown on Al_2O_3 substrates, and also performed on MgO(001). In-situ X-ray diffraction experiments, the beam was configured in the transmission geometry and diffraction images were gather throughout loading cycles. Samples were subjected to 5 cycles to a peak stress of 460 MPa and the strain on the lattice planes was evaluated with a strain resolution 2×10^{-5}. Nanoindentation tests used a Berkovich tip and cross sections of indents were examined in the TEM. Elastoplastic Self-Consistent (ESPC) modeling was used to simulate macroscopic stress-strain behavior in which each grain treated as being embedded in a homogeneous medium with properties of the aggregate, but each grain having single-crystal elastic and plastic properties.

Results on polycrystalline Ti_3SiC_2 showed a small amount of residual strain was observed after the first loading cycle, and fully reversible behavior was observed during subsequent cycles. In-situ X-ray experiments showed that lattice strains, which varied in magnitude and sign between families of grains, developed and remained approximately constant with further cycling. The intuition was described in a similar manner as the Bauschinger effect between hard and soft grains. ESPC modeling predicted residual strain and that for hysteresis to occur, the sample must be loaded to a minimum stress whose magnitude was approximately twice that of compressive the yield stress. EPSC calculations of W_d were reported as being consistent with experiments for uniaxial stress in between 10 – 75 MPa in which W_d scaled with σ. Depending on the range of stresses, $W_d \sim \sigma^n$, where $n \approx 1$ at max stresses much greater than the yield stress on the basal slip system. The evolution of elastic strains was measured from reflections of planes during the 1st loading/unloading cycle, in which plasticity theory predicts that all grains deform first elastically until the yield stress for the soft grains has been achieved. The increasing load is then borne by hard grains. In Ti_3SiC_2, where there are fewer than 5 independent slip systems, plastic flow must be accompanied by elastic strain. It was elastic strains built up in the hard grains during loading that were sufficient to drive reversible plastic flow in the soft grains during unloading was the concluded as giving rise to hysteresis.

Under indentation, dislocation motion in Ti_3SiC_2 was noted as being able to slip only on the basal plane, which gives an insufficient number of slip systems to accommodate plastic flow beneath an indenter, and thus a buildup of elastic strains. In this case, reversible hysteresis was associated with relaxation of the elastic strains in a material with an insufficient number of slip systems. The idea of kinking playing a role in the reversible hysteresis effect was investigated with comparisons between single crystal Ti_3SiC_2 thin films and multilayers in which TiC replaced some Ti_3SiC_2. Reversible hysteresis was observed in both the single crystal and the multilayer cases, and TEM micrographs showed kinks beneath Ti_3SiC_2, but no kink band beneath TiC/Ti_3SiC_2, suggesting that kinking is not required for hysteresis.

The idea that reversible hysteresis was the result of elastic strains built up due to plastic anisotropy instead of kinking was investigated on MgO as well. Reversible hysteresis loops were observed under cyclic nanoindentation with an absence of kink bands. Due to the ionic bonding and cubic crystal structure of MgO, the soft slip systems intersect, increasing the possibility of dislocation entanglement in MgO. It was suggested that reversible dislocation motion would be harder in MgO than in the MAX phases for this reason. Both MgO and the MAX phases are plastically anisotropic, in which it was concluded that hysteresis may occur in single crystal indentation as a result of sufficient plastic anisotropy and an insufficient number of soft slip systems to accommodate deformation around the indentation.

The work by Jones et al. [88] merits some attention as a possible explanation to the reversible hysteresis effect. However, there are a few things that must be pointed out in their work that is of concern. First, EPSC modeling was used to predict stress-strain behavior for samples used in their work. EPSC modeling is based on a homogeneous inclusion method in which the mechanical response of grains surrounding each individual grain is homogenized. This warrants a limitation in their study since each individual grain is governed by its orientation relative to the applied load and by the orientation of neighboring grains. Thus, incompatibility stresses result due to plastic anisotropy. Secondly, while they suggest that reversible hysteresis underneath an indenter is a result of residual lattice strain due to a limited number of slip systems, no model was provided in this case as to directly compare results in my study to their predictions for validation. In the following section, a few possibilities are discussed to help explain results in this study.

6.4.1 Dislocation bowing

Using the same model discussed in Ch. 4 for dislocations bowing in a network, calculations were performed to see how well the model fits observations made on Ti_3SiC_2. As mentioned in previously, due to the high c/a ratio of MAX phases, non-basal dislocations and twins are unlikely to exist. Also, while KBs were not observed at location B6, calculations assuming KBs are present (but faint or diffuse) were made. Using this location specifically where KBs were not present in the calculation would help to give an idea to what extent dislocation bowing could be used to explain the hysteresis effect. This location is the most reliable since the contact radius, a_o, and the total depth were measurable in the AFM.

If GNDs bowing out in the form of LAKBs through SSDs is assumed to be responsible for W_d, the shear strain, $\gamma_{B,}$ due to dislocations bowing in a network can be determined using Eq. 4-4. Since the LAKB was assumed to be faint or diffuse in Ti_3SiC_2 at this particular location, the angle between the LAKB and the matrix could not be measured in the TEM. Instead, as in the case with Zn, the angle between the indenter and sample surface was used, which is an approximate to the angle between the LAKB and the matrix for small angles. This angle was calculated using $\theta = \tan^{-1}(\frac{h}{a_0})$, where h is the displacement into the surface ≈ 170 nm and $a_o \approx 3.5$ μm is the contact radius, both measured in the AFM. The value for θ was calculated to be $\theta \approx 2.8°$. Given that in this case Δa_B was determined to be ≈1.2 μm - at a stress of 6.13 GPa (Fig. 6-10a), it follows that according to Eq. 4-4, $\gamma_B \approx 0.046$ at location B6.

Assuming a Burger's vector, $\mathbf{b}$ = 3.06 Å and that the KBs extend to a depth of $2a_o$ into the material in the form of a cylinder, the GND density was estimated using Eq. 4-2 to be approximately $9.06\text{x}10^{13}$ m^{-2} at location B6, loaded to 500 mN for 50 cycles on the (0001) plane and using a 21 μm tip. Since GNDs must form in equal pairs with dislocation beneath the indent, this approach provides a method to approximate the minimum dislocation density beneath the indent.

Similar calculations were done at other locations, such as at A4 and E4. Since these indents were below the resolution limit of the SEM and no AFM data was available at these locations, a_o was taken as the contact radius from NI data after the 10th cycle, as mentioned above. Starting with A4, this value was determined to be ≈4.7 μm. The total displacement, *h*, was taken as the displacement upon minimum loading during the 10th cycle, which was ~ 119 nm. The value for θ was calculated to be $\theta \approx 1.45°$. Given that in this case Δa_B was determined to be ≈ 2.2 μm - at a stress of 2.89 GPa (Fig. 6-6b), it follows that according to Eq. 4-4, $\gamma_B \approx 0.011$ at location A4.

Now considering E4, $a_o \approx 3.5$ μm, $h \approx 67$ nm, this was taken after 10 cycles. The value for θ was calculated to be $\theta \approx 1.1°$. In this case Δa_B was determined to be ≈2.2 μm - at a stress of 2.87 GPa (Fig. 6-6a), it follows that according to Eq. 4-4, $\gamma_B \approx 0.011$ at location E4. These values are very much the same as those at location A4. The GNDs calculated were $7.5\text{x}10^{13}$ m^{-2} and $5.7\text{x}10^{13}$ m^{-2} at locations A4 and E4, respectively.

Now to focus on W_d, which is equal to $2\tau_f\gamma_B$ [56]. In Ch. 4 it was shown that $W_d = 2\Omega\sigma_f\theta(\Delta a_B/a_o)$, (Eq. 4-5) where the factor of 2 accounts for the energy dissipated during loading and unloading, and τ_f the frictional shear stress that resists bowing. A plot of W_d vs. $\Delta a_B/a_o$ (Fig. 6-7b) was generated at location B6, which yielded a straight line with a slope $\approx 2\Omega\theta\sigma_{y.}$ Using the slope from the W_d vs. $\Delta a_B/a_o$ and σ_y at location B6 (1.7 GPa), Ω was calculated to be ≈ 0.54. Although this value is unphysical since it is higher than the maximum possible value of Ω, which is 0.5, it is reasonable. At locations A4 and E4, Ω was calculated to be ≈ 1.11 and 1.69 respectively. These values are unphysical. However, given the many crude approximation made to derive Eq. 4-5, this result is gratifying in that Ω is of the order of unity – with no adjustable parameters - which is the most important conclusion. Note that it is possible with the various assumptions made in deriving Eq. 4-5, to reduce the values of Ω to reasonable numbers, but that would not shed more light on the problem. What is important here is that Ω is of the order of unity as expected.

Assuming dislocations are bowing out, the fact that $\Delta a_B/a_o$ scaled as σ^2 (Fig. 6-7a) in this work on Ti_3SiC_2 can be attributed to the fact that both the area swept by the ith dislocation in a mosaic block of volume V, A_i, and the number of dislocations which bow per mosaic block, n are linear functions of σ (see Eq. 4-3). Following Lucke and Granato's [75] rigid rod model, and applying Eq. 4-6, with $y \approx \Delta a_B$, and assuming $\alpha \approx 0.5$ and $\Omega \approx 0.54$, then L_N is estimated to be of the order of 0.3 μm at location B6. Assuming this value for L_N, the normal stresses needed to bow dislocations to a radius 0.3 μm, was calculated using Eq. 4-8 to be $\sigma \approx 127.5$ MPa. These values are roughly an *order of magnitude* lower than the measured yield stress at location B6, which was ≈ 1.7 GPa. The reason for this discrepancy most likely because basal dislocations are not what is dissipating the energy but ripplocations (See below).

Similar calculations at locations A4 and E4 reveal L_N to be ≈ 0.5 and 0.2 μm respectively, assuming $\alpha \approx 0.5$ and $\Omega \approx 1.1$ and 1.69 at locations A4 and E4. Assuming these values for L_N, the normal stresses needed to bow dislocations to radii 0.5 μm and 0.2 μm are $\sigma \approx$ 36 and 53.6 MPa, respectively.

The result of calculations at a location where KBs were not observed but assumed provides a reasonable explanation that dislocation bowing as a possibility for the reversible hysteresis loops. However, there are some concerns worthy of consideration. First, given that only basal dislocations are believed to exist in Ti_3SiC_2, it is not possible to explain c-axis strain (see Fig. 6-14), as was observed at location B6. Secondly, since non-basal dislocations do not exist in the MAX phases, it is impossible to explain the strain normal to the basal planes that results in the delamination cracks observed when the indenter is indented into the $(10\bar{1}0)$ plane (Fig. 6-3b). Furthermore, since the shear stress on the basal planes is ≈ 0, the dislocation bowing model cannot be applied to indentations on the $(10\bar{1}0)$ plane. Yet, reversible loops are observed up to ~ 3 GPa (see Fig. 6-6a) when loading was applied on $(10\bar{1}0)$ plane using a 100 μm tip. Some were also observed when the indenter radius was 21 μm (Fig. 6.10b). To explain these observations, we propose that the operative micromechanism is the formation of ripplocations.

6.4.2 Evidence of ripplocations in Ti_3SiC_2

Very recently, Kushima et al. [22] postulated the existence of a new defect in 2D layered van der Waal solids termed ripplocations. Introduced in Ch. 2, Fig. 2-7 shows a schematic of a ripplocation. Kushima et al. [22] defined a ripplocation as being a local line of ripple created by an excessive line of atoms that are locally inserted into one layer relative to the other, thereby creating a local line of ripple in the van der Waal homostructure that combines the effects of dislocations and surface ripples. Ripplocations – as mentioned in Ch. 2, are topologically equivalent, but energetically distinct from dislocations, are localized with core width on the order of a few nanometers, with same-sign ripplocations interacting attractively (see Fig. 2-7b) as they merge at close distances. This last piece of information, of course is different from dislocations in which same sign dislocations repel at close distances. Bonds are not broken when ripplocations form, and one of the many ways ripplocations can form includes formation due to mechanical loading. It is important to note that the work of Kushima et al. [22] was confined to van der Waals solids and all the evidence presented was for surface ripplocations.

Inspired by the work of Kushima et al. [22], we started looking for ripplocations under the indentations made in Ti_3SiC_2. The most intriguing result that was inexplicable in the classic formalism of dislocations is the clear evidence for c-lattice strain under the indenter. The best evidence for c-axis strain in Ti_3SiC_2 is shown in Fig. 6-14. Under the appropriate imaging conditions in the TEM, defects which possessed a c-component strain appeared in contrast – adding to the mystery of the defect type. Fig. 6-15b shows the Bragg filtered image of the region around of what is believed to be a ripplocation, which shows some bending of the atomic planes. Clearly the evidence shown here indicates that ripplocations are not only surface defects but exist in bulk and more importantly that they apply to layered solids in general, and not just van der Waals solids.

The temporary pile up of ripplocations under an indenter and their possible reversible migration when the load is removed may be the cause for W_d in the Ti_3SiC_2 phase, especially when indenting on the $(10\bar{1}0)$ plane, where as noted above, the dislocations bowing model was not applicable. Ripplocations may be pushed parallel to the basal planes into the bulk material during loading (see Fig. 6-21) on the $(10\bar{1}0)$ plane, and return when the load is removed. This is reasonable since residual marks were typically not present or below our detectability limit - when indentations that resulted in reversible loops were made on the $(10\bar{1}0)$ plane (see Fig. 6-6a). Under higher stresses, ripplocations may merge, grow and finally lead to delamination, cracks and therefore observable damage. This process is illustrated in the schematic in Fig. 6-21. It is possible that ripplocations may lead to kink band formation on the (0001) plane when merging ripplocations again can lead to delamination and kinking. Figure 6-22 is a schematic illustrating the process of ripplocations (present in multiple atomic layers of Ti_3SiC_2) migrating and merging to form a kink when a sufficient load is applied normal to the (0001) planes. The atomic planes must separate (as seen in Fig. 6-18b) when a kink forms after ripplocations have merged.

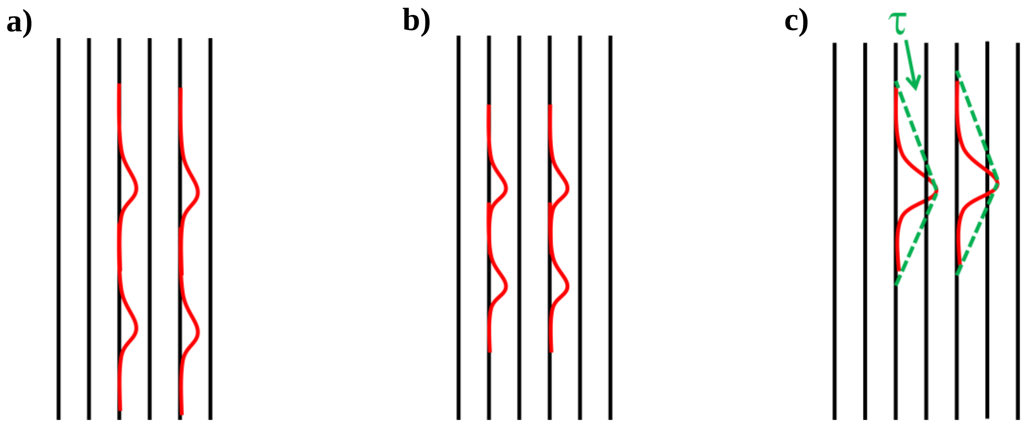

Figure 6-21. Schematic of ripplocations (red lines) beneath Ti_3SiC_2 on the $(10\bar{1}0)$ plane under a) no applied load, b) loading and c) under applied load sufficient for ripplocations to merge. When loading without merging, the ripplocations migrate back, resulting in W_d. Once the merging barrier is overcome, planes delaminate and crack.

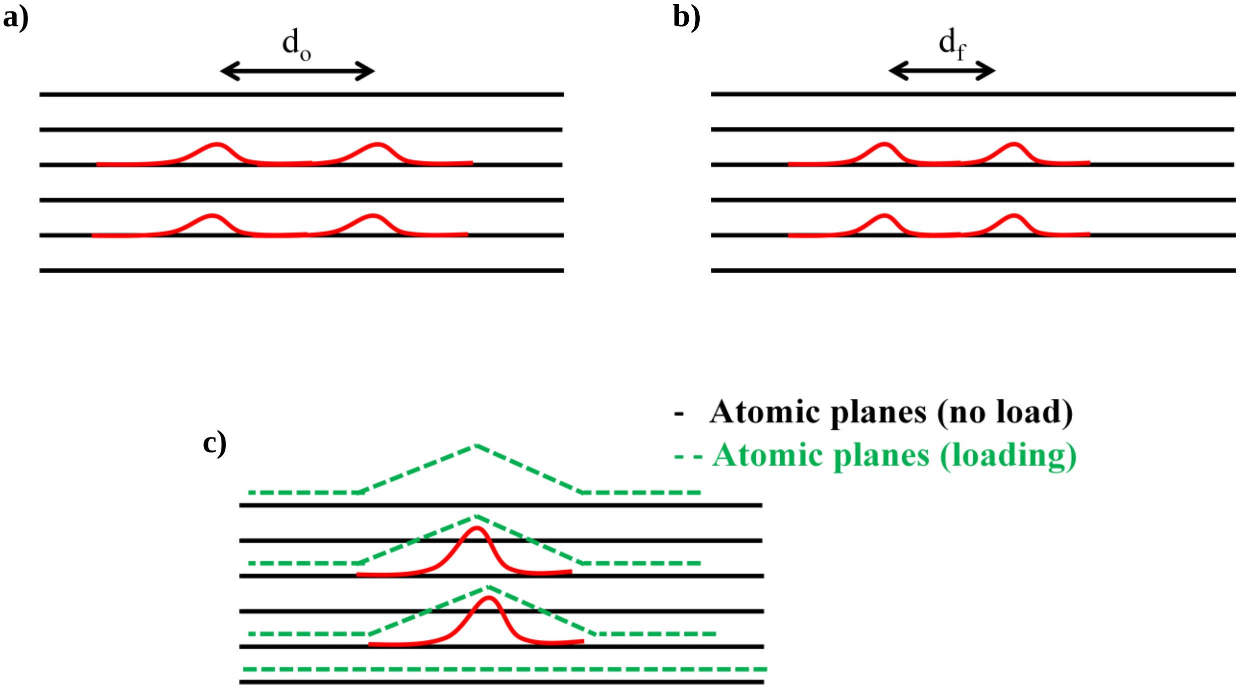

Figure 6-22. Schematic of ripplocations beneath Ti_3SiC_2 on the (0001) plane. a) Ripplocations (red lines) with no load applied spaced a distance d_o apart. b) Ripplocations migrated towards one another under applied load to a distance d_f apart, without merging. c) Merged ripplocations align on parallel planes to form a kink boundary (green dotted line) after delamination.

6.4.3 Damage and hysteresis loops

The effect of damage in the form of cracks and delamination has been shown to change mechanical response of the material under an applied load and W_d, as shown in Figs. 6-10b and 6-11c. Hysteresis loops resulting after the initiation of damage are discernible from those produced when the material was not cracked. Cracks formed at some locations (see Fig. 6-3b) and not at others (see Fig. 6-3a) when loading was applied on the (0001) plane under similar stresses. This may be the result of ripplocations combining and leading to cracking and delamination at one location, but not the other. It is unclear whether or not ripplocations are pre-existing defects; however, according to Kushima et al. [22], ripplocations may form during thermal processes. Thus, if ripplocations do indeed pre-exist, then a higher density may have been present at the location where cracks formed. It is quite possible that this higher density may lead to merging more easily, which can lead to stresses normal to the basal planes (when loading parallel to the basal planes), and thus cracking and delamination, as illustrated schematically in Fig. 6-22.

The presence of other subsurface defects may be one other possibility since such defects serve as obstacles and become points of local stress concentrations. Indenting on the $(10\bar{1}0)$ plane resulted in cracks and damage most likely from the delamination of parallel planes and stress concentrations at subgrain boundaries. Since the material has been damaged instead of simply deformed, the hysteresis loops are not regarded in this study in the same context as reversible plastic deformation.

6.5 Summary

The reversible hysteresis effect of Ti_3SiC_2 was investigated under cyclic nanoindentation on the (0001) and $(10\bar{1}1)$ planes using 21 and 100 μm spherical tips. Fully and spontaneously reversible hysteresis loops were observed in the indentation stress vs. a/R curves in both orientations. This effect may be partly the result of dislocations bowing out, but dislocations alone does not explain all of the observations made in this study. A new deformation mechanism called ripplocations – which combines features of edge dislocations in bulk solids with surface ripples in 2D materials – has been used here to better explain the observations made in this study. Experimental evidence presented herein supports the existence of ripplocations in a bulk solid – for the first time. More detailed analysis and work is certainly needed to better model the reversible hysteresis effect using ripplocations in bulk. The hysteresis loops in the indentation stress vs. a/R curves has a unique signature - in that the curves are initially convex and the cracks faces are being pushed together - when damage such as cracking has occurs. This signature enables the distinction between deformation and failure modes.

CHAPTER 7: COMPARATIVE ANALYSIS

7.1 Introduction

At this juncture in the study, the origins of the reversible hysteresis loops in the indentation stress vs. a/R curves on Mg, Zn and Ti_3SiC_2 has been attributed to bowing of dislocations in LAKBs, twin expansion/contraction, and the possibility of ripplocations in the MAX phases. Although microcracking was not considered to be the origin of the hysteresis loops in this study, other studies [86, 87] reported in literature have suggested that microcracking is responsible for the reversible hysteresis effect. In this study, whenever cracks were observed, the hysteresis loops were distinguished by a unique signature – in which the stress upon loading in any given loop was significantly lower initially than any known mechanical response (see Fig. 6-10b), followed by a response by stiffer material. This effect was due to cracks pushing together underneath the indenter, and therefore was not considered further. Cracks are also considered a mode of failure and not deformation. Also worth noting was the fact that reversible loops were observed in metals, that do not microcrack even after 25 or 50 cycles. Thus, if microcracking contributes anything to the reversible effect, their effect is small.

The nested indentation stress vs. a/R curves can be separated by regime for more careful analysis – a linear elastic regime and a non-linear regime. Depending on the active deformation modes in the most general case, the total non-linear regime, $(\frac{a}{R})_{NL}$, of the reversible hysteresis loops in the indentation stress vs. a/R curves can be expressed as

$$(\frac{a}{R})_{NL} = (\frac{a}{R})_{B} + (\frac{a}{R})_{Twin} + (\frac{a}{R})_{DP} + (\frac{a}{R})_{MC} + (\frac{a}{R})_{Rip}, \qquad (7\text{-}1)$$

where the quantities on the right hand side of Eq. 7-1 represent the non-linear contribution to the total a/R resulting, respectively, to the bowing of dislocations in LAKBs, twin motion, dislocation pile ups, microcracking and ripplocations, respectively.

Equation 7-1 provides a general and all encompassing sum of all currently known possible contributions to the reversible hysteresis effect that were either observed in this study or reported in the literature. If a deformation (or failure) mode is not active, then its contribution to the total non-linear regime is zero. As an example, in the case with Zn and the MAX phases, twins were not observed, and therefore cannot contribute to the reversible hysteresis loops observed in the indentation stress vs. a/R curves. To further investigate the origins of the reversible hysteresis loops, it suffices to make comparisons between the materials used in this study.

7.2 Comparisons of NI on Mg, Zn and Ti_3SiC_2

To compare the indentation stress vs. a/R results between the various materials, the indentation stress was normalized by the shear modulus, and a plot of σ/G vs. a/R for a select nested sequence on each material on the (0001) orientation was generated as shown in Fig. 7-1a. This normalization eliminates the bond strengths of the various materials as a factor and allow for a fair comparison. It was not possible to *directly* compare the size of the loops for Ti_3SiC_2 with Mg and Zn at the same or similar a/R values. Using a 100 μm tip on Ti_3SiC_2 to the maximum load of the nanoindenter (550 mN) resulted in a/R ~ 0.04, while values of a/R for Mg and Zn were around 0.11 and 0.12 respectively (see Fig. 7-1a). A higher stress values, and thus higher a/R, was only feasible on Ti_3SiC_2 when a smaller tip, 21 μm, was used, which resulted in a/R values ~ 0.165. Not surprisingly, the loops were significantly larger when using a 21 μm tip as compared to the 100 μm on Ti_3SiC_2, as shown in Fig. 7-1b. The size of the loops, W_d^*, can be calculated in the same manner that W_d was calculated (see Ch. 3). Note by normalizing by G,

W_d^* is unit less. By assuming an a/R value for Ti_3SiC_2 similar to that of Mg or Zn, then the size of the loop at that value, $W_{d(x)}^*$, would be

$$W_{d(0.04)}^* < W_{d(x)}^* < W_{d(0.165)}^* \tag{7-2}$$

where x represents a/R values such that $0.04 < x < 0.165$. Using this assumption and the observations that at similar a/R values for Mg and Zn,

$$W_d^*(Zn) < W_d^*(Mg) < W_{d(0.04)}^*(Ti_3SiC_2), \tag{7.3}$$

it can be deduced that the loops are larger at a given a/R for Ti_3SiC_2. For example, if an a/R is achieved on Ti_3SiC_2 that is identical to that of Mg and Zn, say a/R = 0.11, then W_d^* for Ti_3SiC_2 is significantly larger at the same value for a/R – assuming the trajectory of the loop sizes in Ti_3SiC_2 continues to sizes observed in Fig. 7-1b. Notice, that at the same stress, the loop sizes seem more or less the same between the different materials.

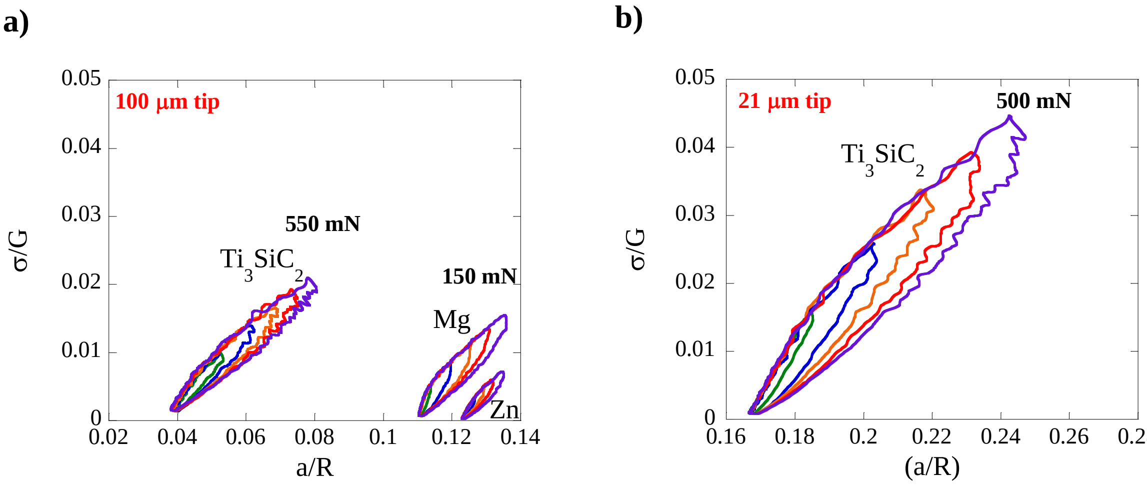

Figure 7-1. The indenation stresses were normalized by the shear modulus, G, for each material and plotted against a/R. a) Each nested sequence resulted from indentation on (0001) using a 100 μm tip with the largest loops resulting from Ti_3SiC_2, followed by Mg and then Zn. b) A single plot of σ/G vs. a/R is shown when using a 21 μm tip on Ti_3SiC_2 to a maximum load of 500 mN. The overall loop sizes were larger for higher values of a/R.

Before explaining the possibilities, some observations to note are that indent craters were present in the cases of Mg (see Ch. 4) and Zn (see Ch. 5), while no visible damage was observed when using a 100 μm tip on Ti_3SiC_2. Using the 21 μm indenter, on the other hand, resulted in an indention crater, but no clearly discernible KBs were found in post-indentation TEM micrographs, despite clear evidence of energy dissipation (Fig. 7-1b).

When KBs did form on Ti_3SiC_2 using the 21 μm indenter, they were accompanied with delamination cracks, which produced a different signature in the indentation stress vs. a/R curves altogether (Fig. 6-10a and 6-11c). Both Mg and Zn can accommodate some c-axis strain with <c + a> dislocations, while Ti_3SiC_2 does not possess non-basal dislocations and the latter is not an option. When combined with the fact that twins also do not exist in these materials, the question of how the c-axis strain is accommodated does not have easy answers.

It follows that the idea of the possible nucleation and migration of ripplocations in the MAX phase contributing to the hysteresis effect must be considered despite the little we know about the latter. The best evidence for the existence of ripplocations in a bulk layered solid was presented in Ch. 6 at the location whose data is shown in Fig. 7-1b. In Fig. 7-1b, the loops for Ti_3SiC_2 are significantly larger than for the other materials in Fig. 7-1a. Assuming loops can be generated on Ti_3SiC_2 at comparable values of a/R to those of Mg and Zn, W_d^* is expected to be larger in Ti_3SiC_2 at the same a/R, which would suggest that ripplocations dissipate may dissipate more energy than dislocations. The confined buckling of atomic layers may contribute to this effect if ripplocations are indeed nucleated beneath the indent.

In a similar manner that the shape of the hysteresis loops in the indentation stress vs. a/R curves were signatures of the phenomena observed, the energy dissipation at a given a/R may also be an indicator or a type of a signature of different mechanisms that contribute to the reversible hysteresis effect.

The size of the loops in Fig. 7-1a were calculated (see Ch. 3), and $W_d^*$was plotted against $\Delta a_{B/}a_o$ (Fig. 7-2a) and $(\sigma/G)^2$ (Fig. 7-2b). As mentioned previously, W_d^* is unit less since the indentation stress was normalized by the shear modulus for each material. This was done, as mentioned above, to provide a more fair comparison of the loops between the different materials. In Fig. 7-2a, the values for $R^2 > 0.96$ for Ti_3SiC_2, and > 0.98 and 0.99 for Zn and Mg respectively. The values for R^2 in Fig. 7-2b are > 0.96 for Ti_3SiC_2, and > 0.99 for Zn and Mg respectively. Lastly, $R^2 > 0.99$ for each material in 7-2c. These values show a very reasonable fit to a line. The interesting thing to note in these figures is that W_d^* is slightly larger for Ti_3SiC_2 when plotted against $\Delta a_B/a_o$, while there is not much variation when plotted against $(\sigma/G)^2$. In fact, Fig. 7-2c shows no variation whatsoever when W_d^* is plotted against $(\sigma - \sigma_Y)^2/G^2$. These results are consistent with the above discussion in which W_d^* in Fig. 7-1a varied with values of a/R, but were more or less the same at a given stress. Thus, in absence of bond strength, results based on $\Delta a_{B/}a_o$ or a/R are most useful in analysis.

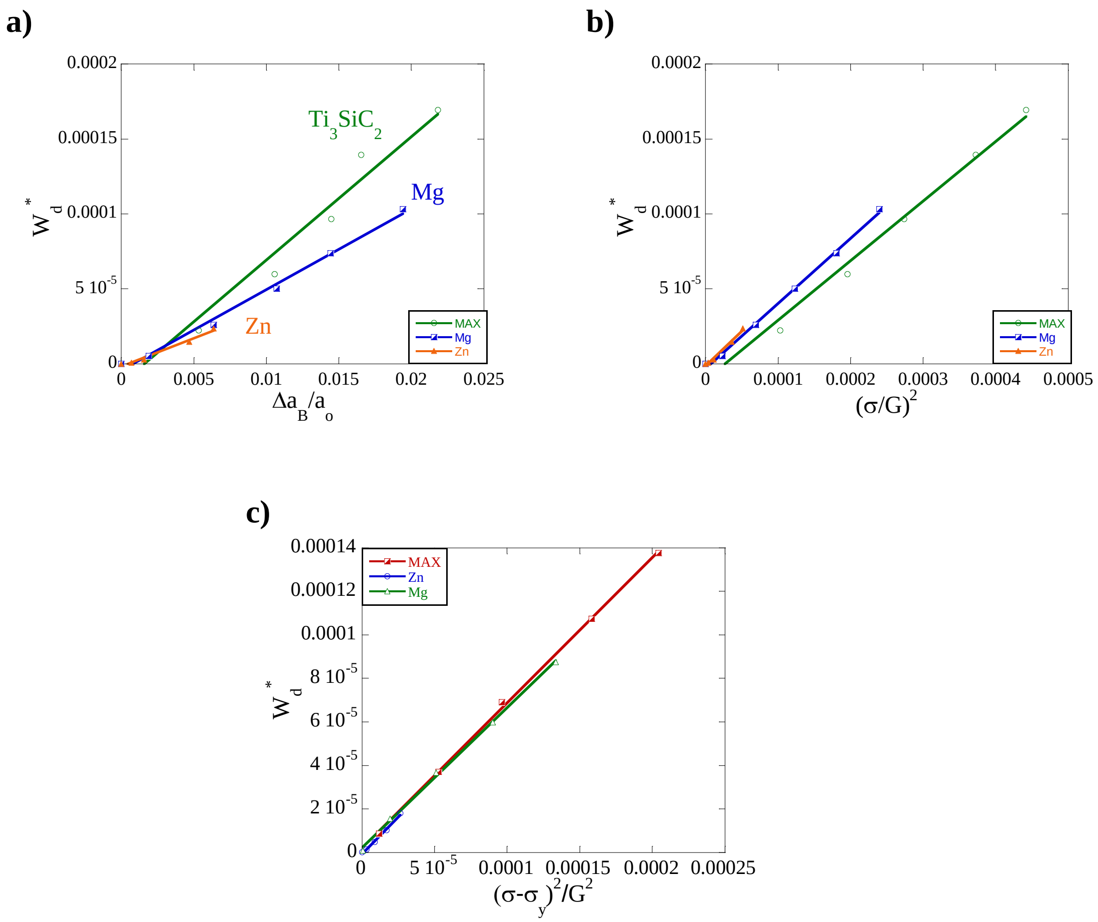

Figure 7-2. Plot of, a) W_d^* vs. $\Delta a_B/a_o$ and, b) W_d^* vs $(\sigma/G)^2$ for indentations on the (0001) plane of Mg, Zn and Ti_3SiC_2, loaded 50 times at each location and using 21 μm tip for Ti_3SiC_2. Note W_d^* does not have units in this plot since $\Delta a_B/a_o$ was calculated from the plots that were normalized by G. Based on plot (a), more energy is dissipated when comparing the variation as a function of $\Delta a_B/a_o$. Little variation exists in plot (b) however, which is expected since area of the normalized loops did not vary from material to material at a given stress in 7-1a. c) Plot of W_d^* vs. $(\sigma - \sigma_Y)^2 / G^2$ shows no variation between the different materials.

Since W_d^* is related to σ/G, and scales linearly with $(\sigma/G)^2$, and $\sigma^2 \sim W_d$, it must follow that $W_d^* \sim W_d/G^2$. Considering this relation, it is possible to use values of W_d^* to make a correlation to the energy dissipation for each material. For any two materials, A and B, if

$$W_d^*(A) < W_d^*(B) \tag{7-4}$$

it follows that

$$\frac{W_d(A)}{G_A^2} < \frac{W_d(B)}{G_B^2}\,. \tag{7-5}$$

Hence, apply Eqs. 7-4 and 7-5 to Eq. 7-3 yields

$$\frac{W_d(Zn)}{G_{Zn}^2} < \frac{W_d(Mg)}{G_{Mg}^2} < \frac{W_d(Ti_3SiC_2)}{G_{Ti_3SiC_2}^2} \quad (7\text{-}6)$$

Given that G_{Zn} = 43 GPa, G_{Mg} = 17 GPa and $G_{Ti3SiC2}$ = 139 GPa, the highest energy dissipation occurs in Ti_3SiC_2. This is an important result that indirectly confirms that the energy dissipating mechanism in the MAX phase is different than that in Mg or Zn. Said otherwise, these results support the idea of ripplocations. It follows that if ripplocations are indeed the mechanism responsible for W_d beneath Ti_3SiC_2, then for a given strain, it is obvious that ripplocations significantly dissipate more energy than dislocations.

While the results in this study on Ti_3SiC_2 were explained using ripplocations, the ideas by Jones et al. [88] still must be considered in comparison. In their study, reversible loops were the result of residual lattice strains due to limited slip systems. It was noted that W_d scaled with σ in between 10 – 75 MPa consistent with EPSC calculations of W_d, and depending on the range of stresses, W_d was also noted as scaling with σ^n, where $n \approx 1$ at max stresses much greater than the yield stress on the basal slip system. Note that these results were predicted on polycrystalline Ti_3SiC_2. Although the stresses in this study were out of the range given by Jones et al. [88], W_d was plotted against σ (see Fig. 7-3a) and σ^2 (see Fig. 7-3b) to compare the results in their predictions with results in this study. Values for R^2 indicate W_d vs. σ^2 was the better fit to a line when comparing the two plots. The lack of a direct comparison between Jones et al.'s [88] prediction to results in this study is a major limitation.

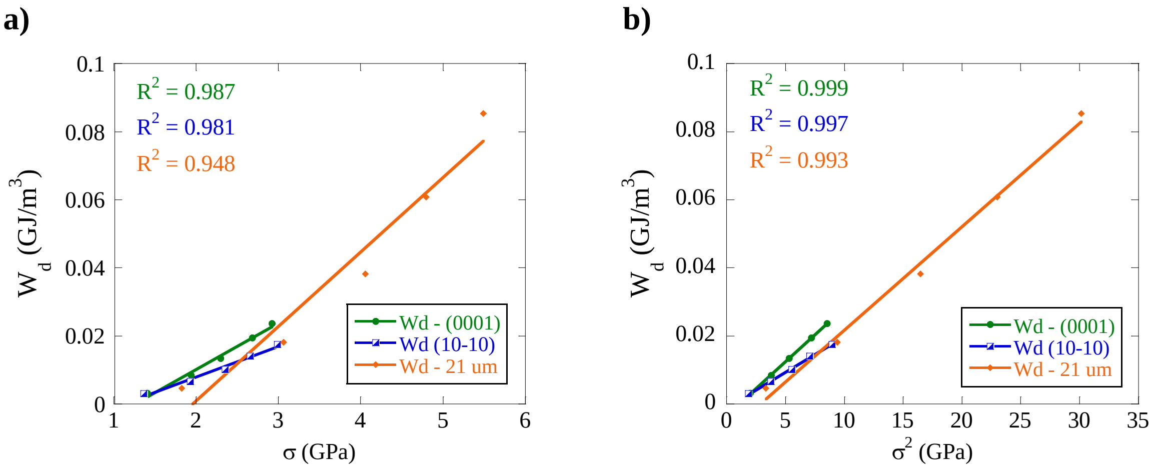

Figure 7-3. a) W_d plotted against σ as predicted by Jones et al. [88] is compared with b) W_d vs σ^2 in this study. Both plots show the same data set which were produced using a 100 μm tip on the (0001) plane (green), a 100 μm tip on the $(10\bar{1}0)$ plane (blue) and a 21 μm tip on the (0001) plane of Ti_3SiC_2. The values for R^2 showed a better fit to a line when W_d was plotted against σ^2.

The variation in energy dissipation between Mg and Zn is possibly a result of the difference in the dislocation core widths. Mg has a larger core width as compared to Zn, which renders Mg more ductile than Zn, and allows Mg deform plastically more easily than Zn [14]. This relative “ease of plasticity” in Mg would result in earlier yielding and a higher range of plastic deformation. This would explain why the values for the total a/R in Mg are slightly lower than Zn in the same orientation, despite the fact both Mg and Zn have similar elastic moduli along [0001], (E_{Mg} = 61.5 GPa and E_{Zn} = 61.8 GPa) on the same plane. Indentations made on the Mg on the (0001) plane using a force of 150 mN, resulted in $\Delta a_B \approx 1.7$ μm (see Ch. 4), while those made on Zn on the (0001) plane using 150 mN resulted in $\Delta a_B \approx 0.7$ μm (see Ch. 5).

It remains to consider the possibility that different slip systems are activated to explain the differences in results between Mg and Zn. Mg has more than 12 slip systems while Zn has far fewer total slip systems. If slip did occur on one of the additional slip systems in Mg under c-axis compression, there would be fewer basal dislocations bowing in a network, leading to a lower value in the shear strain due to bowing, γ_B. In turn, narrower loops would be expected as well, which is not what was observed in this study (see Fig. 7-1). The basal slip system is the primary slip system active in both Mg and Zn, and slip on the $\{11\bar{2}2\}$ pyramidal planes under c-axis compression has been observed in Mg [92, 93] as well as in Zn [64]. Cross slip of <c+a> dislocations from the prismatic planes as a source mechanism for <c+a> dislocations was reported to be energetically favorable in metals like Zn and Be, but not favorable in metals like Mg and Ti [94]. Assuming cross slip of <c+a> dislocations occurred in both Mg and Zn via prismatic planes, it may be possible that since it was more energetically favorable for cross slip to occur in Zn, it occurred more easily leading to a lower density of dislocations bowing in a network. In contrast, the energy threshold for cross slip to occur in Mg may not have been achieved as easily, leading to less cross slip of <c+a> dislocations and thus more dislocations bowing in a network. Despite Mg having more total slip systems, and since cross slip of <c + a> dislocations via prismatic planes occurs more easily in Zn than the in Mg, the activation of different slip systems is a possibility – though unlikely – to explain the differences in experimental results between Mg and Zn.

Lastly, a brief comparison is made between the loops made on the (0001) plane and the $(10\bar{1}0)$ plane in Mg. Plots were made of W_d vs (σ/G) (see Fig. 7-4) on both orientations despite the material being the same. For a given stress, more energy is dissipated in the (0001) orientation than in the $(10\bar{1}0)$ orientation.

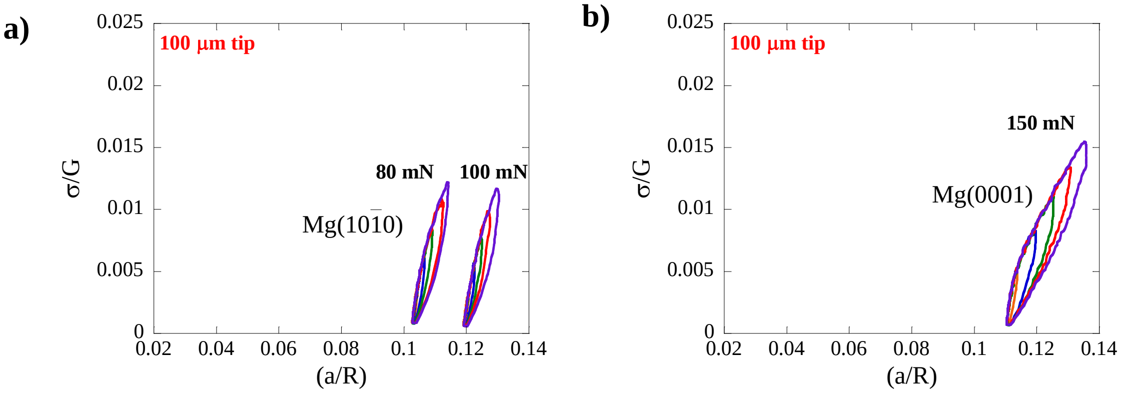

Figure 7-4. a) σ/G is plotted against a/R for nested cycles loaded on the $(10\bar{1}0)$ plane on Mg single crystal. These cycles resulted in comparable a/R values for Mg in the (0001) orientation, shown in b). Note that the loops in (a) shows no distinctive variation when normalized by G, which means either series (80 mN or 100 mN) in part (a) can be *directly* compared with the loops in part (b) at comparable a/R values. As shown, the loops from the (0001) plane were larger than those on the $(10\bar{1}0)$ plane.

CHAPTER 8: SUMMARY, CONCLUSION AND FUTURE WORK

8.1 Summary and Conclusion

In this study to investigate the origins of fully reversible hysteresis loops in stress-strain curves, it has been shown that dislocations bowing in a network in the form of LAKBs offers a plausible explanation to the observations made on Mg single crystal by indenting on the (0001) plane, and also by indenting on the (0001), $(10\bar{1}2)$ and $(10\bar{1}1)$ planes in Zn. W_d was typically larger for Mg at comparable values of a/R compared with values from Zn. Twinning was observed when indentations were made on the $(10\bar{1}1)$ plane in Mg, and the growth and shrinking of $\{10\bar{1}2\}$ tensile twins are believed to be responsible for W_d in that orientation. The growth and shrinkage of $\{10\bar{1}2\}$ tensile twins in Mg is well known [16, 46, 61] and observations made in this study are consistent with the behavior reported in literature. More work is certainly needed to fully understand the role twins play in the reversible hysteresis loops, however.

Reversible loops observed in Ti_3SiC_2 were the result of either defects or a mode of failure – the latter of which exhibited unique signatures in the indentation stress vs. a/R curves. SEM images of cracking and delamination around such indents are consisted with the mechanical behavior observed as well as that which is reported in literature. When loops resulted from defects, a dislocation bowing model was applied to determine whether or not dislocations are a reasonable explanation for the reversible hysteresis effect. The model, unfortunately was unable to explain all phenomena observed in this study. Thus, ripplocations were considered as an alternate defect that would explain the experimental observations.

The first possible evidence supporting the existence of ripplocations existing in a bulk crystal was presented in this study on Ti_3SiC_2. Conventional basal dislocations - the only kind known to exist in the MAX phases - could not account for c-axis strain observed in this study.

Ripplocations were nucleated and became mobile under cyclic loading and unloading dissipated more energy than conventional dislocations at comparable values of a/R. The energy dissipation may be a type of signature to indicate the presence of ripplocations in a material in a like manner that cracking is distinguishable from deformation in the indentation stress vs. a/R curves.

8.2 Future Work

Many avenues of future work exist to extend existing knowledge on the origins of the hysteresis loops observed in this work, especially in understanding the precise role of twinning in this effect. A more detailed study of the micromechanical role that twinning has on the hysteresis effect will help to broaden the scope of understanding of the hysteresis effect. Detailed and careful TEM analysis of the LAKBs in Zn is also a promising frontier to more precisely quantifying the qualitative observations made in this study. Perhaps an in situ TEM experiment involving micro pillars would help to understand the formation of LAKBs in Zn and why they were quite diffuse. By extending the existing knowledge of both the deformation characteristics and mechanical behavior in Mg and Zn, more robust crystal plasticity models can be developed for these metals that will help lead to optimal use of these metals and their alloys in applications. It is especially important that the deformation behavior of Mg is well understood and robust crystal plasticity models are developed since Mg and its alloys are being considered by the automotive manufacturers as a material to reduce total vehicle weight, and thus reduce total green house emissions.

Ideas and results on Ti_3SiC_2 create multiple directions for future work. While the results of Jones et al. [88] were not directly comparable with results in this study, their ideas that reversible loops are caused by residual lattice strain due to a limited number of slip systems deserves more investigation and attention as a possible explanation. These comments notwithstanding the fact that dislocations are most likely not the micromechanism responsible for the energy dissipation renders many of these arguments questionable.

Perhaps even more fascinating from this study was the possible existence of a new defect type in bulk solids, ripplocations. The future potential for understanding the fundamental nature of defects in layered solids is an exciting frontier. Evidence supporting this new defect type presented in this study lays the groundwork for future investigations. By better quantifying and investigating the character and nature of ripplocations in bulk crystals, we may more precisely understand the microstructural changes in deformation process and the energy dissipation in these solids. This is important to understand since Ti_3SiC_2 is considered a possible candidate in a variety of fusion and fission nuclear applications, which requires better understanding of how the microstructure changes in the presence of radiation. The work in this study may help to pave the way for studies involving ripplocation interactions with radiation.

REFERENCES

[1] U.S.E.P.A. (EPA), 2015.
[2] B.L. Mordike, T. Ebert, Materials Science and Engineering: A, 302 (2001) 37-45.
[3] M.V. 2020, (2006).
[4] I.Z. Association, 2015.
[5] M.K. Patel, D.J. Tallman, J.A. Valdez, J. Aguiar, O. Anderoglu, M. Tang, J. Griggs, E. Fu, Y. Wang, M.W. Barsoum, Scripta Materialia, 77 (2014) 1-4.
[6] C. Wang, T. Yang, S. Kong, J. Xiao, J. Xue, Q. Wang, C. Hu, Q. Huang, Y. Wang, Journal of Nuclear Materials, 440 (2013) 606-611.
[7] M.H. Yoo, J.R. Morris, K.M. Ho, S.R. Agnew, Metall and Mat Trans A, 33 (2002) 813-822.
[8] J.J. Gilman, Journal of Metals, 6 (1954) 621-629.
[9] E. Orowan, Nature, 149 (1942) 643-644.
[10] A.J.W. Moore, Acta Metallurgica, 3 (1955) 163-169.
[11] M. Barsoum, L. Farber, T. El-Raghy, Metall and Mat Trans A, 30 (1999) 1727-1738.
[12] S. Basu, A. Zhou, M. Barsoum, Journal of Structural Geology, 31 (2009) 791-801.
[13] M.W. Barsoum, Basu, S., in: R.W.C. K. H. Jurgen Buschow, Merton C. Flemings, Bernard Ilschner (print), Edward J. Kramer, Subhash Mahajan, and Patrick Veyssiere (updates) (Ed.) Encyclopedia of Materials: Science and Technology, Elsevier, Oxford, 2010, pp. 1-23.
[14] M.H. Yoo, Symposium on the Role of Twinning in Fracture of Metals and Alloys, 15-19 Oct. 1978, USA, 1981, pp. 409-418.
[15] P.G. Partridge, Metallurgical Reviews, 12 (1967) 169-194.
[16] J.W. Christian, S. Mahajan, Progress in Materials Science, 39 (1995) 1-157.
[17] M.H. Yoo, Transactions of the Metallurgical Society of AIME, 245 (1969).
[18] M.W. Barsoum, A. Murugaiah, S.R. Kalidindi, T. Zhen, Y. Gogotsi, Carbon, 42 (2004) 1435-1445.
[19] S. Basu, M.W. Barsoum, Journal of Materials Research, 22 (2007) 2470-2477.
[20] J.J. Gilman, Journal of Metals, 8 (1956) 1326-1336.
[21] F. Frank, A. Stroh, Proceedings of the Physical Society. Section B, 65 (1952) 811.
[22] A. Kushima, X. Qian, P. Zhao, S. Zhang, J. Li, Nano letters, 15 (2015) 1302-1308.
[23] A. Murugaiah, M.W. Barsoum, S.R. Kalidindi, T. Zhen, Journal of materials research, 19 (2004) 1139-1148.
[24] S. Basu, M.W. Barsoum, S.R. Kalidindi, Journal of Applied Physics, 99 (2006) 063501.
[25] A.G. Zhou, M.W. Barsoum, Metall and Mat Trans A, 40 (2009) 1741-1756.
[26] A.G. Zhou, S. Basu, M.W. Barsoum, Acta Materialia, 56 (2008) 60-67.
[27] A. Zhou, M. Barsoum, Journal of alloys and compounds, 498 (2010) 62-70.
[28] M.W. Barsoum, T. Zhen, A. Zhou, S. Basu, S.R. Kalidindi, Physical Review B, 71 (2005) 134101.
[29] M.W. Barsoum, M. Radovic, Annual review of materials research, 41 (2011) 195-227.
[30] S. Basu, M.W. Barsoum, J. Struct. Geology, 31 (2009) 791–801.
[31] S. Basu, A. Moseson, M.W. Barsoum, Journal of materials research, 21 (2006) 2628-2637.
[32] I.N. Sneddon, Int. J. Eng. Sci., 3 (1965).
[33] W.C. Oliver, G.M. Pharr, Journal of materials research, 19 (2004) 3-20.
[34] J. Field, M. Swain, Journal of Materials Research, 10 (1995) 101-112.
[35] R.H. H. Yoshinaga, Trans. JIM 4(1963) 1-8.
[36] J.-H.S.e. al., Scripta Materialia, 68 (2013) 483-486.

[37] L. Capolungo, P.E. Marshall, R.J. McCabe, I.J. Beyerlein, C.N. Tomé, Acta Materialia, 57 (2009) 6047-6056.
[38] S.-G. Hong, S.H. Park, C.S. Lee, Acta Materialia, 58 (2010) 5873-5885.
[39] S.R. Agnew, J.A. Horton, M.H. Yoo, Metall and Mat Trans A, 33 (2002) 851-858.
[40] J. Ye, R.K. Mishra, A.K. Sachdev, A.M. Minor, Scripta Materialia, 64 (2011) 292-295.
[41] W.F.H. E.W. Kelley, Trans. TMS-AIME, 242 (1968) 654.
[42] W.F.H. E.W. Kelley, Trans. TMS-AIME, 242 (1968) 5.
[43] M.H. Yoo, J.K. Lee, Philosophical Magazine A, 63 (1991) 987-1000.
[44] H. Kitahara, T. Mayama, K. Okumura, Y. Tadano, M. Tsushida, S. Ando, Acta Materialia, 78 (2014) 290-300.
[45] D. Catoor, Y.F. Gao, J. Geng, M.J.N.V. Prasad, E.G. Herbert, K.S. Kumar, G.M. Pharr, E.P. George, Acta Materialia, 61 (2013) 2953-2965.
[46] M.R. Barnett, Materials Science and Engineering: A, 464 (2007) 1-7.
[47] M.R. Barnett, Materials Science and Engineering: A, 464 (2007) 8-16.
[48] G.E. Mann, T. Sumitomo, C.H. Cáceres, J.R. Griffiths, Materials Science and Engineering: A, 456 (2007) 138-146.
[49] P.G. Partridge, E. Roberts, Acta Metallurgica, 12 (1964) 1205-1210.
[50] L. Capolungo, I.J. Beyerlein, C.N. Tomé, Scripta Materialia, 60 (2009) 32-35.
[51] S. Basu, A.G. Zhou, M.W. Barsoum, J. Mater. Res., 23 (2008) 1334-1338.
[52] M.W. Barsoum, T. Zhen, A. Zhou, S. Basu, S. Kalidindi, Phys. Rev. B., 71 (2005) 134101.
[53] A.G. Zhou, M.W. Barsoum, Journal of Alloys and Compounds, 498 (2010) 62-70.
[54] D. Catoor, Y.F. Gao, J. Geng, M.J.N.V. Prasad, E.G. Herbert, K.S. Kumar, G.M. Pharr, E.P. George, Acta Mater, 61 (2013) 2953–2965.
[55] J.M. Roberts, D.E. Hartman, Tran. AIME, 230 (1964) 1125-1133.
[56] J.M. Roberts, N. Brown, Trans. AIME, 218 (1960) 454-463.
[57] J.J. Gilman, Trans. AIME, 200 (1954) 621.
[58] A.G. Zhou, M.W. Barsoum, J. Alloys Compds., 498 (2010) 62-67.
[59] K. Lucke, A.V. Granato, Phys. Rev. B (1981).
[60] W.F. Gale, T.C. Totemeier, Smithells metals reference book, Butterworth-Heinemann, 2003.
[61] Y. Cui, Y. Li, S. Sun, H. Bian, H. Huang, Z. Wang, Y. Koizumi, A. Chiba, Scripta Materialia, 101 (2015) 8-11.
[62] R. Parisot, S. Forest, A. Pineau, D. Mareuse, X. Demonet, Proceedings of Conference on Advances in Mechanical Behavior, Plasticity and Damage (EUROMAT 2000), 7-9 Nov. 2000, Elsevier Science, Kidlington, UK, 2000, pp. 407-412.
[63] R.L. Bell, R.W. Cahn, Proceedings of the Royal Society of London. Series A. Mathematical and Physical Sciences, 239 (1957) 494-521.
[64] H.S. Rosenbaum, Acta Metallurgica, 9 (1961) 742-748.
[65] M.H. Yoo, C.T. Wei, Journal of Applied Physics, 38 (1967) 2974-2976.
[66] J.G. Antonopoulos, T. Karakostas, P. Komninou, P. Delavignette, Acta Metallurgica, 36 (1988) 2493-2502.
[67] M.W. Barsoum, T. Zhen, S.R. Kalidindi, M. Radovic, A. Murugaiah, Nat Mater, 2 (2003) 107-111.
[68] S. Basu, A. Zhou, M.W. Barsoum, Journal of Materials Research, 23 (2008) 1334-1338.
[69] J. Bradby, S. Kucheyev, J. Williams, C. Jagadish, M. Swain, P. Munroe, M. Phillips, Applied physics letters, 80 (2002) 4537-4539.

[70] A. Granato, K. Lucke, Journal of Applied Physics, 27 (1956) 583-593.
[71] L.T.N. J.S. Lecomte, F. Abbes, C. Schuman, and J.M. Raulot, Trans Tech Publications, 783-786 (2014) 2327-2332.
[72] D. Lorenz, A. Zeckzer, U. Hilpert, P. Grau, H. Johansen, H.S. Leipner, Physical Review B, 67 (2003) 172101.
[73] S. Basu, O.A. Elshrief, R. Coward, B. Anasori, M.W. Barsoum, Journal of Materials Research, 27 (2012) 53-63.
[74] W.D. Nix, H. Gao, Journal of the Mechanics and Physics of Solids, 46 (1998) 411-425.
[75] K. Lücke, A.V. Granato, Physical Review B, 24 (1981) 6991-7006.
[76] N.H. Jeitschko W., Benesovky F. , Monatsh Chem., 94 (1963) 672.
[77] Z. Sun, Y. Zhou, Physical Review B, 60 (1999) 1441-1443.
[78] T.H. Scabarozi, S. Amini, P. Finkel, O.D. Leaffer, J.E. Spanier, M.W. Barsoum, M. Drulis, H. Drulis, W.M. Tambussi, J.D. Hettinger, S.E. Lofland, Journal of Applied Physics, 104 (2008) 033502-033501.
[79] M.W. Barsoum, T. El-Raghy, Journal of the American Ceramic Society, 79 (1996) 1953-1956.
[80] L. Farber, M.W. Barsoum, A. Zavaliangos, T. El-Raghy, I. Levin, Journal of the American Ceramic Society, 81 (1998) 1677-1681.
[81] Y. Zhou, Z. Sun, Journal of the European Ceramic Society, 21 (2001) 1007-1011.
[82] J.M. Molina-Aldareguia, J. Emmerlich, J.-P. Palmquist, U. Jansson, L. Hultman, Scripta Materialia, 49 (2003) 155-160.
[83] A. Joulain, L. Thilly, J. Rabier, Philosophical Magazine, 88 (2008) 1307-1320.
[84] C. Tromas, P. Villechaise, V. Gauthier-Brunet, S. Dubois, Philosophical Magazine, 91 (2011) 1265-1275.
[85] A. Guitton, A. Joulain, L. Thilly, C. Tromas, Sci. Rep., 4 (2014).
[86] B.R. Lawn, D.B. Marshall, Journal of the Mechanics and Physics of Solids, 46 (1998) 85-113.
[87] B. Poon, L. Ponson, J. Zhao, G. Ravichandran, Journal of the Mechanics and Physics of Solids, 59 (2011) 2238-2257.
[88] N.G. Jones, C. Humphrey, L.D. Connor, O. Wilhelmsson, L. Hultman, H.J. Stone, F. Giuliani, W.J. Clegg, Acta Materialia, 69 (2014) 149-161.
[89] B. Anasori, M.W. Barsoum, MRS Communications, 3 (2013) 245-248.
[90] B. Anasori, K.E. Sickafus, I.O. Usov, M.W. Barsoum, J. Appl. Phys., 110 (2011) 023516.
[91] S. Basu, M.W. Barsoum, J. Mater. Res., 22 (2007) 2470-2477.
[92] T. Obara, H. Yoshinga, S. Morozumi, Acta Metallurgica, 21 (1973) 845-853.
[93] J.F. Stohr, J.P. Poirier, Philosophical Magazine, 25 (1972) 1313-1329.
[94] M.H. Yoo, S.R. Agnew, J.R. Morris, K.M. Ho, Materials Science and Engineering: A, 319–321 (2001) 87-92.

APPENDIX A: EFFECT OF CYCLING ON Ti_3SiC_2

There was some variation between when using 25 or 50 cycles on Ti_3SiC_2. Figure A1 shows the nested cycles for a location that was loaded to 550 mN for 50 cycles using a 100 μm spherical tip. The loops from the 50 cycles were slightly larger and more work hardened than the loops that resulted after 25 cycles. This slight variation is expected, to some degree. σ_Y after 50 cycles is lager, which again can be expected since material at this location was more work hardened.

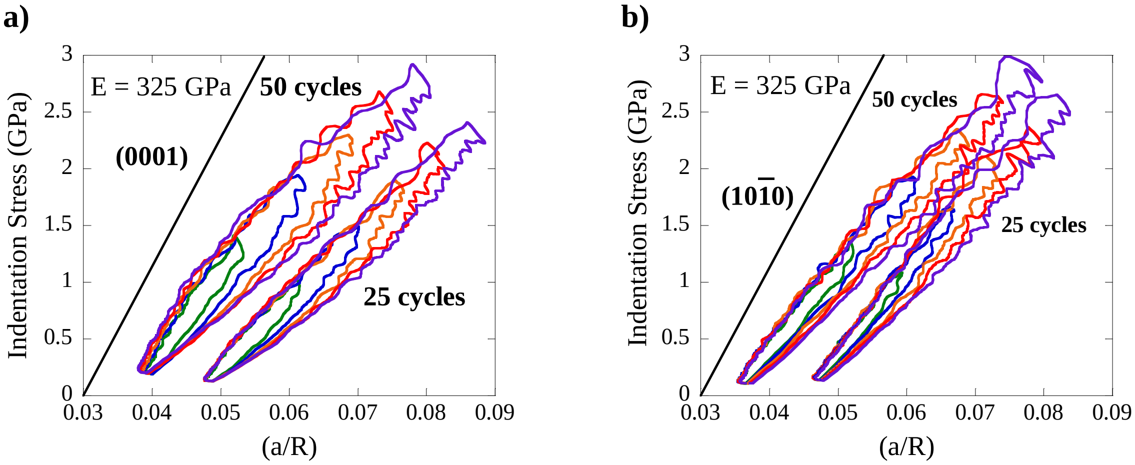

Figure A1. a) Indentation stress vs. a/R curve for nested loops at locations A1 and A4, which were loaded to 550 mN for 25 and 50 cycles, respectively using a 100 μm tip. b) Indentation stress vs. a/R curve for nested loops at locations E1 and E4, which were loaded to 550 mN for 25 and 50 cycles, respectively using a 100 μm tip.

Total a/R values after 25 cycles were higher than after 50 cycles when using the same applied load despite drift being minimal for each location plotted in Fig. A1. Shifting was not applied to any data set. This observation is different than that observed on Mg where the total a/R was the same when using the same applied load. This is an illustration of the discrepancies that typically resulted during the first loading cycle in the MAX phases, as mentioned in Ch. 6.

Nonetheless, the results in this thesis are still valid despite these small discrepancies since the nested cycles were the focal point in this study.